PR12-18-005

# Proposal for the PAC 46: Timelike Compton Scattering off a transversely polarized proton

June 2, 2018


## Abstract

We propose to measure Timelike Compton Scattering (TCS) off the proton using a transversely polarized target. The TCS process corresponds to the scattering of a real photon off a quark, followed by the emission of a high virtuality photon decaying into a lepton pair. According to QCD factorization theorems, TCS can be parametrized by Generalized Parton Distributions (GPDs), containing information about the transverse spatial distribution of quarks and their longitudinal momenta inside the proton. Using a transversely polarized proton target and a real circularly polarized photon beam, we can access several independent observables which are sensitive to the GPDs, in particular the GPD E. TCS measurements will provide a first fundamental test of the universality of the GPDs. We plan to measure the TCS+BH (TCS+Bethe-Heitler interfering process) unpolarized cross section, cross section of circularly polarized photon beam, and cross section of transversely polarized proton. The major goal of this experiment is to access the GPD H, $\tilde{H}$ and E from TCS observables, and in particular the GPD E, which is poorly constrained and contains information about the orbital momentum of the quarks. The other major goal is to compare GPDs extracted from TCS (timelike process) to GPDs extracted from DVCS (Deeply Virtual Compton Scattering, spacelike process), and test the GPDs universality and its possible violations. This experiment will take place at the Jefferson Laboratory Hall C experimental facility, using a transversely polarized target, electromagnetic calorimeters and recoil proton detectors.



**Keywords** *Generalized Parton Distributions, Compton Form Factors, Timelike Compton Scattering, Neutral Particle Spectrometer, Compact Photon Source, Hall C.*


**Related experiments at Jefferson Laboratory** *E12-12-006A [1] with SoLID (approved), E12-12-001 [2] with CLAS12 (running).*

A. Camsonne, M. Carmignotto, R. Ent, C. Keith, C. Keppel, D. Mack, J. Maxwell, L. Pentchev, A. Somov, B. Wojtsekhowski, S.A. Wood, C. Zorn
*Jefferson Laboratory, Newport News, Virginia 23606*

A. Asaturyan, A. Mkrtchyan, H. Mkrtchyan, V. Tadevosyan[1], H. Voskanyan, S. Zhamkochyan
*A. I. Alikhanyan National Science Laboratory, 0036 Yerevan, Armenia*

S. Ali, V. Berdnikov, M. Boër[2],T. Horn, G. Kalicy, I.L. Pegg, R. Trotta
*The Catholic University of America, Washington, D.C. 20064*

D. Day, D. Keller[3], S. Liuti, D. Perera, O. Rondon, J. Zhang
*University of Virginia, Charlottesville, VA 22904*

P. Chatagnon, R. Dupré, M. Ehrhart, M. Guidal, H.S. Ko, D. Marchand, C. Munoz Camacho, S. Niccolai, E. Voutier, R. Wang, S. Zhao
*Université Paris-Sud, Institut de Physique Nucleaire d'Orsay, 91406 Orsay, France*

M. Amaryan, C. Hyde, M. Kerver, M.N.H. Rashad
*Old Dominion University, Norfolk, Virginia 23529*

R. Paremuzyan
*University of New Hampshire, Durham, NH-03824*

G. Niculescu
*James Madison University, Harrisonburg, Virginia 22807*

J. Stevens, W. Li
*Physics Department, College of William and Mary, Williamsburg VA 23187*

P. King, J. Roche
*Ohio University, Athens, OH 45701*

J.R.M. Annand, D.J. Hamilton
*University of Glasgow, Glasgow, Scotland, UK*

K.-T. Brinkmann, S. Diehl, R. Novotny, H.-G. Zaunick
*Universitaet Giessen, Giessen, Germany*

I. Strakovsky, W.J. Briscoe,
*George Washington U., Washington, DC 20052*

[1]Co-spokesperson
[2]Co-spokesperson and Contact person: mboer@jlab.org
[3]Co-spokesperson

D. Dutta
*Mississippi State University, Starkville, MS 39762*

E. Kinney
*University of Colorado, Boulder, CO 80309*

V. Bellini
*University of Catania, Catania, Italy*

I. Albayrak
*Hampton University, Hampton, Virginia 23669*

S. Sirca
*University of Ljubljana, Ljubljana, Slovenia*

And the NPS Collaboration.

# Contents

# 1 Introduction

## 1.1 Timelike Compton Scattering physics

The Timelike Compton Scattering (TCS) process corresponds to the exclusive photoproduction of a lepton pair with exchange of a high virtuality photon. A real photon is scattered off a quark of the nucleon, and a high virtuality photon is emitted, then decays into a lepton pair ($\gamma N \hookrightarrow \gamma^* N' \rightarrow e^+e^-N'$, Fig. 1). Typically, the photon virtuality $Q'^2 = +q'2 = (k - k')^2$ (where q', k, k' are the 4-momenta of the virtual photon, the electron and the positron respectively), is greater than $\sim 1$ GeV$^2$ to allow for factorization of the TCS amplitude between a hard part, calculable from perturbative QED (upper part of the diagram 1) and a soft QCD non perturbative part (lower part of the diagram 1). TCS is sensitive to the transverse spatial distribution of partons in the nucleon and the correlation with their longitudinal momentum. It can be parametrized by Generalized Parton Distributions (GPDs), which have been introduced in [3, 4, 5]. Assuming massless quarks, at QCD leading order and leading twist in QCD, we can parametrize TCS with 4 helicity conserving quark GPDs: H, E, $\tilde{\text{H}}$, $\tilde{\text{E}}$. They correspond to 4 independent helicity-spin transitions between the initial quark-proton system and the final one, and are the Fourier transform of the QCD matrix element of the soft part of the TCS amplitude. Given the kinematic domain accessible at JLab, we neglect GPDs of gluons. At leading order, the GPDs depend on 3 independent variables besides the 4-momentum transfer Q'$^2$: $x$ is the longitudinal momentum fraction of the nucleon momentum carried by the quark, $\xi$ is proportionnal to the longitudinal momentum transfer to the quark, and $t$ is the square 4-momentum transfer to the nucleon, i.e. t=(p-p')$^2$, where p and p' are the 4-momenta of the incoming and outgoing nucleon respectively. We refer to the reviews [5, 6, 7, 8] for details about GPD formalism and physics interests.

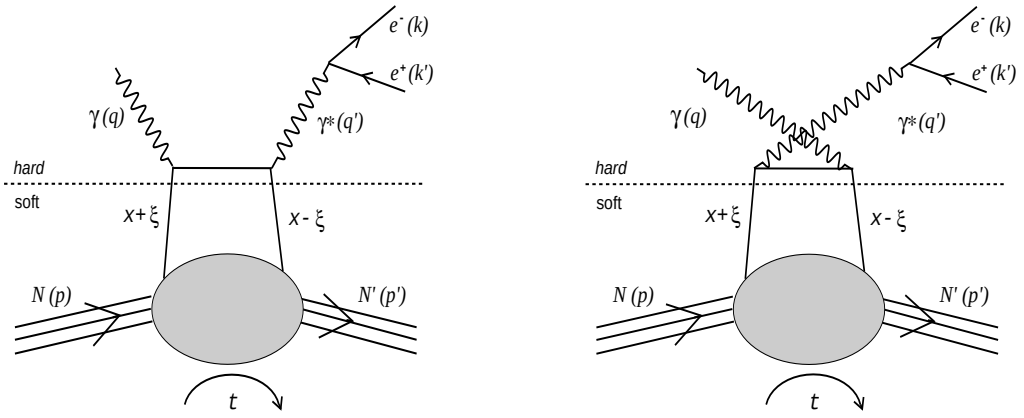


Figure 1: TCS leading order and leading twist handbag diagrams.

TCS interferes with a Bethe-Heitler like process (BH), where the incoming real photon splits into a lepton pair in the nucleon field (Fig. 2). BH depends on the nucleon Form Factors (FFs) and is not sensitive to GPDs. Since TCS and BH leads to the same final state, experimental measurements of the hard exclusive lepton pair photoproduction reaction contain the two processes and their interference, and cannot be measured separately. As it will be discussed later, the BH amplitude is always largely dominant compared to the TCS one at JLab kinematics. However, the interference between BH and TCS is enhancing TCS, which would have a rather small cross section otherwise. Several spin dependent observables (from polarized beam and/or target) allow for accessing directly or indirectly the TCS+BH interference term, and information about GPDs, as discussed in [9, 10]. Measuring several independent observables allow to extract the GPDs, as it will be shown later. It should be noticed that in TCS, as well as in all deeply virtual exclusive experiments, we don't access directly GPDs, since they appear in the amplitude integrated over the $x$ variable. The observables are given by the Compton Form Factors (CFFs), which are complex functions of GPDs depending on $\xi$, t and Q'$^2$: we therefore associate 2 independent quantities to each GPD, corresponding to the imaginary and the real part of the CFFs. For example, $\Im\mathcal{H}$ and $\Re\mathcal{H}$ are functions of the GPD H.

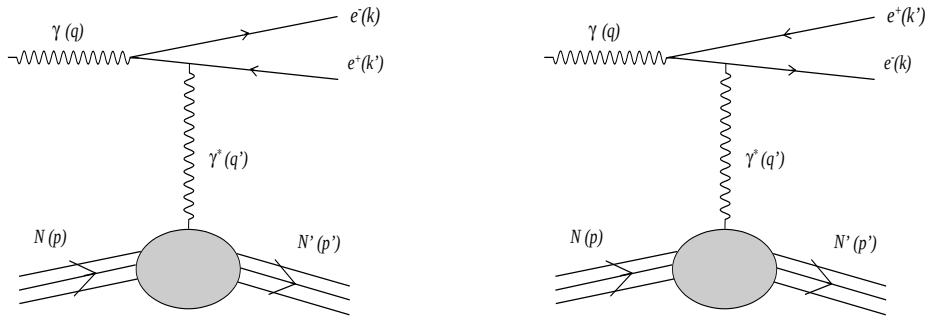


Figure 2: Bethe-Heitler process interfering with TCS, leading order and leading twist diagrams.

An analogy can be made between TCS and Deeply Virtual Compton Scattering (DVCS = $eN \hookrightarrow \gamma^* N \rightarrow e'N'\gamma$ - Fig. 3), which corresponds to the scattering of a high virtuality photon, coming from a lepton beam, off a quark of the nucleon. DVCS has been intensively studied over the past 15 years, and measurements of DVCS observables already lead to DVCS CFFs and GPD measurements, constraining GPD models [8]. However, the real part of DVCS CFFs is poorly constrained by existing measurements. While different models are in good agreement for imaginary part of CFFs, predictions differ on the real part. In addition, the GPD E is poorly constrained and there is a real need of independent measurements sensitive to it. E describes the quark and gluon motion in a transversely polarized nucleon. Its measurement is key for testing the nucleon angular

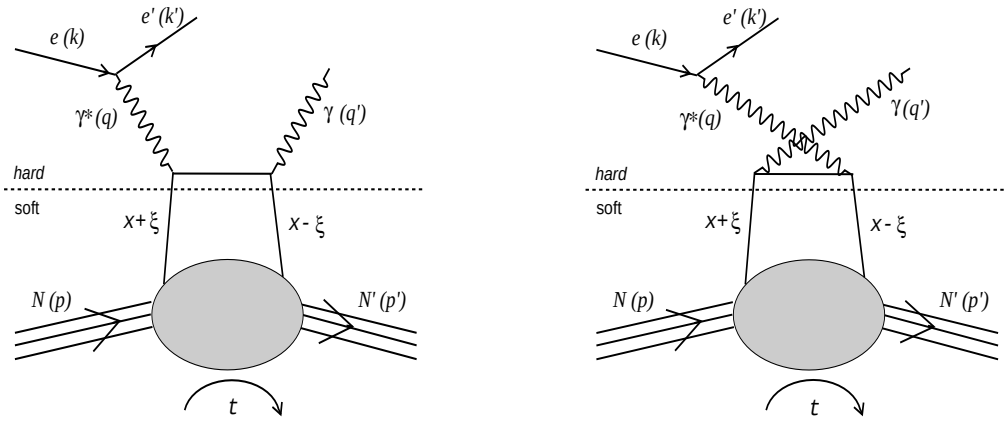


Figure 3: DVCS leading order and leading twist handbag diagrams.

momentum sum rule (Ji sum rule [4, 11]):

$$J^q(t=0) = \frac{1}{2}\int dx\, x\, [H^q(x,\xi,t=0) + E^q(x,\xi,t=0)] = \frac{1}{2}\Delta\Sigma + L_q \quad (\forall\xi), \tag{1}$$

where $L_q$ is the quark angular momentum and $\Delta\Sigma$ is the fraction of the nucleon spin carried by the quarks ($\Delta\Sigma \approx 0.3$). Indeed, there is a strong interest in measuring GPD E to understand the quark orbital momentum contribution to the proton spin, or how the nucleon spin is distributed within its constituents.

As shown in [7], the DVCS and TCS amplitudes are complex conjugate at leading order and leading twist. At this order, both processes access the same GPDs at the same kinematic points ($\xi$, t), and their CFFs are complex conjugates. Demonstrating the universality of QCD structure functions such as GPDs is a significant stage in our field. Comparing GPDs extracted from DVCS (spacelike process) to GPDs extracted from TCS (timelike process) is therefore one of the most important results we can obtain from our TCS experiment in addition to other independent DVCS measurements. We will therefore demonstrate the feasibility of extracting CFFs from TCS observables, at a level comparable with DVCS for performing such comparison. Furthermore, as the only soft part involved in the DVCS and TCS processes corresponds to the GPDs, these two processes can be seen as the cleanest one to access GPDs without additional unknowns. In the eventuality of non-negligible higher twist effects in TCS and in DVCS, our measurements will allow for a comparative study of these effects in a spacelike versus a timelike process.

Assuming, or after demonstrating, that GPDs are universal (at twist 2), constraining GPD E from TCS measurements will be complementarily to the existing and planned measurements of DVCS in the JLab 12 GeV program. Indeed, under the assumption of GPD universality and ne-

glecting higher twist and higher order effects in DVCS and TCS, it is possible to complementarily constrain GPDs from DVCS and from TCS measurement as we will demonstrate. TCS observables, particularly the transversely polarized target cross sections, bring new independent information and allow to extract all proton CFFs simultaneously in a multi-parameters, multi-observables CFFs fitting approach.

In the following, we will present the TCS formalism and the observables we intend to measure. We will discuss the impact of the measurements and the projection of experimental uncertainties. We propose an experimental setup, which uses an untagged bremsstrahlung photon beam from the Compact Photon Source [12], the UVa/JLab transversely polarized ammonia $NH_3$ target [13, 14], detectors for the recoil proton detection and a pair of electromagnetic calorimeters, similar to the calorimeter of the Neutral Particle Spectrometer project [15].

### 1.2 Brief summary of the science case

The main measurement of our experiment is the transverse target spin asymmetry of the TCS+BH reaction, in addition to the unpolarized cross section and the circularly polarized beam spin asymmetry. For illustration, we display Fig. 4 the expected transverse target spin asymmetry and the statistical uncertainties for a selected bin. The major impacts of the measurements will be:

1. Extraction of the CFF $\Im E$ and parametrization of GPD E. This result will allow for understanding the partition of the nucleon angular momentum among the quarks.

2. Demonstration or proof of violation of GPDs universality by comparative measurement of CFFs extracted from TCS (timelike) and DVCS (spacelike). Fig. 5 shows the precision expected on extracted CFFs from TCS (under some assumptions detailed in the document).

3. Simultaneous fits of CFFs with DVCS and TCS to constrain all CFFs (twist 2) at the same time thanks to new independent observables from TCS, provided the GPD universality is established.

Our experiment will be the first one accessing the TCS transverse target spin asymmetries and $\Im E$ of the proton from TCS. The unpolarized and beam polarized cross sections will be measured with $\sim$ 10 to 100 times higher luminosity than other approved experiments, with a narrower acceptance, allowing for a precision measurement. An experiment is running using the CLAS12 spectrometer [2] (E12-12-001) and aims at measuring the unpolarized cross section and beam spin asymmetry (circularly polarized). It will allow for accessing the cos($\phi$) and sin($\phi$) moments of the cross sections, and constrain the GPD H. Another experiment will use the SoLID spectrometer [1] (E12-12-006A) and is approved as a run-group proposal in parallel to the J/$\Psi$ experiment E12-12-006 [16]. The SoLID experiment is similar to the CLAS12 one, but benefits from a higher luminosity ( 10 times) on a narrower acceptance range, allowing for binning in Q'$^2$ and studies of NLO effects. The main advantages of our experiment compared to the other TCS approved measurements are the first and unique access to $\Im E$ from the target spin asymmetries, a larger photon luminosity (up to $10^{35}$ cm$^{-2}$ sec$^{-1}$), and the real photon beam in comparison to the use of a quasi-real photon on the other experiments, which implies some approximations and angular corrections at the analysis and calculation levels. The increased precision, and the larger number of independent observables of our experiment allow for studies of GPDs universality and higher twist effects in TCS versus DVCS. If we assume that the same CFFs can be accessed through DVCS, a conditionally approved experiment in CLAS12 aims at measuring DVCS transverse target spin asymmetries and accessing $\Im E$ of the proton (E-12-12-010) [17]. Overall, the experiment we are proposing is unique (TCS off a transversely polarized proton) and will provide for the first time an access to $\Im E$ of the proton. In complement to DVCS experiments, it will allow for studies on GPDs universality at a $10$ times better precision level than other TCS experiment for the GPD H, it will allow for the first time to study universality on GPD $\tilde{H}$ and E (providing another DVCS measurement in the future), and a drastic reduction on the uncertainty on $\Re H$, which is poorly constrained by current GPD models (strong discrepencies between dual-type and double distribution based GPD models).

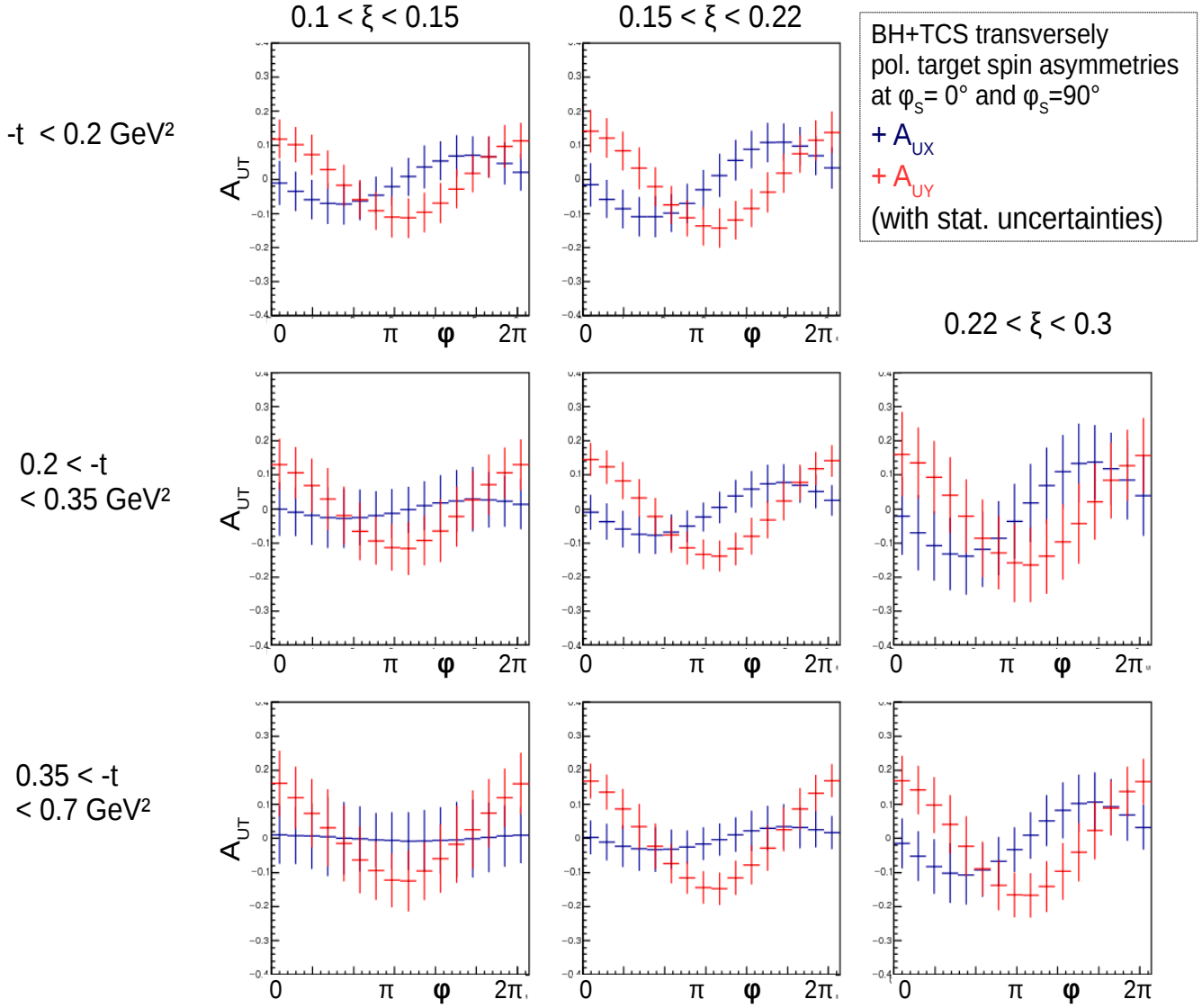


Figure 4: Projection of the single transversely polarized target spin asymmetries for $\phi_S = 0°$ (blue) and $\phi_S = 90°$ (red), as a function of 16 bins in $\phi$. Statistic uncertainties are represented and correspond to an integrated photon luminosity of $5.85 * 10e5$ pb$^{-1}$ for $5.5 < E_\gamma < 11$ GeV. The projections include acceptance, phase-space cuts, momentum thresholds and a $E_\gamma > 7.5$ GeV cut (see section 4.6). Systematic uncertainties and the 27% target polarization dilution factor are not included. Our interpretations are based on projections for $-t > 0.2$ GeV$^2$ only ($2^d$ and $3^d$ rows) due to magnetic field effects and the limited acceptance at smaller -t.

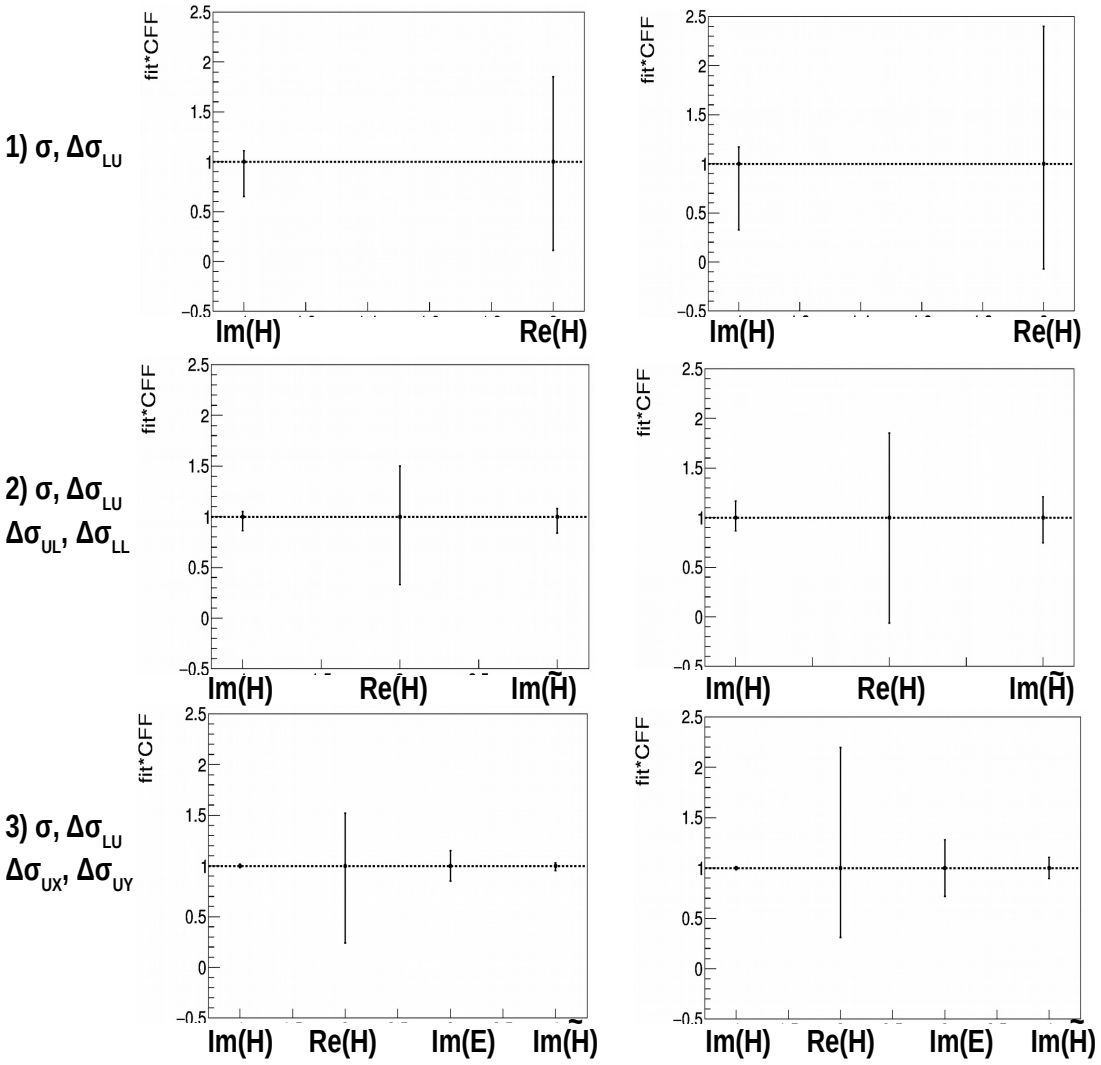


Figure 5: Extracted CFFs from DVCS (left column) and TCS (right column), using $\sigma$ and $\Delta\sigma_{LU}$ (top row), using $\sigma$, $\Delta\sigma_{LU}$, $\Delta\sigma_{UL}$, $\Delta\sigma_{LL}$ (center row) and using $\sigma$, $\Delta\sigma_{LU}$, $\Delta\sigma_{UX}$, $\Delta\sigma_{UY}$ (bottom row). The sensitivity to CFFs of this experiment corresponds to the bottom row right figure (with transversely polarized TCS) and can be compared to other TCS experiments (top row, right column) and existing DVCS experiments (top and center row, left column). The uncertainties are based on pseudo-data azimuthal distribution fitting with the assumption of 5% error per bin for the unpolarized cross section and 7% per bin for the polarized cross section, with 16 bins in $\phi$.

The proposed experimental setup for the measurements consists of a high intensity photon source, a transversely polarized proton target, and detectors to measure the decay lepton pair and the recoil proton from the BH/TCS reaction in coincidence. Some of the group members of the proposal are deeply involved in the design and construction of the components of the setup which are already under development. Other members are ready to take responsibility for development of new components. The Compact Photon Source [12] is being developed by joint efforts of the CPS collaboration and JLab. The NPS collaboration will take responsibility for the development and the construction of the electromagnetic calorimeters for the lepton detection. The UVa and JLab polarized target groups ([18], [19]) will provide the transversely polarized proton target.

# 2 Physics case

## 2.1 TCS formalism

The unpolarized TCS+BH cross section depends on five independent variables. In the following, we express it as a function of the beam energy ($E_\gamma$, which is more convenient for the simulations), or as a function of the longitudinal momentum transfer $\xi = \frac{Q'^2}{2s-Q'^2}$ (more convenient for the interpretations), where s=(p+q)$^2$ is the squared C.M. energy of the reaction (where p and q are the incoming proton and photon 4-momenta). The definition of $\xi$ is valid at the asymptotic limit (t/Q'$^2$ $\to 0$) (we refer to [9] for details). We also express the cross section as a function of the momentum transfer squared, t = (p-p')$^2$ (where p' is the recoil proton 4-momentum), the virtuality of the final photon, Q'$^2$ = + q'$^2$ (where q' is the scattered photon 4-momentum, timelike), and the polar and azimuthal angles ($\theta$, $\phi$) of the electron in the C.M. frame of the lepton pair versus the reaction plane (the $\gamma, \gamma^*$ plane). These angles are represented on Fig. 6: the left panel is a scheme of the reaction in the C.M. frame of the incoming photon and proton (see the legend for details about variables and angles). The right panel represents the angles in the virtual photon C.M. frame. The longitudinal axis for the boost between the two frames is used as reference for the final electron polar angle $\theta$.

At fixed beam energy, averaging over the beam and the initial and the final nucleon helicities, we express the 4-differential BH+TCS unpolarized cross section as

$$\frac{d^4\sigma}{dQ'^2 dt d\Omega}(\gamma p \to p' e^+ e^-) = \frac{1}{2\pi^4}\frac{1}{64}\frac{1}{(2m_N E_\gamma)^2} \mid T^{BH} + T^{TCS} \mid^2,$$

where the $\mid T^{BH}+T^{TCS} \mid^2$ term corresponds to the BH and TCS amplitudes, and $m_N$ is the nucleon mass. The polarized nucleon cross sections also depends on the angles between the nucleon spin vector and the reaction plane, $\phi_S$ and $\theta_S$. We display in Fig. 6 the particular cases of a spin along the z-axis ($\theta_S = 0°$), along the x-axis ($\theta_S = 90°$ and $\phi_S = 0°$) and along the y-axis ($\theta_S = 90°$ and $\phi_S = 90°$). In this experiment, the target is transversely polarized, and the polarized cross sections depends on $\phi_S$, and is calculated for $\theta_S = 90°$.

The TCS amplitude reads

$$T^{TCS} = -\frac{e^3}{q'^2}\, \bar{u}(k)\, \gamma^\nu\, v(k')\, \epsilon^\mu(q)\, H^{TCS}_{\mu\nu}, \tag{2}$$

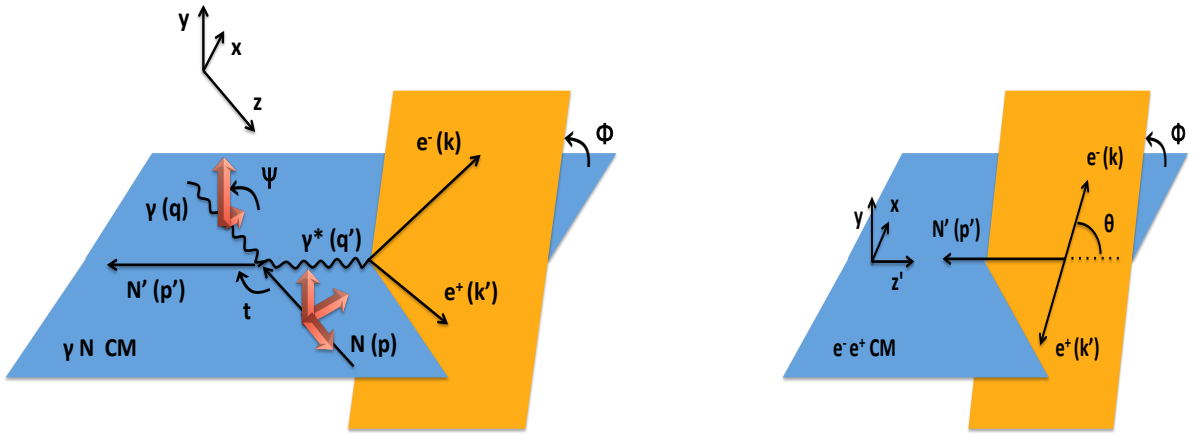


Figure 6: Scheme of the TCS reaction in the nucleon-photon center of mass frame (left panel) and in the virtual photon rest frame (right panel). The momentum of incoming and outgoing nucleon, real and virtual photon, electron and positron are indicated by letters p, p', q, q', k and k', respectively. Left panel: we indicated the angle $\phi_{CM}$ between the lepton decay plane and the reaction plane. We also indicated by red arrows the possible orientations of beam and target spin. Right panel: $\phi_{CM}$ angle is conserved in the boost from $\gamma N$ to $\gamma^*$ C.M. frames. $\theta_{CM}$ is the angle between the lepton direction and the boost axis, defined by the $\gamma^*$ direction in the $\gamma N$ C.M. frame.

with, at the asymptotic limit,

$$
\begin{aligned}
&H^{TCS}_{\mu\nu} \qquad (3)\\
&= \frac{1}{2}\,(-g_{\mu\nu})_\perp \int_{-1}^{1} dx\,\left(\frac{1}{x-\xi-i\epsilon}+\frac{1}{x+\xi+i\epsilon}\right).\left(H(x,\xi,t)\bar{u}(p')\not{n}u(p)+E(x,\xi,t)\bar{u}(p')i\sigma^{\alpha\beta}n_\alpha\frac{\Delta_\beta}{2m}\,u(p)\right)\\
&-\frac{i}{2}(\epsilon_{\nu\mu})_\perp \int_{-1}^{1} dx\,\left(\frac{1}{x-\xi-i\epsilon}-\frac{1}{x+\xi+i\epsilon}\right).\left(\tilde{H}(x,\xi,t)\bar{u}(p')\not{n}\gamma_5\,u(p)+\tilde{E}(x,\xi,t)\bar{u}(p')\gamma_5\frac{\Delta.n}{2m}\,u(p)\right),
\end{aligned}
$$

where we used the metric:

$$
\begin{aligned}
&(-g_{\mu\nu})_\perp = -g_{\mu\nu}+\tilde{p}_\mu n_\nu+\tilde{p}_\nu n_\mu\ , \qquad (4)\\
&(\epsilon_{\nu\mu})_\perp = \epsilon_{\nu\mu\alpha\beta}\,n^\alpha\,\tilde{p}^\beta.
\end{aligned}
$$

The GPDs entering Eq. 3 are proton GPDs, i.e. they read, in terms of quark flavors:

$$
H_{TCS}(x,\xi,t) \;=\; \frac{4}{9}H^{u/p} \;+\; \frac{1}{9}H^{d/p} \;+\; \frac{1}{9}H^{s/p}. \qquad (5)
$$

We use the decomposition into GPDs and notations from Ji [4], and the GPD parametrizations from the VGG model [20, 21, 6, 22], which are summarized in Ref. [8] and based on the Radyushkin double- distribution ansatz for the ($x$,$\xi$)-dependence [23, 24, 3] and on the Reggeized ansatz for the $t$-distribution [6, 22].

The BH amplitude can be expressed as

$$
T^{BH} = -\frac{e^3}{\Delta^2}\,\bar{N}\,\Gamma^\nu\,N\,\epsilon^\mu(q)\,\bar{u}(k)\,\left(\gamma_\mu\frac{\not{k}-\not{q}}{(k-q)^2}\gamma_\nu+\gamma_\nu\frac{\not{q}-\not{k}'}{(q-k')^2}\gamma_\mu\right)\,v(k'), \qquad (6)
$$

where the 4-vectors q, k, k' respectively correspond to the photon, the electron and the positron, N is the nucleon spinor and $\Delta$ is the proton momentum transfer. The virtual photon-proton electromagnetic vertex matrix can be expressed as a function of Dirac ($F_1$) and Pauli ($F_2$) form factors

$$
\Gamma^\nu = \gamma^\nu\,F_1(t)+\frac{i\sigma^{\nu\rho}\Delta_\rho}{2\,m_N}\,F_2(t), \qquad (7)
$$

We use the electric form factor parametrization from [25] and magnetic form factor parametrization from [26].

More details about the formalism entering the calculations used in this proposal are presented in [9].

## 2.2 Observables: calculations

### 2.2.1 Unpolarized cross section

Using a real circularly polarized photon beam and a transversely polarized target, there are 6 independent observables that can be accessed from the TCS+BH reaction. However, we restrict this study to the unpolarized and single polarized cross section as intended to be measured, i.e. 4 independent observables. The double spin asymmetries can be measured as well, but their interpretation is complicated by a strong BH contribution to the asymmetry and a relatively small TCS and interference contribution. In addition, a finer binning in the observables would be required.

We display on Fig. 7 the TCS and BH unpolarized cross section as a function of $\phi$ for various $\theta$ angles. In the analysis, we will integrate the cross sections over $\theta$ in a range depending on the kinematics (this point will be discussed in section 4.2).

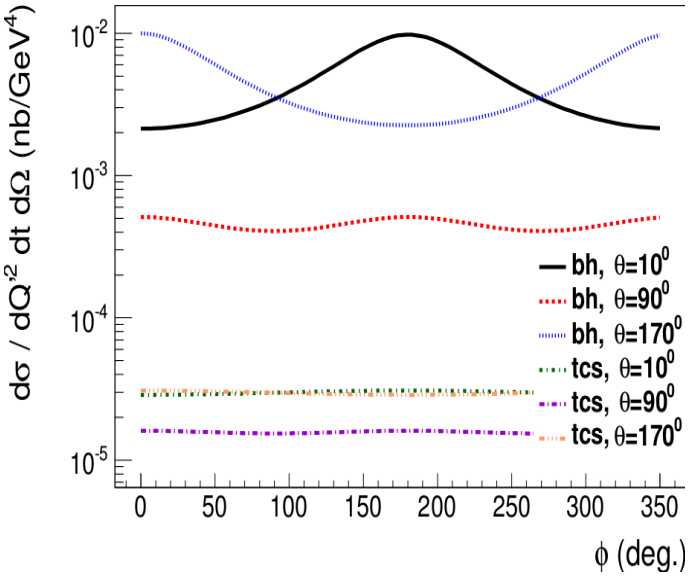


Figure 7: BH and TCS cross sections as a function of $\phi$ at $Q'^2$ = 7 GeV$^2$, -t=0.4 GeV$^2$, $\xi$=0.2, for $\theta_{CM} = 10°$, $\theta_{CM} = 170°$ and $\theta_{CM} = 90°$.

We use the following notations for the observables:

- We use the notation for an asymmetry $A_{PP'}$, with two indices $P$ and $P'$. The first index $P$ refers to the polarization type of the beam: $U$ for an unpolarized beam, $P = \odot$ and for a circularly polarized beam. The second index $P'$ refers to the polarization of the target and can take the values $U$ (unpolarized), $x$ ($\phi_S = 0°$), $y$ ($\phi_S = 90°$), or $T$ for any generic value of $\phi_S$.

- Similarly, we use the notation $\sigma_{PP'}$ for polarized cross sections and $\Delta\sigma_{PP'}$ for polarized

cross section differences, defined as the difference of polarized cross sections $\sigma_{PP'}$, with spin vectors pointing in opposite directions.

### 2.2.2 Circularly polarized beam spin asymmetry

We define the circularly polarized beam spin asymmetry as

$$A_{\odot U} = \frac{\sigma^+ - \sigma^-}{\sigma^+ + \sigma^-}, \tag{8}$$

where $\sigma^{\pm}$ stand for the 4-fold differential cross sections $\frac{d\sigma}{dQ'^2\, dt\, d\phi\, d(cos\theta)}$ for the two photon circular polarization states (right and left polarized). We display in Fig. 8 (left panel) our results for $A_{\odot U}$ as a function of $\phi$ at $Q'^2 = 7$ GeV$^2$, $\xi = 0.2$, $-t = 0.4$ GeV$^2$ for $\theta$ integrated over $[45°, 135°]$. This observable is sensitive to the imaginary part of the amplitude, and therefore BH doesn't produce any asymmetry since its amplitude is purely real. The observed asymmetry therefore reflects a contribution from TCS. We show in [9] the integration over $\theta$ does not strongly reduce the signal, and that we obtain a relatively large (∼20%) sin($\phi$)-shape asymmetry for the explored kinematics. In Fig. 8 (right panel), we show for $\xi = 0.2$, $Q'^2 = 7$ GeV$^2$, $\phi = 90°$ and $\theta$ integrated over $[45°, 135°]$, the $t$-dependence of $A_{\odot U}$. The results Fig. 8 (both figures) are displayed using different GPD parametrizations for TCS. We notice that the magnitude of $A_{\odot U}$ increases with $|t|$ and that there is a sensitivity of this observable to all four GPDs, especially at large $\mid t \mid$. We also display in this figure our calculation with the factorized ansatz for the $t$-dependence of the $H$ GPD in order to illustrate the model-dependence of our results. Since this beam spin asymmetry is sensitive to the imaginary part of TCS+BH amplitudes, its GPD dependence is contained in the imaginary part of CFFs.

### 2.2.3 Transversely polarized target spin asymmetries

We define the transversely polarized target spin asymmetries as

$$A_{Ui} = \frac{\sigma^+ - \sigma^-}{\sigma^+ + \sigma^-}, \tag{9}$$

where $\sigma^{\pm}$ stands for the 4-fold differential cross sections $\frac{d\sigma}{dQ'^2\, dt\, d\phi\, d(cos\theta)}$ for the two target spin orientations $+$ and $-$ along the axis $i = x, y$ or any other $\phi_S$ direction with $\theta_S = 90°$.

We show in Fig. 9 our results for the $\phi$-dependence of $A_{Ux}$ and $A_{Uy}$ for $Q'^2 = 7$ GeV$^2$, $\xi = 0.2$, $-t = 0.4$ GeV$^2$ and for $\theta$ integrated over $[\frac{\pi}{4}, \frac{3\pi}{4}]$. The TCS is calculated with differents GPDs parametrizations. We observe $\sin\phi$ or $\cos\phi$ shapes with amplitudes between 10 and 15%. Like for $A_{\odot U}$, the BH doesn't produce any asymmetry and any non-zero asymmetry directly reflects the strength of GPDs. We show in Fig. 10 the $t$-dependence of $A_{Ux}$ and $A_{Uy}$ at $\phi$=90° and 0° respectively, for the kinematics $\xi = 0.2$, $Q'^2 = 7$ GeV$^2$ and $\theta$ integrated over $[\frac{\pi}{4}, \frac{3\pi}{4}]$. In this figure,

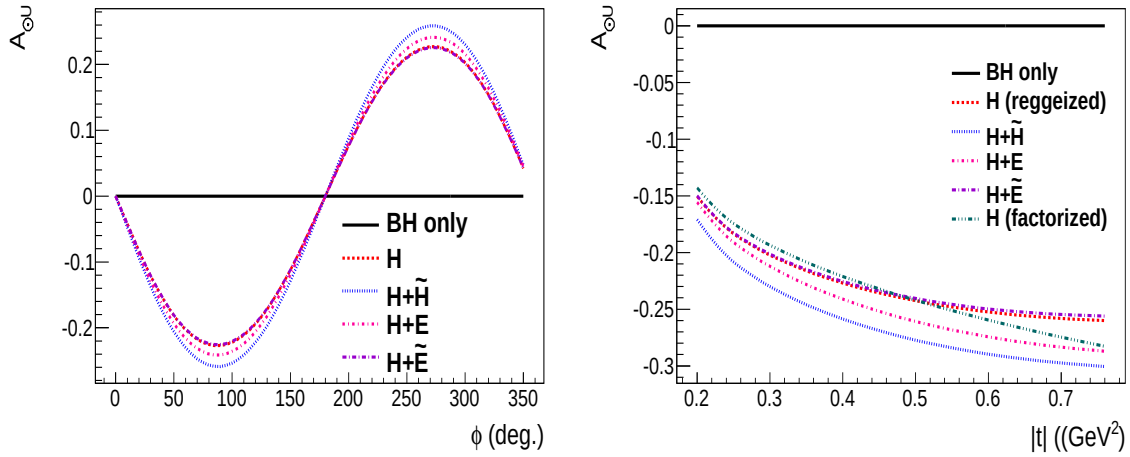


Figure 8: Left panel: The $A_{\odot U}$ for $\theta \in [45°, 135°]$ using different GPD parametrizations for TCS. The calculations are done for $Q'^2 = 7$ GeV$^2$, $\xi = 0.2$, $-t = 0.4$ GeV$^2$. Right panel: The $A_{\odot U}$ asymmetry as a function of $t$ for BH+TCS at $\xi = 0.2$, $Q'^2 = 7$ GeV$^2$, $\phi = 90°$ and $\theta$ integrated over $[45°, 135°]$. TCS is calculated with different GPD parametrizations. From [9].

TCS is calculated with different GPD parametrizations. Depending on the value of $t$, the two asymmetries are sensitive to the GPDs $H$, $\tilde{H}$ and $E$ in various proportions. We also display in this figure our calculations with the factorized ansatz for the $t$-dependence of the $H$ GPD in order to illustrate the model-dependence of our results. Experimentaly, we access different values of $\phi_S$, which are taken into account in the calculation of the polarized cross sections for our projections (in section 4.6).

## 2.3 Interpretations

### 2.3.1 Relations between cross sections and Compton Form Factors for TCS and DVCS

Analytic equations have been developed for the unpolarized and circularly beam polarized TCS+BH [10]. According to this work, the squared TCS amplitude, summed over the initial and final photon spin states is expressed as a function of CFFs, and is proportional to (using our notations) [10]

$$TCS^2 \propto (1-\xi^2)\left(|\mathcal{H}|^2 + |\tilde{\mathcal{H}}|^2\right) - 2\xi^2 \Re\left(\mathcal{H}\mathcal{E} + \tilde{\mathcal{H}}\tilde{\mathcal{E}}\right), \qquad (10)$$
$$-(\xi^2 + \frac{t}{4m_N^2})|\mathcal{E}|^2 - \xi^2 \frac{t}{4m_N^2}|\tilde{\mathcal{E}}|^2.$$

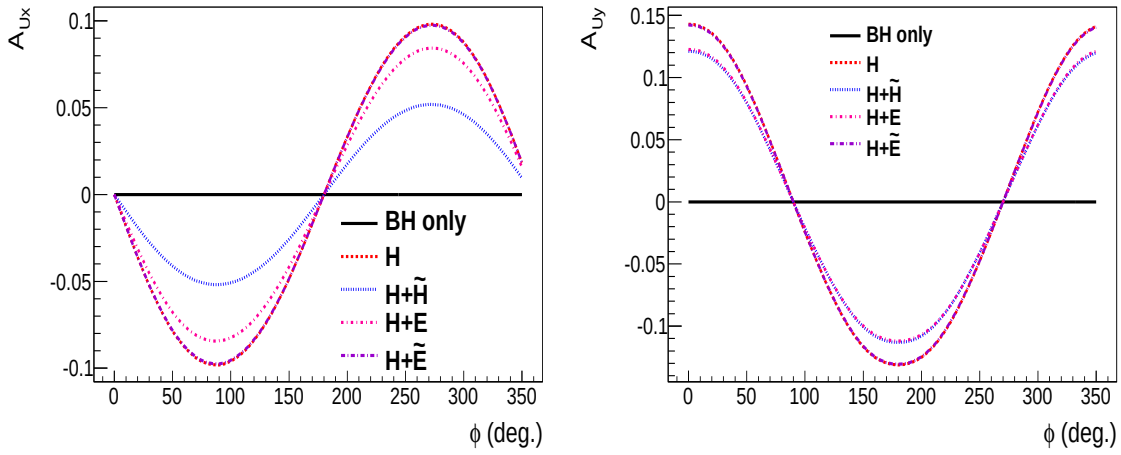


Figure 9: The $A_{Ux}$ (left panel) and $A_{Uy}$ (right panel) asymmetries as a function of $\phi$ for $\xi = 0.2$, $Q'^2 = 7$ GeV$^2$, $-t = 0.4$ GeV$^2$ and for $\theta$ integrated over $[\frac{\pi}{4}, \frac{3\pi}{4}]$. TCS is calculated with different GPD parametrizations. From [9].

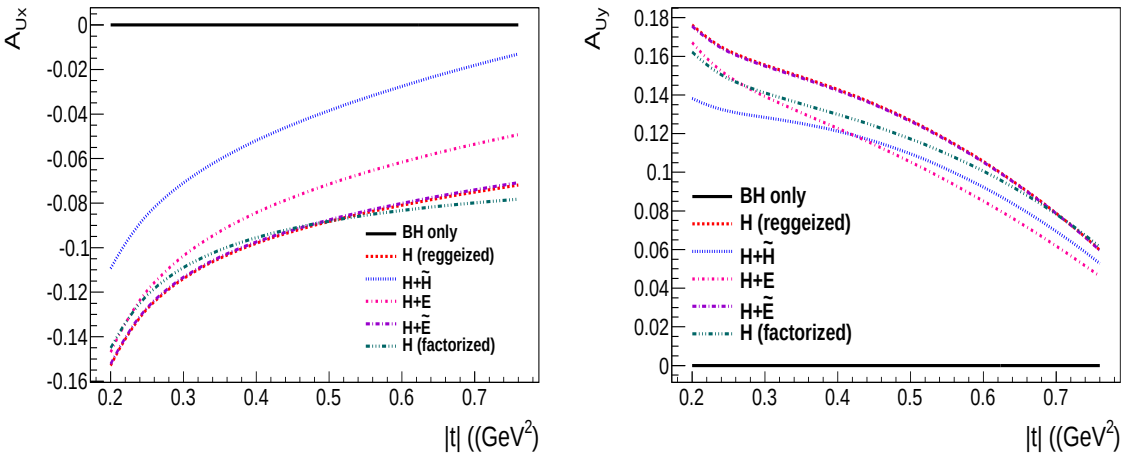


Figure 10: The $A_{Ux}$ (left panel) and $A_{Uy}$ (right panel) asymmetries as a function of $t$, at $\phi$=90°, 0° and 90° respectively, and for $\xi = 0.2$, $Q'^2 = 7$ GeV$^2$, $-t = 0.4$ GeV$^2$ and $\theta$ integrated over $[\frac{\pi}{4}, \frac{3\pi}{4}]$. TCS is calculated with different GPD parametrizations. From [9].

The dominant sin($\phi$) amplitude term ($M^{--}$) of the circularly beam polarized cross section decomposes into CFFs and FFs, and is proportionnal to [10]

$$M^{--} \propto F_1\mathcal{H} - \xi(F_1 + F_2)\tilde{\mathcal{H}} - \frac{t}{4m_N^2}F_2\mathcal{E}. \tag{11}$$

One can notice the similarities with the DVCS polarized cross sections decomposition into CFFs (see reviews [7, 27]). However, the terms depending on GPDs in TCS observables are occurring with different kinematical factors compare to DVCS. Based on the QCD factorization theorems, DVCS and TCS should access the same matrix elements at leading order and leading twist. Therefore, DVCS and TCS depend on the same CFFs (up to a sign change for the imaginary part) and carry the same information on GPDs. We therefore expect the DVCS and TCS observables being correlated at this order: the TCS unpolarized cross section is partially correlated to the DVCS one, whereas the TCS circularly polarized beam spin asymmetries are correlated to the DVCS lepton beam polarization asymmetries which access the imaginary part of amplitudes. Similarly, concerning target polarization, the DVCS and TCS single target spin asymmetries are correlated and access the imaginary part of amplitudes, the DVCS and TCS (with circularly polarized photon) double spin asymmetries are correlated and access the real part of amplitudes.

Although there is no published reference displaying the CFF dependences of the transversely polarized TCS observables, ongoing studies with quantitative predictions will be soon available [28]. Our calculations show a first order sin($\phi - \phi_S$) dependence of the single spin asymmetries which can be related to the DVCS $\phi$ and $\phi_S$ dependence of transverse target spin asymmetries (up to a sign change). DVCS phenomenology [29], results from the HERMES collaboration on transversely polarized DVCS, our results on GPD dependence of $A_{UT}$ (Figs. 9 and 10) suggest an enhanced sensitivity to $\Im\mathcal{E}$ from the (cos($\phi$)sin($\phi - \phi_S$)) moment of the transverse target spin asymmetry. Therefore, $\phi$-dependent transversely polarized target cross section measurements will access $\Im\mathcal{E}$, in addition to $\Im\mathcal{H}$ and $\Im\tilde{\mathcal{H}}$.

### 2.3.2 Higher twist and higher order effects, impact on the observables

In the above discussion, we neglect the impact of higher twist and next to leading order effects on the observables. These however might impact the possibility to access the same CFFs with DVCS and TCS. Higher twist effects have been found to be non negligible from recent JLab DVCS experiments [30]. A preliminary study of TCS [9] suggested that their impact on the observables might be small compared to the leading order GPD contributions. However, a complete study including all higher order corrections has not beed published yet for TCS. Next to leading order calculations of DVCS+BH and TCS+BH show a different NLO structure for the two reactions [31], and small but non negligible effects are expected on the observables.

Depending on the size of higher twist and NLO effects, we will take the following approch for

the interpretation of our results:

- Small effects compared to the uncertainties: we can combine leading order DVCS and TCS observables toward a global CFF fits approach.
- Small or moderate effects compared to the uncertainties: a more thorough analysis of CFFs extracted independently from DVCS and TCS will allow us to put a stringent constraint on the universality of GPDs.
- Large effects compared to the uncertainties: this will lead to the first observation of higher twist effects in TCS (timelike process), which can be compared to higher twist effects in DVCS (spacelike process).

In summary, in the “small effects" scenario, TCS measurements and their comparison to DVCS results will allow us to demonstrate the universality of twist-2 GPDs. If large effects appear, measuring TCS will be an unique opportunity to observe the universality violation for GPDs and their important twist 3 structure [32] in a timelike (TCS) versus a spacelike (DVCS) reaction. Similar studies with TMDs (Transverse Momentum Distributions) lead in particular to the demonstration of an induced sign change for the first moment of azimuthal asymmetries in semi-inclusive reactions (spacelike photon) and in the Drell-Yan reaction (timelike photon) [33], unpredicted at twist 2, and related to the Sivers effect (twist 3 TMD "$f_{1T}^{\perp}$") [34]. This effect can also be related to the GPD E (its projection in impact parameter space), as shown in [35], which will be accessed in our experiment.

## 2.4 Extraction of CFFs from TCS measurements and impact for GPDs

### 2.4.1 Framework

We base the discussion in the current section under the assumption of negligible higher order and higher twist effects. In this case, we access the same CFFs from DVCS and TCS. We can either access the CFFs independently from the two reactions and compare the results, or combine DVCS and TCS observables to do a multi-observable fitting.

We show in Fig. 11 the kinematical domain which can be accessed for DVCS and TCS. We display in blue the ($\xi$, $Q'^2$) phase space accessible for TCS with an 11 GeV electron beam, assuming that the real photon is provided by bremsstrahlung of the electron and that its energy is in $E_\gamma \in [5, 11]$ GeV. We have applied two cuts: $Q'^2 \in [4, 9]$ GeV$^2$ and $-t \in [0, 1]$ GeV$^2$. The motivations are respectively to stay in the region free of vector meson resonances and minimize higher twist corrections to the TCS formalism, which grow with $\frac{t}{Q'^2}$. We overlap in red in this same figure the ($\xi$, $Q^2$) phase space accessible with an 11 GeV beam for DVCS. We have applied the cuts: $-t \in [0, 1]$ GeV$^2$, for the same reason as for TCS, and $s > 4$ GeV$^2$ in order to stay above the baryon resonance region. One notes the large intersection between the DVCS and the TCS phase spaces. In this section, we combine DVCS and TCS observables calculated at the same $\xi$ and t with the

same CFFs (up to a sign change for the imaginary part). As we neglect the $Q^2$ and $Q'^2$ dependence of CFFs, we performed the calculations at two different values, reflecting the average $Q^2$ and $Q'^2$ accessible in DVCS and TCS experiments, respectively.

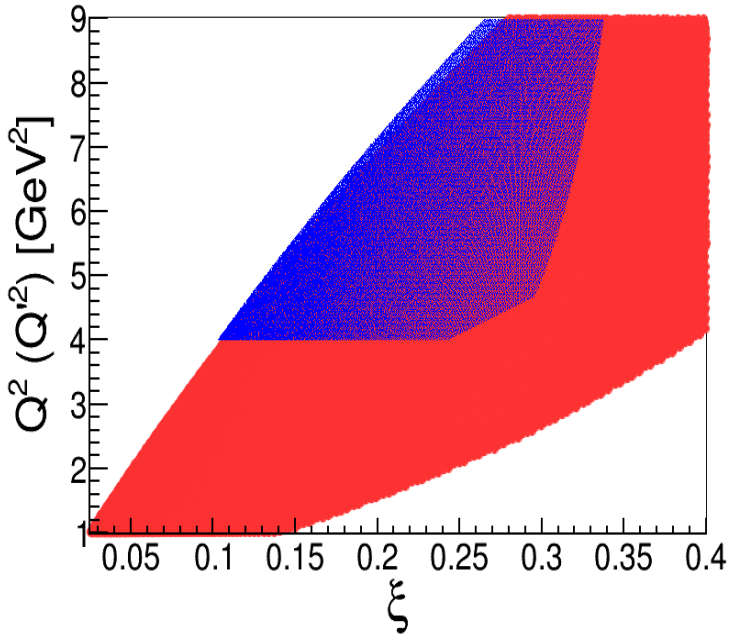


Figure 11: Kinematical domain accessible as a function of $\xi$ and $Q^2$ for DVCS (red plain surface) and in $\xi$ and $Q'^2$ for TCS (blue dotted surface) with an 11 GeV electron beam. For DVCS, the cuts $-t \in [0,1]$ GeV$^2$ and $s > 4$ GeV$^2$ have been applied and for TCS, the cuts $E_\gamma \in [5,11]$ GeV, $-t \in [0,1]$ GeV$^2$ and $Q'^2 \in [4,9]$ GeV$^2$ have been applied. Cuts are purely from the kinematic, and no acceptance cuts are applied in this figure.

### 2.4.2 Fitting method

We generated DVCS+BH and TCS+BH pseudo-data sets based on VGG model for the GPDs and the calculations from [20, 21, 22, 6, 9]. The cross sections are calculated at the same t and $\xi$ for DVCS and TCS: DVCS+BH distributions are generated at t=-0.2 GeV$^2$, $\xi = 0.15$, Q'$^2$ = 2.5 GeV$^2$, E(beam) = 11 GeV, TCS+BH distributions are generated at t=-0.2 GeV$^2$, $\xi = 0.15$, Q$^2$ = 4.5 GeV$^2$, $\theta_{CM}$ = 90°. The distributions are presented as a function of 16 bins in $\phi$. In case of transversally polarized protons, we generated the polarized cross sections at $\phi_S = 0°$ (proton spin along the x-axis) and at $\phi_S = 90°$ (proton spin along the y-axis). We extracted the CFFs following to the fitting method from [36]. In order to match the uncertainties expected in short term experiments at JLab, and to compare DVCS and TCS in the same conditions, we set relative errors of 5% per bin in $\phi$ for both DVCS+BH and TCS+BH unpolarized cross sections. We set relative errors of 7% per bin in $\phi$ for all the polarized cross sections. We assume the same uncertainties for both reactions

in order to compare the sensitivities to CFFs. The free parameters of the fits are the 7 Compton Form Factors: $\Im(\mathcal{H})$, $\Im(\tilde{\mathcal{H}})$, $\Im(\mathcal{E})$, $\Re(\mathcal{H})$, $\Re(\tilde{\mathcal{H}})$, $\Re(\mathcal{E})$, $\Re(\tilde{\mathcal{E}})$ (we neglect $\Im(\tilde{\mathcal{E}})$ as in [36]). Figures of the fitted distributions and more details about the method are given in Appendix A.

We performed fits on the sets of observables presented on table 1. For configurations 1 to 5, we systematically performed fits for DVCS and TCS independently, and combining both reactions. For the configurations 6, 6', 6'', we fitted observables from DVCS, TCS, DVCS+TCS, respectively (the symbol "x" in the table indicate configurations that are not fitted). In the table we used the notations corresponding to DVCS observables: the first index "L" for designing DVCS+BH beam spin asymmetries should be replace by an index "$\odot$" in case of TCS (circularly polarized beam).

We indicated experimental Halls in JLab who have experiments accessing the different observables. Some of these experiments are running or approved to run in a short term. Complementary DVCS experiments at JLab (12 GeV) include the experiments [37, 38, 39] aiming at measuring the unpolarized and beam polarized DVCS cross sections, the experiment [38] will also measure the longitudinally polarized target single and double spin asymmetries, and the conditionally approved experiment [17] aims at measuring the transverse target spin asymmetries. Complementary TCS experiments at JLab (12 GeV) include the experiments [2] (running) and [1] (future) aiming at measuring the unpolarized and circularly beam polarized cross section of TCS, from a quasi-real photon beam (the incoming beam is a longitudinally polarized 11 GeV electron). The experiment we are proposing will measure the unpolarized and circularly beam polarized cross section, but initiated from a real photon at about $10^2$ times the photon intensity of [2] and at about 10 times the photon intensity of [1]. It will measure in addition the transverse target spin asymmetries.

The extracted CFF uncertainties are presented on Fig. 12 (imaginary parts) and 13 (real parts).

#### 2.4.3 Interpretation on fitting DVCS or TCS independently

Measuring only the unpolarized cross section and beam spin asymmetry either from DVCS+BH or from TCS+BH (with a circularly polarized beam for TCS) allow for extracting $\Im\mathcal{H}$, $\Im\tilde{\mathcal{H}}$, and $\Re\mathcal{H}$ with a good enough precision for contributing to constrain GPD models and for comparisons between the two processes (Fig. 14). Having in addition the longitudinal target spin asymmetry allow for constraining better these CFFs, in particular $\Im\tilde{\mathcal{H}}$, and allow for bringing some constraint on $\Re\tilde{\mathcal{H}}$.

Having in addition to the unpolarized cross section and the beam spin asymmetry, the two independent transverse target spin asymmetries allow to constrain in addition $\Im\mathcal{E}$ (Fig. 14). Thanks to the correlations between the CFFs and the fact of having more independent observables to constrain the fits, a much better precision is reached for $\Re\mathcal{H}$ compared to cases without transverse

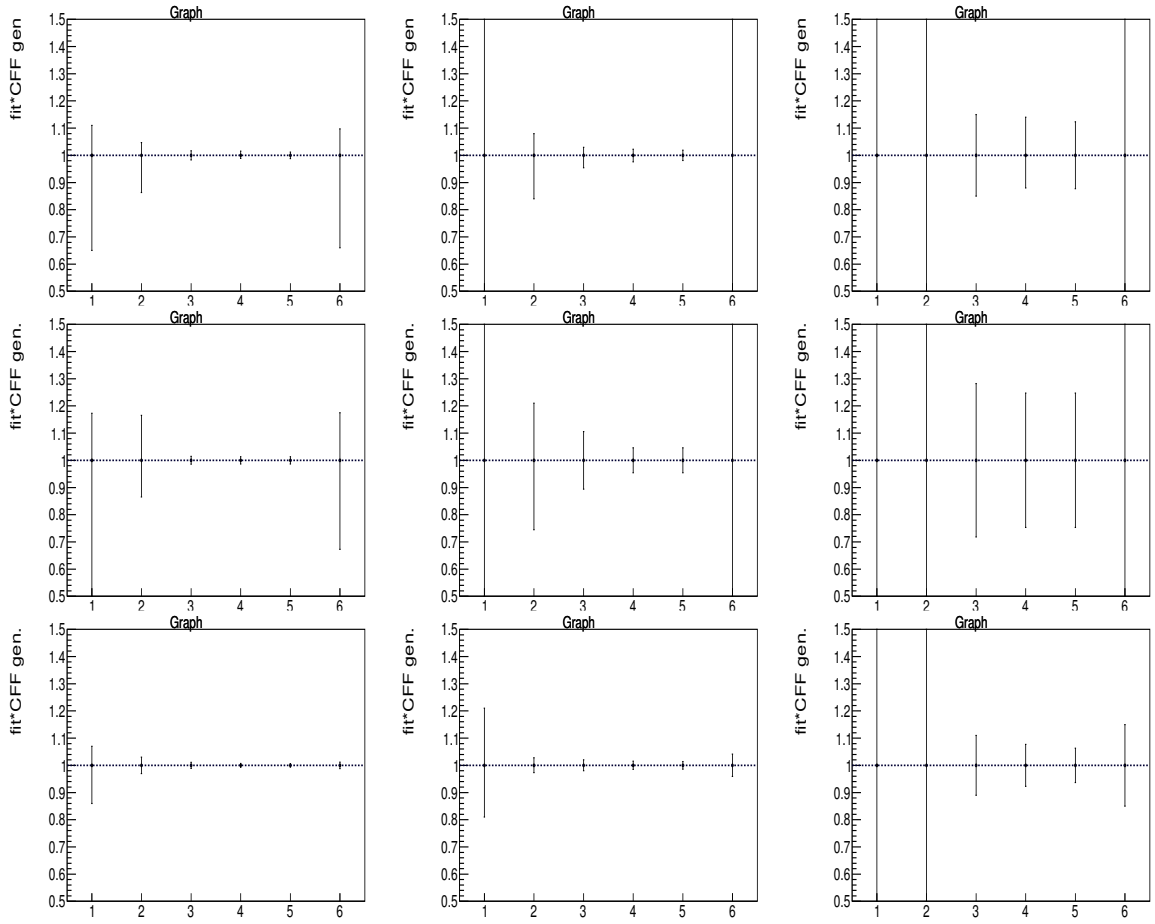


Figure 12: Extracted coefficients for imaginary part of CFFs, defined as fit result * generated CFF. Left column: Im($\mathcal{H}$), central column: Im($\tilde{\mathcal{H}}$), right column: Im($\mathcal{E}$). Top: extracted from DVCS, central row: extracted from TCS, bottom row: extracted from DVCS+TCS. Set of observable indices (from 1 to 6) are detailed in table 1. The scale is zoomed, fitting coefficient variation has been limited to $[-5, 5]$ time the generated one. The generated coefficient (1) is indicated by the black dashed line. For visibility, we allow data points with uncertainties larger than the displayed vertical range. The uncertainties are based on pseudo-data azimuthal distribution fitting with the assumption of 5% error per bin for the unpolarized cross section and 7% per bin for the polarized cross section, with 16 bins in $\phi$.

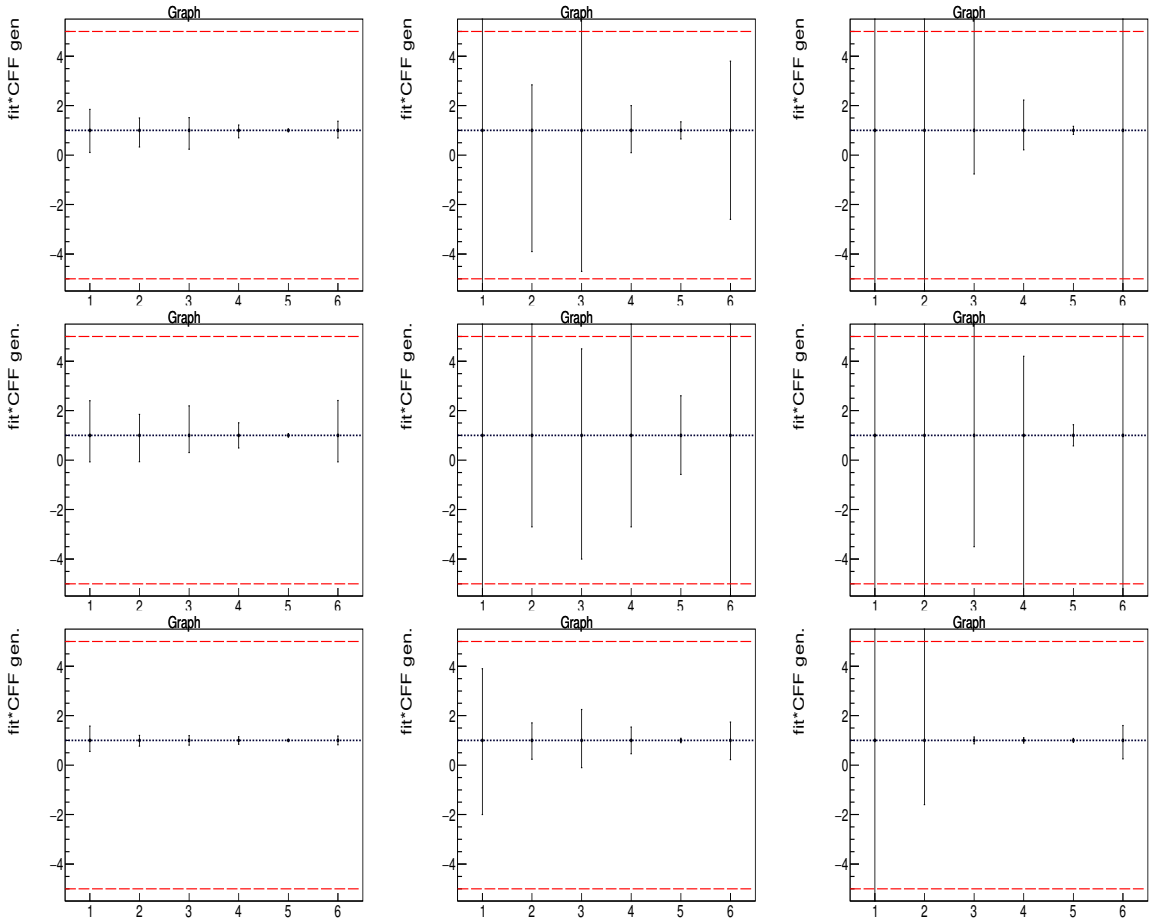


Figure 13: Extracted coefficients for real part of CFFs, defined as fit result * generated CFF. Left column: Re($\mathcal{H}$), central column: Re($\tilde{\mathcal{H}}$), right column: Re($\mathcal{E}$). Top: extracted from DVCS, central row: extracted from TCS, bottom row: extracted from DVCS+TCS. Set of observable indices (from 1 to 6) are detailed in table 1. Fitting coefficient variation has been limited to $[-5, 5]$ times the generated one. These limits are indicated by the red dashed lines. Generated coefficient (1) is indicated by the black dashed line. The uncertainties are based on pseudo-data azimuthal distribution fitting with the assumption of 5% error per bin for the unpolarized cross section and 7% per bin for the polarized cross section, with 16 bins in $\phi$.

| Set of observables | DVCS | TCS | DVCS+TCS | # independent obs. (DVCS/TCS/both) |
|---|---|---|---|---|
| 1) $\sigma$, $\Delta\sigma_{LU}$ | A, B, C | A, B, **C** | A, B, **C** | 2/2/2 |
| 2) $\sigma$, $\Delta\sigma_{LU}$, $\Delta\sigma_{UL}$, $\Delta\sigma_{LL}$ | B | | | 4/4/4 |
| 3) $\sigma$, $\Delta\sigma_{LU}$, $\Delta\sigma_{UT}$ (x2) | B$^{(*)}$ | **C** | B+C$^{(*)}$ | 4/4/4 |
| 4) $\sigma$, $\Delta\sigma_{LU}$, $\Delta\sigma_{UT}$ (x2) $\Delta\sigma_{UL}$, $\Delta\sigma_{LL}$ | | | | 6/6/6 |
| 5) $\sigma$, $\Delta\sigma_{LU}$, $\Delta\sigma_{UT}$ (x2) $\Delta\sigma_{UL}$, $\Delta\sigma_{LL}$, $\Delta\sigma_{LT}$ (x2) | | | | 8/8/8 |
| 6) $\sigma$, $\Delta\sigma_{LU}$, $\Delta\sigma_{C}$ | | x | x | 3 (DVCS) |
| 6') $\sigma$, $\Delta\sigma_{\odot U}$, $\Delta\sigma_{LU}$ | x | | x | 3 (TCS) |
| 6") 2) of DVCS + 3) of TCS | x | x | B+**C** | 6 (DVCS+TCS) |

Table 1: First column: set of combined observables for DVCS, TCS and DVCS+TCS fitting. Second to fourth column: current and future experiments at JLab accessing these observables (letters indicate experimental Halls, the letter **C** in bold corresponds to this proposal). Note that the projected uncertainties of these experiments are not corresponding to the one assumed in this exercise, done in the purpose of comparing DVCS and TCS in the same conditions. Fifth column: number of uncorrelated observables. $^{(*)}$) this CLAS12 experiment is conditionally approved.

target asymmetries (Fig. 14).

Fitting DVCS+BH or TCS+BH unpolarized cross sections, beam polarized cross sections, 3 single target polarized cross sections (1 longitudinal, 2 transverse), and the double beam and longitudinaly polarized target cross sections (case 4) bring constraint to $\Im\mathcal{H}$, $\Im\tilde{\mathcal{H}}$, $\Im\mathcal{E}$, $\Re\mathcal{H}$, $\Re\tilde{\mathcal{H}}$ and $\Re\mathcal{E}$. Adding the double beam and transverse target spin asymmetries with the same precision (case 5) will strongly shrink the uncertainties for all the CFFs and avoid incorrect solutions to the problem, thanks to it being overconstrained. The CFF $\Re\tilde{\mathcal{E}}$ is constrained thanks to correlations with other CFFs. This case is not corresponding to any short term DVCS or TCS experiments, and represent an ideal case of what can be achieved according to the uncertainties we set and the method.

We notice that in a scenario of same uncertainties on DVCS and TCS observables, the sensitivities to CFFs of DVCS observables are stronger the sensitivities of TCS observables. Indeed, TCS is more suppressed than DVCS compared to the associated BH process in the reaction. However, we can constraint CFFs from the two reactions independently and compare the results for studies of GPDs universality.

#### 2.4.4 Interpretation on fitting simultaneously DVCS and TCS

For the first 5 sets of observables, we fitted simultaneously correlated observables from DVCS and from TCS (Fig. 12). These simultaneous fits allow for about a factor of 2 reduction of error bars compared to the case of fitting only DVCS. This reduction is larger than statistically expected, due

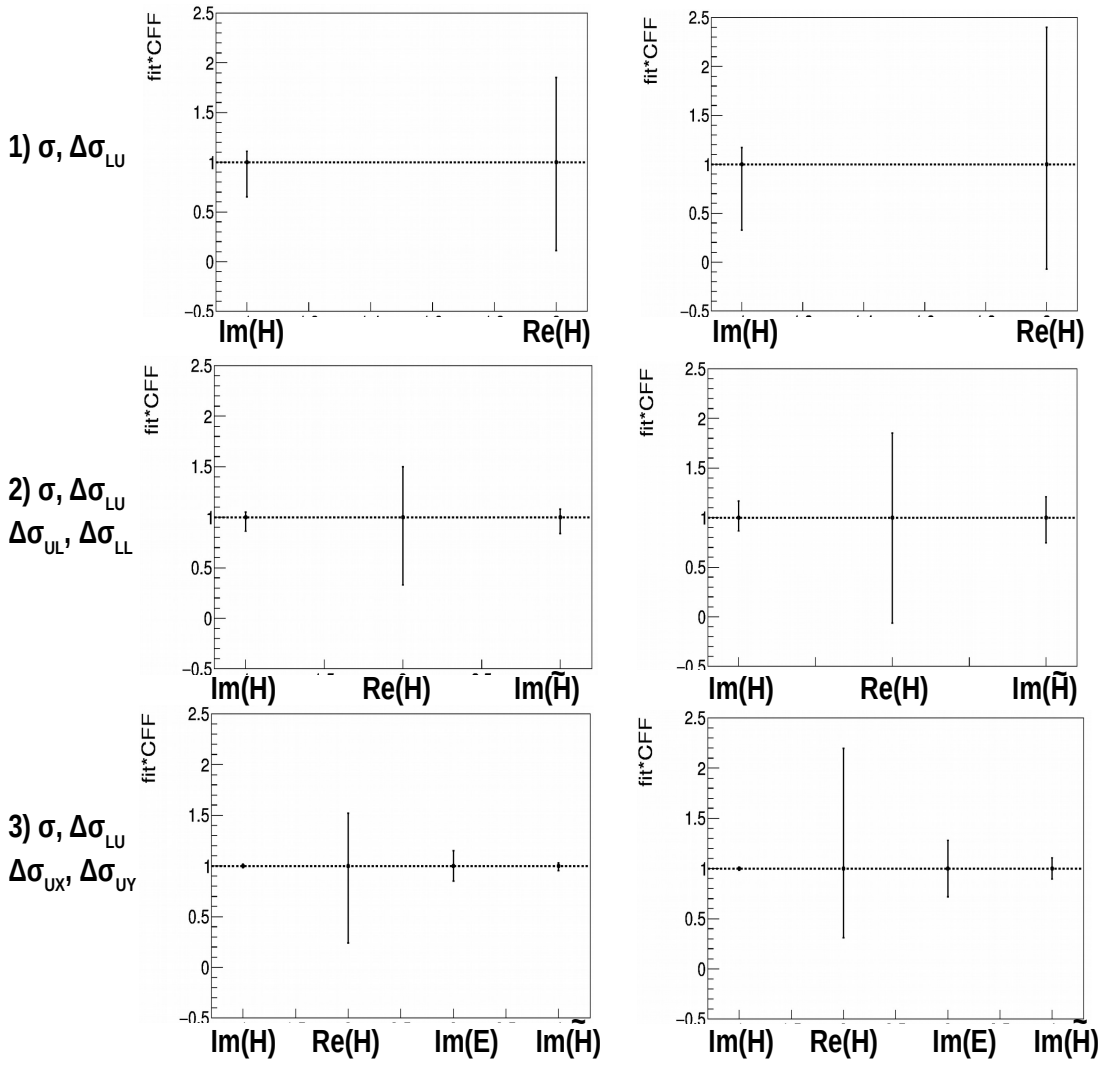


Figure 14: Extracted CFFs from DVCS (top row) and TCS (bottom row), using $\sigma$ and $\Delta\sigma_{LU}$ (top row), using $\sigma$, $\Delta\sigma_{LU}$, $\Delta\sigma_{UL}$, $\Delta\sigma_{LL}$ (center row) and using $\sigma$, $\Delta\sigma_{LU}$, $\Delta\sigma_{UX}$, $\Delta\sigma_{UY}$ (bottom row). This experiment corresponds to the bottom row right figure (with transversely polarized TCS). The uncertainties are based on pseudo-data azimuthal distribution fitting with the assumption of 5% error per bin for the unpolarized cross section and 7% per bin for the polarized cross section, with 16 bins in $\phi$.

to the fact that the unpolarized cross sections are not fully correlated and therefore they bring both some new information. Combining observables from both reactions can help at a non negligible level in constraining GPD models by reducing uncertainty and allowing for extraction of CFFs which would be hard to constrain otherwise.

The data set 6" (for DVCS+TCS) is a combination of DVCS $2^d$ data set and TCS $3^d$ data set, corresponding to a scenario of CLAS12 DVCS data (with longitudinal target) combined to the results of our experiment. Independent information is brought by the different target polarization accessible in these experiments. Combining these data sets allow for constraining at the same time all CFFs.

Even though simultaneous fits are assuming GPD universality and neglect higher twist effects, they allow for bringing strong constraints to GPD models with short term upcoming DVCS and TCS experiments, compared to measurement from DVCS only.

### 2.4.5 Neutron measurements and flavor decomposition for the GPDs

The results of sec. 2.4.3 demonstrate the feasibility of accessing CFFs and GPDs for the proton from DVCS and TCS measurements. However, for interpretations, GPDs have to be decomposed into flavor, which is possible thanks to measurements of the GPDs of the neutron in other experiments [40, 41] in addition to the measurements off the proton. In particular, the CFF $\Im\mathcal{E}$ for the neutron is accessible with the unpolarized and the beam polarized DVCS cross section measurements [40] and the longitudinaly polarized experiment [41] using the CLAS12 spectrometer. As shown on Fig. 15, the neutron DVCS measurement will complement the TCS measurement we are proposing for the flavor decomposition of the GPD E, with uncertainties on the CFF at the same level.

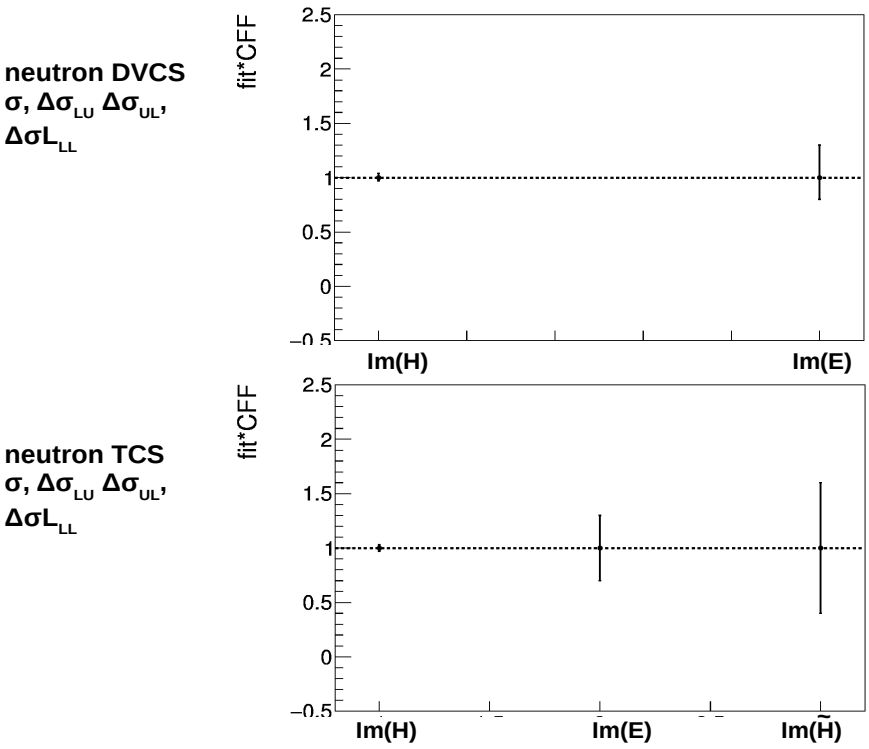


Figure 15: Extracted CFFs from DVCS (left column) and TCS (right column) off the neutron, using $\sigma$, $\Delta\sigma_{LU}$, $\Delta\sigma_{UL}$, $\Delta\sigma_{LL}$. The uncertainties are based on pseudo-data azimuthal distribution fitting with the assumption of 5% error per bin for the unpolarized cross section and 7% per bin for the polarized cross section, with 16 bins in $\phi$.

# 3 Experimental setup

## 3.1 The concept of setup

The setup is aimed at detection of decay lepton pair and recoil proton from BH/TCS events in triple coincidence, in forward kinematics. The key components of the setup are high intensity photon source, a transversely polarized proton target, and a set of detectors for proton and lepton detection and identification.

The experiment will utilize untagged bremsstrahlung photon beam from Hermetic Compact Photon Source (CPS) ([12]) on the UVA/JLab polarized ammonia target ([13, 14]). The CPS is capable of delivering up to $1.5 \times 10^{12}$ photons per second with primary CEBAF electron beam of 11 GeV energy and $2.5\ \mu A$ intensity, within the energy range from 5.5 to 11 $GeV$ ([42]). The photon beam has clear advantage over the electron beam when using the polarized target: less heat load, higher polarization and less depolarization of the target material. This boosts figure of merit for the beam – polarized target combination by factor of $\sim$30. Assuming aforementioned CPS beam intensity, $1.5 \times 10^{23} cm^{-2}$ of polarized hydrogen atoms in the UVA target (3 $cm$ long target cell, 0.6 packing fraction, $0.817 g/cm^3$ density of frozen $NH_3$), the luminosity for this combination may reach $2.2 \times 10^{35} cm^{-2} sec^{-1}$.

To provide transverse polarization, the target assembly will be rotated by 90° around the vertical axis. For this configuration the rendered angular acceptance is $\pm 17°$ horizontally, and $\pm 21.6°$ vertically. The exit beam pipe excludes from angular acceptance a conical region with opening angle of $6°$.

The proposed positioning of detectors optimizes coverage of the remaining angular acceptance in a simple way (Fig.16). The detectors are positioned above and below the exit pipe and span from $6°$ to $21.6°$ vertically, and $\pm 17°$ horizontally. Small adjustments in this coverage due to deflections of the particles in the target magnetic field and background distributions are described below, in Sections 3.4 and 3.5. Positioning at 150 $cm$ from target ensures reasonable transverse sizes of detectors.

The proposed detector package in its minimal configuration consists of hodoscopes for detection of proton, and electromagnetic calorimeters for detection of leptons. The hodoscopes have X and Y planes and measure both transverse coordinates.

The final state of the reaction contains two leptons and a proton, which will provide a coincidence trigger. The exclusivity of the reaction is ensured by detecting all final-state particles, $e^+e^-p$. The secondary photon beam being provided by an untagged initial electron beam, its energy is provided by cutting on the missing particle kinematics.

| Parameters | Calorimeters | Hodoscope |
|---|---|---|
| range in $\phi$ | $\pm 17^o$ | $\pm 17^o$ |
| range in $\theta$ | $6^o$ - $21.6^o$ | $6^o$ - $21.6^o$ |
| | -$6^o$ - $-21.6^o$ | $-6^o$ - $-21.6^o$ |
| $\delta\phi$ | $< 5$ mr | $< 1^\circ$ |
| $\delta\theta$ | $< 5$ mr | $< 1^\circ$ |
| Energy resolution | $\sim 2\%/\sqrt{E}$ | $\sim 10\%$ |
| Time resolution | $< 100$ ps | $< 100$ ps |
| PID: | | |
| e/$\pi$ | $\sim$0.01 | ... |
| $\pi$/p | .... | $\sim$0.1 |

Table 2: Proposed characteristics of the TCS detector setup. $\phi$ denotes angle in horizontal plane, and $\theta$ denotes angle in vertical plane.

The proposed design characteristics of the detectors are presented in Table 2.

The following sub-sections contain more detailed description of the parts of setup, and studies on background conditions and trigger choices.

### 3.2 High Intensity photon beam

The proposed experiment will utilize an untagged photon beam from Hermetic Compact Photon Source (CPS) proposed by G. Niculescu and B. Wojtsekhowski [12]. The bremsstrahlung photons are produced from CEBAF electron beam (maximum energy 11 GeV) impinging on 10% $Cu$ radiator. The electrons after the target bend in 1 $m$ long, 2.2 $T$ field magnet, while photons pass straight through narrow, 2 $mm$ in diameter collimator before reaching target. As bent electrons are dumped in the body of magnet, the whole setup is heavily shielded by $W$-alloy in order to eliminate produced radiation.

The spot size of photon beam at 2 $m$ away from the radiator is estimated to be $\sim$0.9 $mm$. The projected photon flux is $1.5 \times 10^{12}$ $s^{-1}$ for primary electron beam current 2.5 $\mu A$, for photon energies $>$ 0.5 $E_{beam}$ [42].

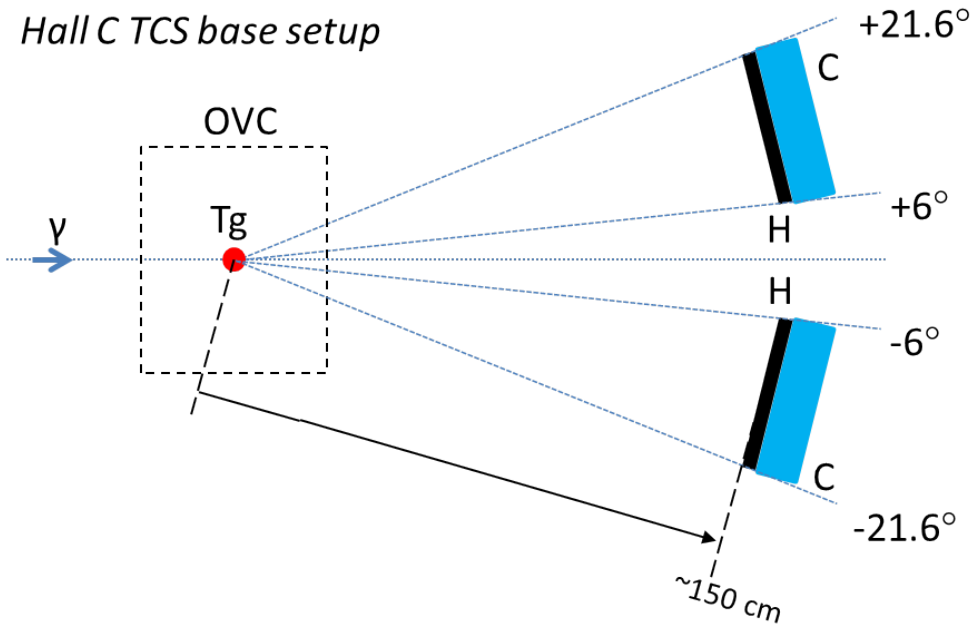


Figure 16: Side view of the TCS experimental setup. Shown are photon beam ($\gamma$), transversely polarized target (Tg) in the scattering chamber (OVC), and pairs of hodoscope (H) and calorimeter (C) counters for detection of the recoil proton and the lepton pair.

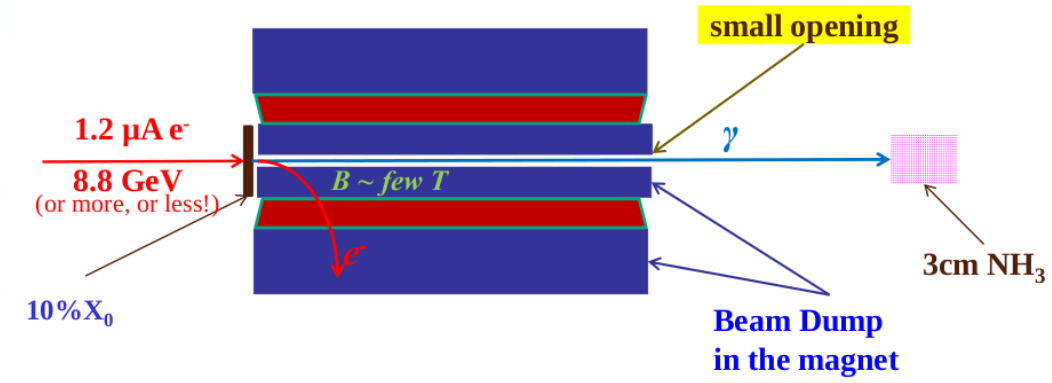


Figure 17: The conceptual design of Hermetic Compact Photon Source.

### 3.3 Polarized Target

Hall C has a long and successful experience with the use of solid polarized targets, starting in 1998 with the first run of E93-026[43] designed to measure the electric form factor of the neutron. This was followed by its second run in 2001 and immediately by the Resonance Spin Structure experiment, E01-006 [44] in 2002 and by the Spin Asymmetries Experiment on the Nucleon (SANE) [45] in 2009. The polarized target was extensively refurbished and modified for successful measurements of $g_2$p and $G_E$p in Hall A [46].

These targets exploit a technique called Dynamic Nuclear Polarization (DNP) in which polarization is transferred from unpaired electrons in a dilute concentration of paramagnetic centers (introduced via irradiation at 80K or by chemical doping). At 5 T and 1K the thermal equilibrium of both species (proton and electron) is determined solely by Boltzmann statistics and can be written as $P = \tanh \frac{\mu B}{kT}$. The TE polarization of the electron under these conditions is 99.8% while the proton is 0.51%, the difference due solely to the size of their respective magnetic moments. The dipole-dipole interaction between the nucleus and the electron spins leads to hyperfine splitting. By applying a RF field with a frequency very close to the electron paramagnetic resonance (EPR) frequency (about 140 GHz at 5.0 Tesla), the high electron polarization (due to the large electron magnetic moment) can be transferred to the proton. Either positive or negative polarization can be achieved, depending on whether the RF field is below or above the EPR frequency.

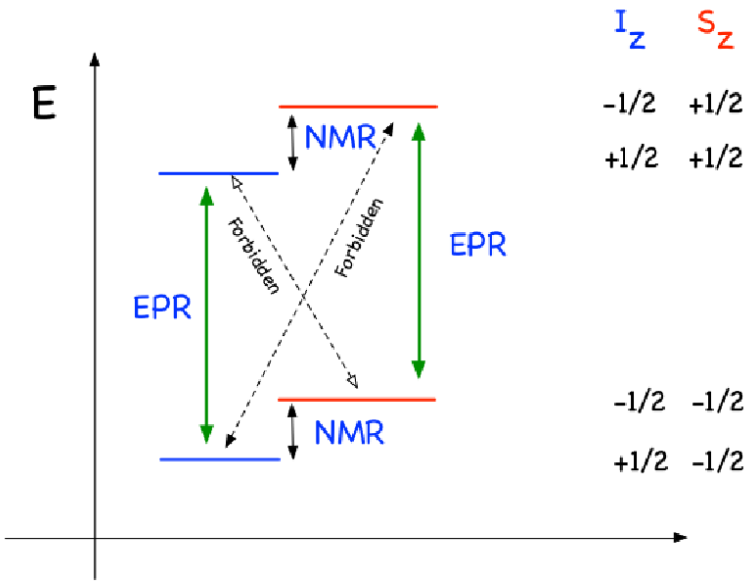


Figure 18: Transitions driven by GHz microwaves in the DNP process

Positive proton polarization results by driving the forbidden transition from the $|S_z, I_z\rangle = |-\frac{1}{2}, -\frac{1}{2}\rangle$ ground state to the $|+\frac{1}{2}, +\frac{1}{2}\rangle$ excited state. The later quickly relaxes to the $|-\frac{1}{2}, +\frac{1}{2}\rangle$

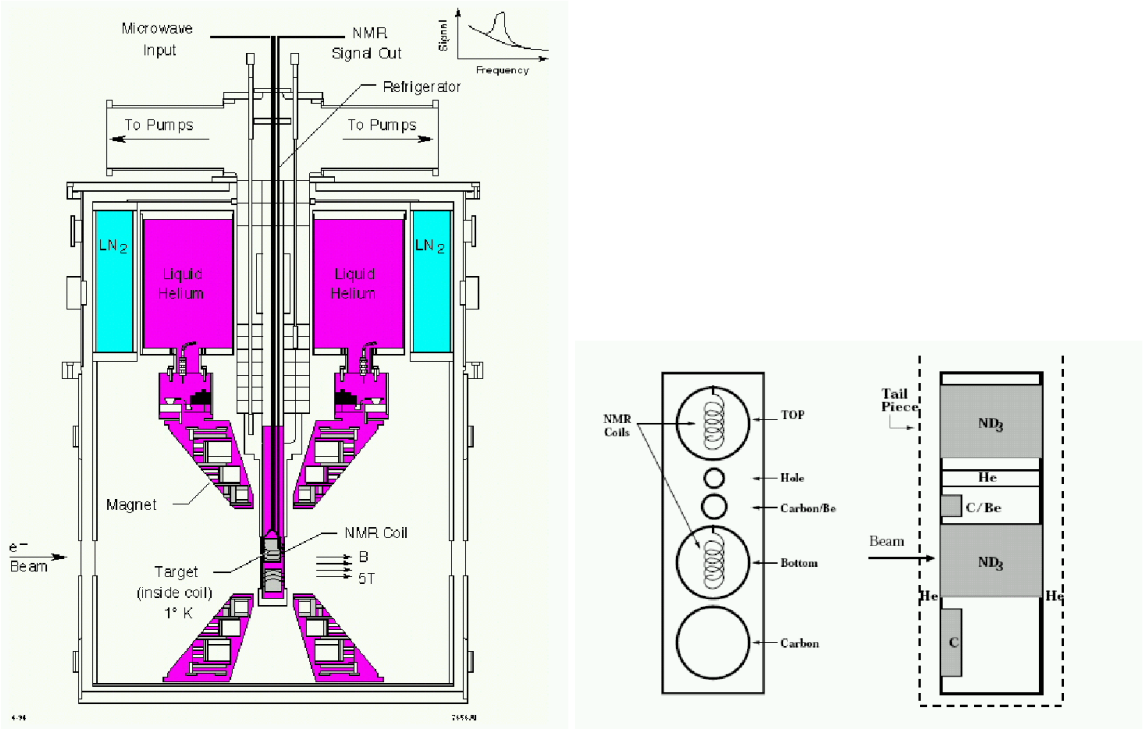


Figure 19: The UVA polarized target used in Hall C experiments. Left:Cross section view of the target. Right: A schematic drawing of the lower part of the target insert. The dashed line represents the tail piece which contained liquid helium during data taking.

ground state via the allowed EPR transition. Driving the other forbidden transition, $|-\frac{1}{2},+\frac{1}{2}\rangle \rightarrow |+\frac{1}{2},-\frac{1}{2}\rangle$, results in negative proton polarization. It is illustrated Figure 18.

The schematic view of the polarized target and the lower part of the target insert are shown in Fig. 19.

The target magnet is a pair of superconducting Helmholtz coils that when driven at 121 Amps produce a magnetic field of 5 Tesla. The coils have a 20 cm central bore, $100^o$ opening angle and 8 cm of coil split. The field is uniform to $10^{-4}$ over the 3 cm diameter right cylinder.

To provide transverse polarization of the target needed in this measurement, the target magnet will be rotated by $90^\circ$ around vertical axis. Restricted by the magnet coils and scattering chamber window, the angular acceptance in this configuration will span $\pm 17^\circ$ horizontally and $\pm 21.7^\circ$ vertically [4].

The target magnetic field direction has been found to be coincident with the geometric axis of the coils and is known to $0.1^\circ$ [47]. The target is cooled by a $^4He$ evaporation refrigerator placed

[4] A version of the target used in JLab Hall A $g_p^2$ experiment E08-027.

vertically in the center bore of the magnet (see Fig. 19). The target material is held in cups at the the end of the target insert which can carry up to 5 targets: a top and bottom $NH_3$, an empty target and 2 solid targets (C or Be).

The microwaves are generated by an Extended Interaction Oscillator tube (Manufactured by CPI, Canada) which has a maximum power of ∼20 W with approximately 1 W delivered to the target sample. $^{15}NH_3$ is chosen as the target material because of its high polarizability, large polarizable nucleon content and resistance to radiation damage.

The target polarization is measured via NMR using the Liverpool Q-meter in which the magnitude of polarization is linearly related with the voltage of the phase sensitive detector: $P = K \cdot S$, and K is a calibration constant. The calibration constant K is determined by measuring the size of a sample's NMR signal under known thermal equilibrium conditions where the polarization can be calculated from the aforementioned Boltzmann statistics. A series of NMR signal area measurements are made and averaged to obtain the calibration constant. They are typically done with each load of target material and as many time as is possible during the run, especially after anneals.

The target material consists of 1-3 mm diameter granules of $NH_3$, immersed a $^4He$ bath inside the target cavity. The packing fraction is the fraction of target cell volume filled by target material $(NH_3)$, the rest of the cell being filled with liquid $^4He$. The packing fraction is important for the simulation of the scattering cross sections and for the determination of the dilution factor.

The dilution factor, $f$, is defined as the fraction of events originating from polarized hydrogen.

Interaction of the beam with the target material produces an abundance of paramagnetic radicals which increase the rate of nuclear spin relaxation, but do not contribute to the DNP process. As a result, the polarization decays with the accumulation of beam charge until the time required to achieve a desired statistical precision becomes unacceptable.

In practice, for experiments using 100 nA electron beam this can occur in about 8 hours. For experiments with photon beam like this one, the radiation damages are less intense and the time is much longer. Fortunately, the process of annealing recombines the paramagnetic centers and restores polarization. To anneal, the target material is moved out of the beam and the polarizing microwave radiation and is heated to between 70-100 K for between 10 and 60 minutes.

The high intensity multi-GeV photon beam causes ionization energy loss by production of electron positron pairs inside the target. The energy loss from this process is approximately independent of beam energy and is estimated to be about 2 $MeV \cdot cm^2/g$.

For a photon intensity of $1.5 \times 10^{12}$ equivalent photons per second, it is necessary to use an evaporation refrigerator with $\sim$1 Watt cooling power in combination with a high polarization, high radiation resistant proton target material ($NH_3$). For electron beam experiments, typically 100 nA is the maximum current on the target. The heat load is about 0.33 W and combined with the DNP microwaves is about 0.5 W. This heat load must be distributed throughout the target so that the target material beads do not experience local depolarization. To do this, the standard fast raster is used to make a $2mm \times 2mm$ square pattern of electrons over the radiator. The resulting photon beam is then distributed over the target by mechanical rotation of the target cell.

A mechanical rotation system is built at UVA which provides rotation rates faster that 1 Hz. The target rotation in combination with the standard target actuator results in an effective slow raster which spirals over the full area of the standard 2.5 cm diameter target. Uniform exposure of the target cell is achieved by a combined rotation of the target cup synchronized with an up/down movement of the target ladder. Rotation of the target cup has already proven viable during the tests at UVa. Depolarization and homogeneous radiation damage can easily be achieved by continuously moving the target at a rate determined by the radius of the circle made through rotation on the target surface, spending no more than a few hundred milliseconds on each set of target beads.

The detailed information about polarized target subsystems, technique of operation and experimental measurements can be found in Ref. [13, 14, 48] and the UVa target group web server Ref.[46, 18].

### 3.4 Lepton detectors

The determination of the kinematic variables $Q'^2$, $\xi$ and $\tau$ depends on the accuracy of reconstruction of the lepton energy and angle. Leptons ($e^+$ and $e^-$) in the experiment will be detected and identified by measuring their energies and coordinates ($X$ and $Y$) in a pair of electro-magnetic calorimeters.

The calorimeters are a copy of the shower counter for the projected Neutral Particle Spectrometer. The basic concept for the NPS is a highly segmented electro-magnetic calorimeter preceded by a compact sweeping magnet. Experiments with NPS require detection of neutral particles with energies ranging between 0.5-7.6 GeV with good energy resolution ($\sim 2\%$), and good coordinate and angular resolution of 0.5-0.75 mrad, the latter being comparable to the resolutions of the focusing spectrometers in Hall C.

An assembly of lead tungstate crystals, similar to HYCAL calorimeter in the PrimEx and PrimEx-II experiments in Hall B [49] is recognized as a good match for the NPS calorimeter (see Fig 20). Preparation work for construction of the NPS calorimeter is well underway. Tests are being curried out at CUA and JLab to characterize optical and radiation-resistive properties of $PbWO_4$ crystals from SICCAS and other sources, a small prototype detector of $3 \times 3$ crystal assembly has been built for studies.

The new active divider design of the PMT bases provides a linear response up to high rates of $\sim$1 MHz. More information about the NPS and design studies can be found in reference [50].

The calibration procedures developed in PrimEx experiment can be adapted to this project. Experience with the HYCAL yielded energy and coordinate resolutions of $\sigma/E = 1.3\%$ and $\sigma_x$ $\sim$1.28-2.10 mm at a neutral-pion energy of 5 GeV, giving an invariant mass distribution with a width of 2.3 MeV/$c^2$ (see Fig, 21). For comparison, an energy resolution of 2.2% for incident electrons of $\sim$4 GeV energy has been obtained in beam tests with the prototype in Hall D at JLab.

The transverse size of the TCS lepton detectors is driven by required angular acceptance and distance to the target. Restricted by the target setup angular acceptance is $\pm 17^\circ$ in horizontal plane and $\pm 21.7^\circ$ in vertical plane (see Section 3.3). In addition, the beam pipe restricts scattering angles to greater than $6^\circ$. Taken into account vertical deflections of the particles to be detected in the sideways magnetic field of the target, we consider positioning the lepton detectors above and below the beam pipe, at $0^\circ$ of azimuthal angle.

Reasonable sizes for the detectors are obtained by positioning them at a distance $\sim$1.5 m from the target. This implies $92 \times 41.5\ cm^2$ of active area, for the angular acceptances $\pm 17^\circ$ horizontally and $\pm 15.7^\circ$ vertically. For $PbWO$ crystals of $2.05 \times 2.05\ cm^2$ cross section for construction, the num-

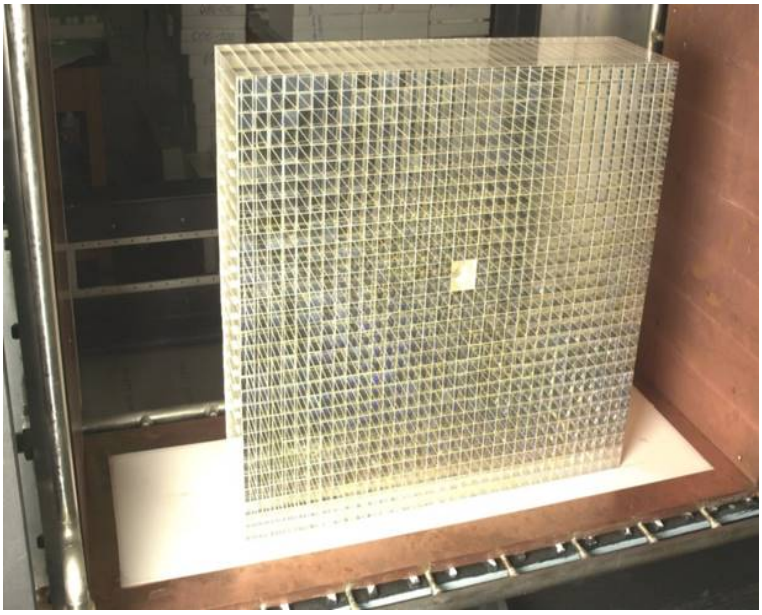

Figure 20: $2.05 \times 2.05 \times 18 cm^3$ $PbWO_4$ crystals used in the high resolution part of Hall B PrimEx experiment calorimeter (HYCAL) [49].

ber of modules would be $\sim$1000 for each detector (taken into account addition of a layer around the perimeter of cross-sectional area to exclude shower leaks). This number was refined after simulated acceptance studies, according to which a 50 $\times$ 23 matrix arrangement would be optimal, with 1150 blocks per detector. A further refinement took place due to background simulations, according to which the central region of detectors covering $\pm 1.6^\circ$ horizontally must be excluded from consideration, because of unacceptably high background rates (see Section 3.6 below).

Hence the final layout of the calorimeters consists of 4 quarters (top left, top right, bottom left, bottom right), 23 $\times$ 23 matrix of blocks each, mirroring each other horizontally and vertically. The horizontal gap between left and right quarters is 8.2 $cm$ wide, the vertical gap is 15.8 $cm$ wide. The number of required lead tungstate crystals totals to 2,116.

### 3.5 Detection of recoil protons

Determination of momentum transfer -t and its resolution depends on accuracy of reconstruction of the recoil proton four momentum. Design requirements for the proton detectors are defined by kinematics, required accuracy, available space and cost, as well as by the expected background conditions. The recoil detectors will be located just before the lepton detectors and will cover a slightly larger angular area than allowed by the polarized target. Similar to the calorimeters' case (see Section 3.4), the horizontal band from -6° to 6° and vertical band $\pm 1.6^\circ$ at the middle of the acceptance will be excluded, and the detector will be divided in 4 separate partitions.

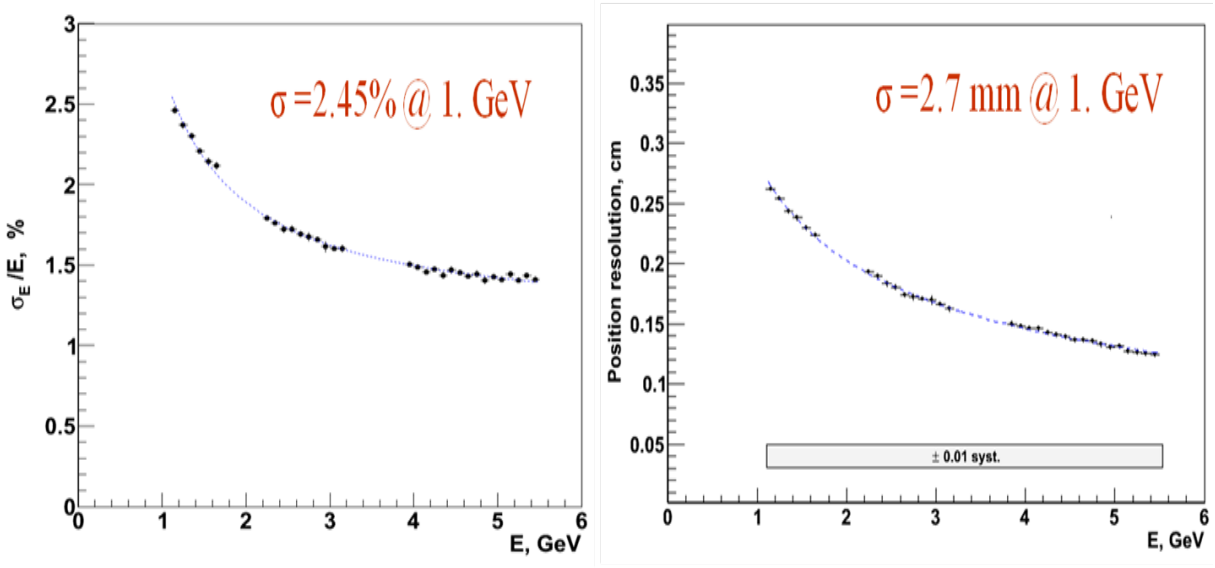


Figure 21: Energy and coordinate resolutions of $PbWO_4$ crystals based HYCAL calorimeter.

The proposed 4 proton detectors have hodoscopic construction. Each hodoscope consists of $X$ and $Y$ planes, and cover rectangular area of $50 \times 48\ cm^2$. The counters will be made of scintillator bars. The width and thickness of the bars will be optimized for accuracy of the track coordinates' determination, and for particle identification capabilities of the detectors.

The detected proton momenta will be within $0.3 - 1.2\ GeV/c$ range, with bulk of statistics between 0.4 and 0.8 GeV/c. Proton identification will be based on $dE/dx$ signal from the hodoscopes. Thickness of at least few $cm$ will be needed for reliable separation of protons and lighter particles at momenta $\sim$1 $GeV/c$ (Fig. 22).

### 3.6 Background and trigger studies

For experiments with open geometry setups, background conditions are of special importance. This experiment will utilize a bremsstrahlung photon beam of intensity, potentially as high as $2 \times 10^{13}$ photons per second on target of 3.8% radiation length. Simple PDG based estimates for $e^+e^-$ $\gamma$-conversion production alone yields $3\%/\gamma$ probability, i.e. rates in $\sim 10^{11} Hz$ range, even a small portion of which in the acceptance may cause difficulties.

A Geant4 based simulation code was developed to study background conditions, and detector acceptances as well. The code models the target assembly (scattering chamber with its windows and shieldings, target cell and target material, magnet coils, magnetic field) and detector pack-

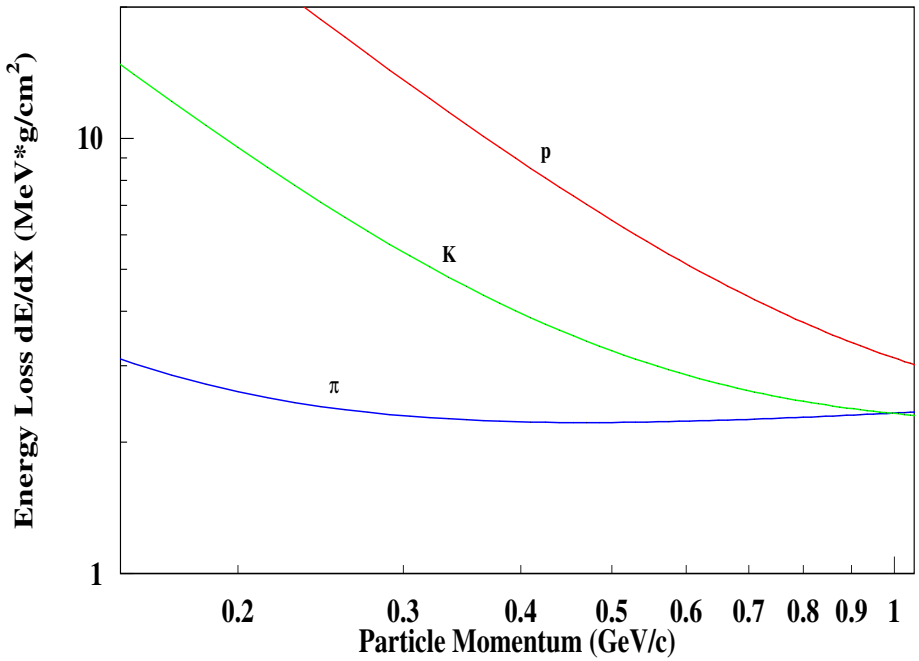


Figure 22: Proton PID by $dE/dx$ in the Recoil Proton Detector. The graph shows ionization energy losses versus momentum for pions, kaons and protons.

age. The background events in the detectors were generated by passing bremsstrahlung photons through the target assembly. The photon energy was sampled from the bremsstrahlung spectrum with endpoint energy of 11 GeV.

A custom made, fast c++/Root code for acceptance studies was also helpful in this case. The code features a pointlike target, target magnetic field, target chamber and detector acceptances.

It was found that among background tracks within the detector acceptances ∼90% are $\gamma$-s, ∼10% are electrons and ∼0.2% are positrons. The hadron content is small. Deposited in the calorimeters energies are mostly below 200 MeV (Fig.23). While vast majority of energetic electrons and positrons from $\gamma$-conversion in the target material fall into the gap in the middle of acceptance, some of them hit the calorimeters and deposit energies in GeV range.

The transverse magnetic field from the target deflects charged background toward detectors. The middle of acceptance is particularly affected with high background rates (Figures 24 and 25). The high energy background tend to concentrate there. The rates vary several times from the middle of acceptance to the edges.

We note here that there is a room to optimize hodoscope configuration for both efficiency of the recoil proton detection and background rate reduction. High rates in the hodoscope counters can be reduced by a finer segmentation of the detectors. Energy loss by the recoil proton in 1 $cm$ scintillator is above 2.4 $MeV$, hence background rates in Fig.25) can be reduced, as our simulations show by 4 times, by raising the threshold energy. Thicker counters would allow for easier selection of efficient thresholds.

For construction of a viable low level trigger, identification of the ranges of useful events is necessary. For loose cuts on the TCS kinematic variables of interest $9\ GeV^2 > Q^2 > 4\ GeV^2$, $-t < 1\ GeV^2$, $s > 4\ GeV^2$, $-t/Q^2 < 0.3$, the momenta of leptons from detected BH events are greater than 1 $GeV$, and the sum of lepton momenta is greater than 5 $GeV$. By establishing those thresholds on the deposited energies in the calorimeter, one can reduce rates of $e^+e^-$ background coincident events by 3 orders of magnitude, but still leave them in $10^5\ Hz$ range (Fig. 27).

A more sophisticated trigger can be constructed requiring that the sum of transverse momenta of the 3 detected particles be equal to ∼0. One can look for combinations of the measured quantities that are proportional to the transverse momenta, are easy to implement in the trigger, and construct the sum. For instance, the X component of the lepton transverse momentum can be represented by $X$ coordinate of the hit cluster in the calorimeter, weighted by the energy of the cluster $E$. Then, assuming one lepton hit the top calorimeters, another the bottom calorimeters, one can look for a pair of hit clusters with significant energy deposition, calculate the energy weighted coordinates for them, and take the sum of the two quantities as a representation of the transverse momentum of the decayed outgoing photon:

$$P_X(\gamma^\star) \sim X_+E_+ + X_-E_- \tag{12}$$

The same procedure can be applied to the $Y$ coordinate, but with taking into account a caveat: contrary to the previous case, the leptons bend in axis direction. This results in a constant term in the expression for the sum:

$$P_Y(\gamma^\star) \sim Y_+E_+ + Y_-E_- + const \tag{13}$$

Such constructed quantities for the triple coincidence BH/TCS events are constrained within ranges of $\pm 50\ GeV{\cdot}cm$ ($X$ component), and from $-100\ GeV{\cdot}cm$ to $50\ GeV{\cdot}cm$ ($Y$ component) (Fig.28). The dips in distributions correspond to gaps between parts of the calorimeters' assembly.

### 3.7 Acceptance and reconstruction

The coincidence trigger between all the final state particles of the reaction helps reduce the background. We suppress the background from the two-pion photoproduction by setting a cut on the two leptons energy of 300 MeV. The exclusivity of the reaction is ensured by detecting all final-

state particles, $e^+e^-p$ and cutting on the missing-particle kinematics. We use an 11 GeV energy electron beam incident on 10% radiator to produce high intensity real photons (see Section 3.2). Highly collimated photons will interact with transversely polarized protons (solid ammonia $NH_3$) yielding luminosities up to $L = 10^{35}$ cm$^{-2}$ sec$^{-1}$. A pair of electromagnetic NPS-type calorimeters will be used for detection of leptons, determination of their energies, and for e/$\pi$ separation. A pair of recoil detectors will be used to detect protons. These detectors will be combined Hall C basic electronics and DAQ. The experimental setup is shown in Fig. 16.

The generated lepton and proton tracks are traced through the magnetic field of the target, then scattering chamber window up to the detectors at 1.5 m distance from target. As target field is oriented sideways relative to the beam direction, the tracks are deflected up and down. The track bending happens close to the target, for the field being localized within ∼15 cm space at target. The fringe fields do not affects significantly the tracks. The high momentum electrons deflect by only $\sim 2^\circ$. While for protons, with momenta from 0.3 to 1.5 GeV/c the bending angle is $\sim 15^\circ - 30^\circ$, typically, and may reach $45^\circ$.

Positions and sizes of the lepton and proton detectors and trackers are chosen to match the outgoing track directions (see Sections 3.1, 3.5, 3.4). We display in Fig.29 the t-distribution of accepted events applying a tagging of the two leptons only (left pane, blue curve), and applying in addition a tagging of the proton (left panel, red curve). The ratio of the curves (right panel) illustrates the impact on the acceptance of the proton tagging.

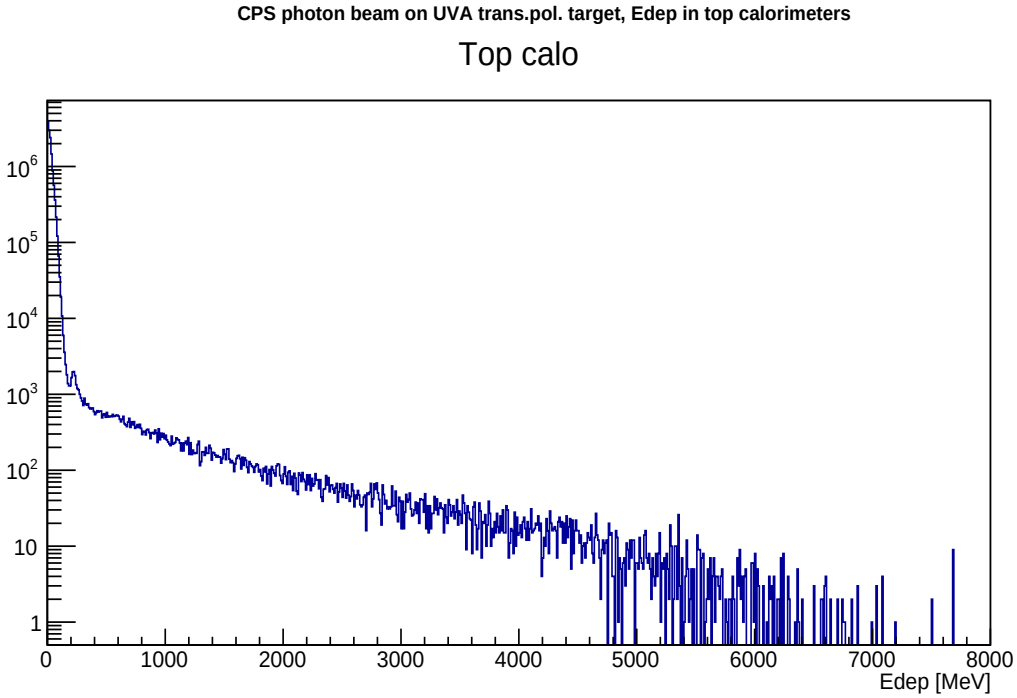


Figure 23: Background energy deposition in the Top calorimeters. The energy deposition in the Bottom calorimeters has similar distribution.

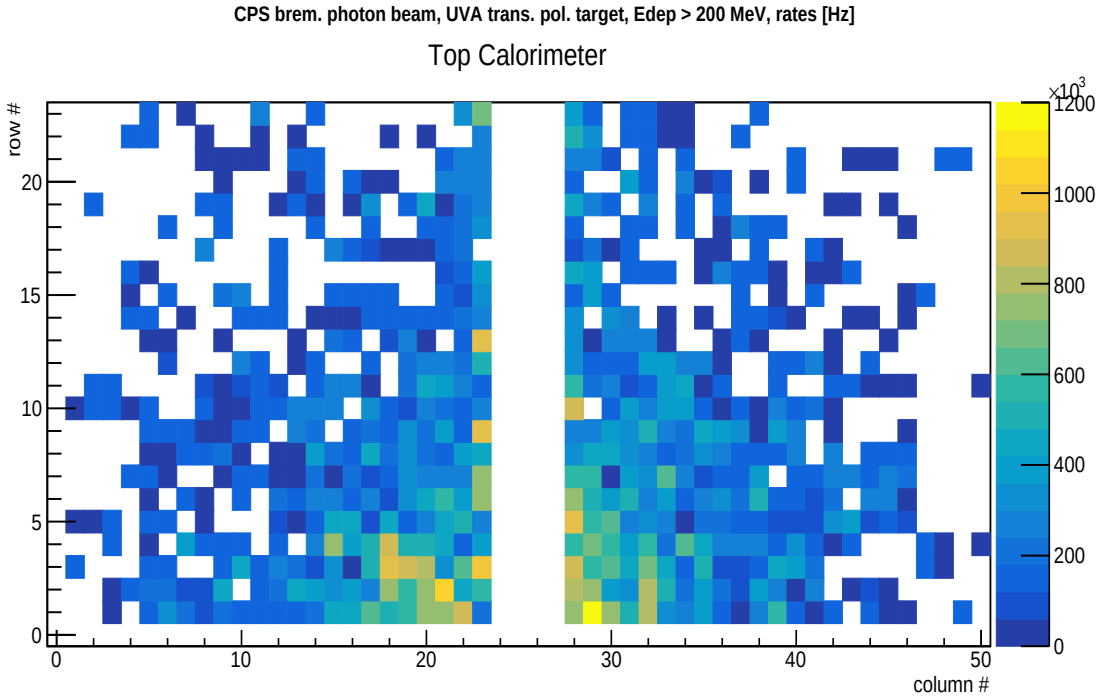


Figure 24: Background rates in the modules of Top calorimeters. Hits with deposited energies greater than 200 MeV are counted. The pattern in the Bottom calorimeters is similar.

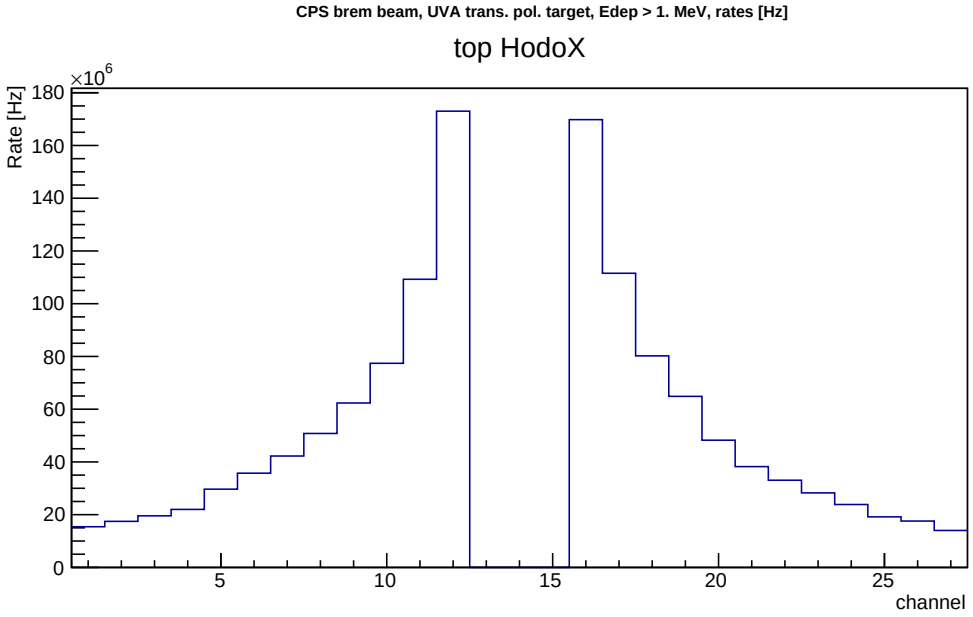


Figure 25: Background rates in the paddles of Top X hodoscopes. The scintillator paddles are 1 $cm$ thick, 4 $cm$ wide. Hits with deposited energies greater than 1 MeV are counted. Rates in the Bottom X hodoscopes are similar.

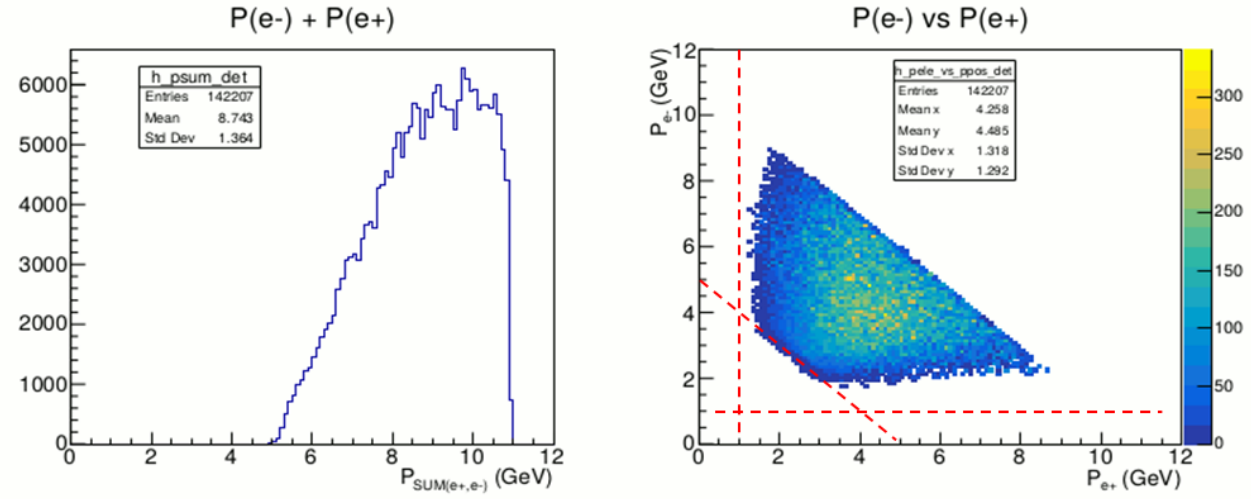


Figure 26: Lepton momenta of Bethe-Heitler events within acceptance of the TCS setup. Left: Sum of the momenta. Right: electron momentum versus positron momentum. The dashed lines indicate thresholds on the electron and positron momenta greater than 1 GeV, and sum of the two greater than 5 GeV.

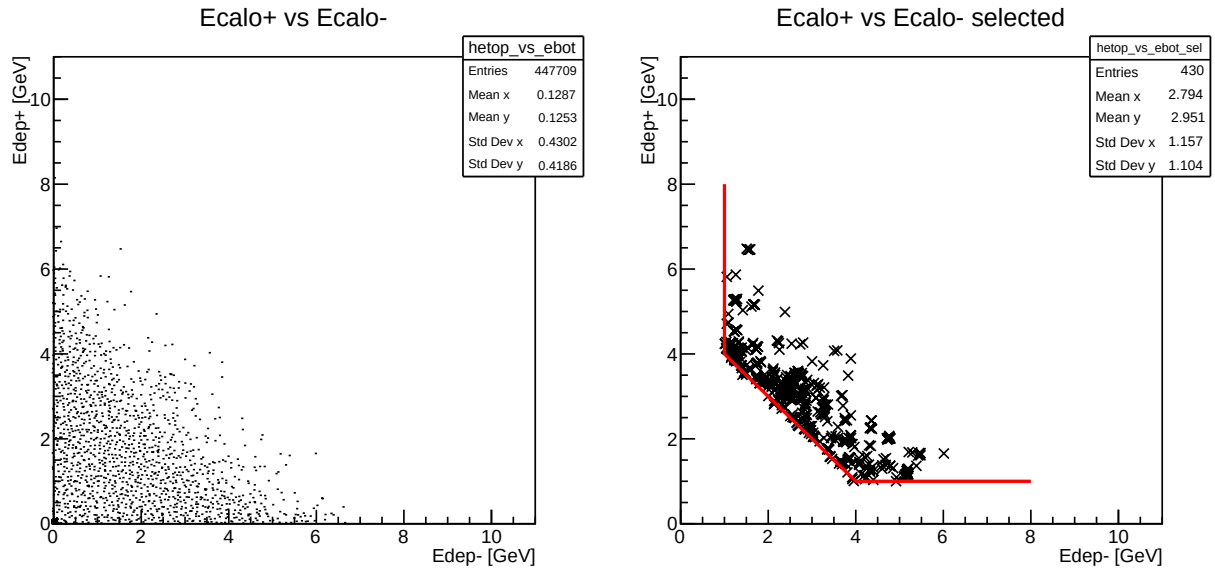


Figure 27: Background coincidence events in the calorimeters. Left: energy deposition in the top calorimeter versus energy deposition in the bottom calorimeter. Right: same for events surviving threshold cuts on the deposited energies.

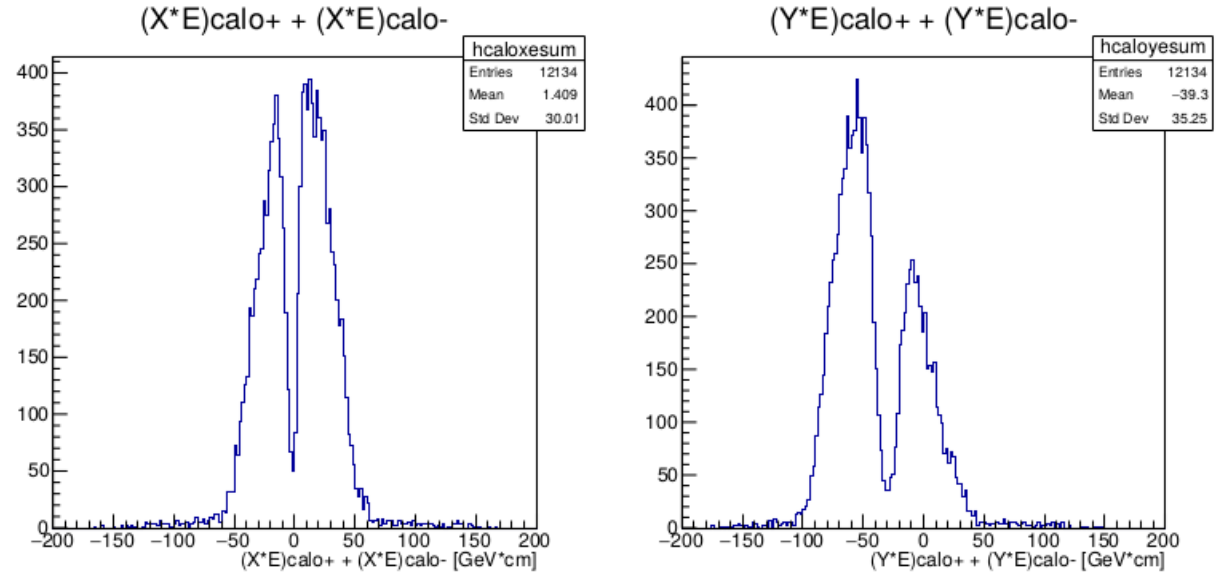


Figure 28: Weighted by deposited energy coordinates of hit clusters from leptons hitting the calorimeters, for BH/TCS events detected in the setup. Left: sum of the weighted X coordinates from top and bottom calorimeters. Right: same for the Y axis. See text for details.

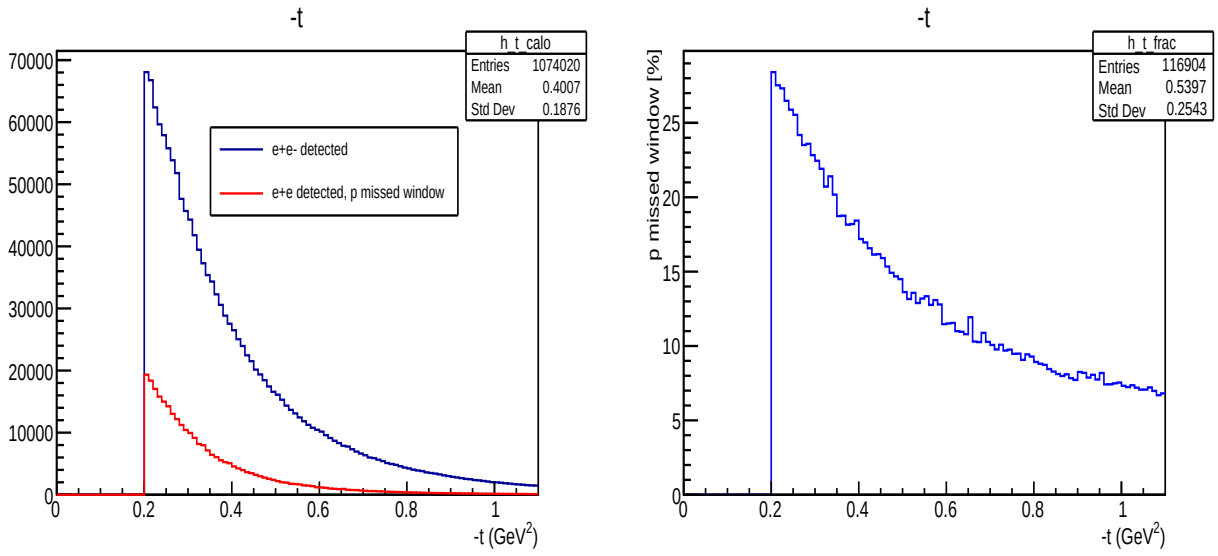


Figure 29: Left panel: the $-t$ distributions for events with the decay leptons within the detectors' acceptance (blue curve), and in addition the recoil proton in the acceptance (red curve). Right panel: the ratio of the two cases. The energy of bremsstrahlung photon beam is in the range from 5.5 GeV to 11 GeV. Kinematic cuts $4\ GeV^2/c^2 < Q'^2 < 9\ GeV^2/c^2$, $-t > 0.2\ GeV^2/c^2$, $-t/Q^2 < 0.3$ are applied.

# 4 Simulations and analysis

## 4.1 Event generator for the beam and target polarized TCS+BH reaction

We developed an event generator based on the formalism presented in 2.1. The generator webpage is hosted in [51], with a public version available. We generated events initiated from a real photon, the energy distribution being rescalled following a bremstrahlung spectra. At the generation level, we assume 100% polarization of the initial electron and 100% polarization of the target, which can be rescaled by measured values of dilution factors at the analysis level. We set the polarization of the target being along the x-axis, and we rotate randomly the reaction plane for taking into account the $\phi_S$ dependence of the reaction. The events are generated in the following kinematic range:

- 7.5 < $E_\gamma$<10.5 GeV,
- 4 < $Q'^2$ < 9 $GeV^2$,
- .04 < -t < 0.8 $GeV^2$,
- 40° < $\theta$ < 140°,
- 0° < $\phi$ < 360°,
- 0° < $\phi_S$ < 360°.

Fig. 30 shows the correlations between t, $Q'^2$ and $\xi$ for all generated events.

These simulations are used for all projection studies in the following. Events are weighted according to the unpolarized and polarized TCS+BH, BH "only" and TCS "only" cross sections for the purpose of systematic studies. TCS is calculated using GPDs H and $\tilde{H}$, using the same parametrization than other calculations in this document. Unpolarized, beam or target polarized TCS+BH cross sections are used for the projection of experimental uncertainties. We generated 200M events and obtained over $10^3$ generated events/bin for all projections, therefore we can neglect the uncertainties coming from the simulations in the following.

Some studies in the setup section are done with the genTCS [52] event generator, which uses bremsstrahlung photons from a 11 $GeV$ primary electron beam within the energy range 5.5 – 11 $GeV$, a point-like target, and with invariant masses of the lepton pairs in the resonance-free region between 2 and 3 GeV.

## 4.2 Angular correlations and interpretations

### 4.2.1 BH angular distributions

The angular dependence of the lepton pair production can be understood with the BH propagators of eq.6. In the lab frame or in the $\gamma N$ CM frame, if one of the leptons is emitted along the beam direction, one of the terms becomes very large. At these limits, one of the two BH diagrams

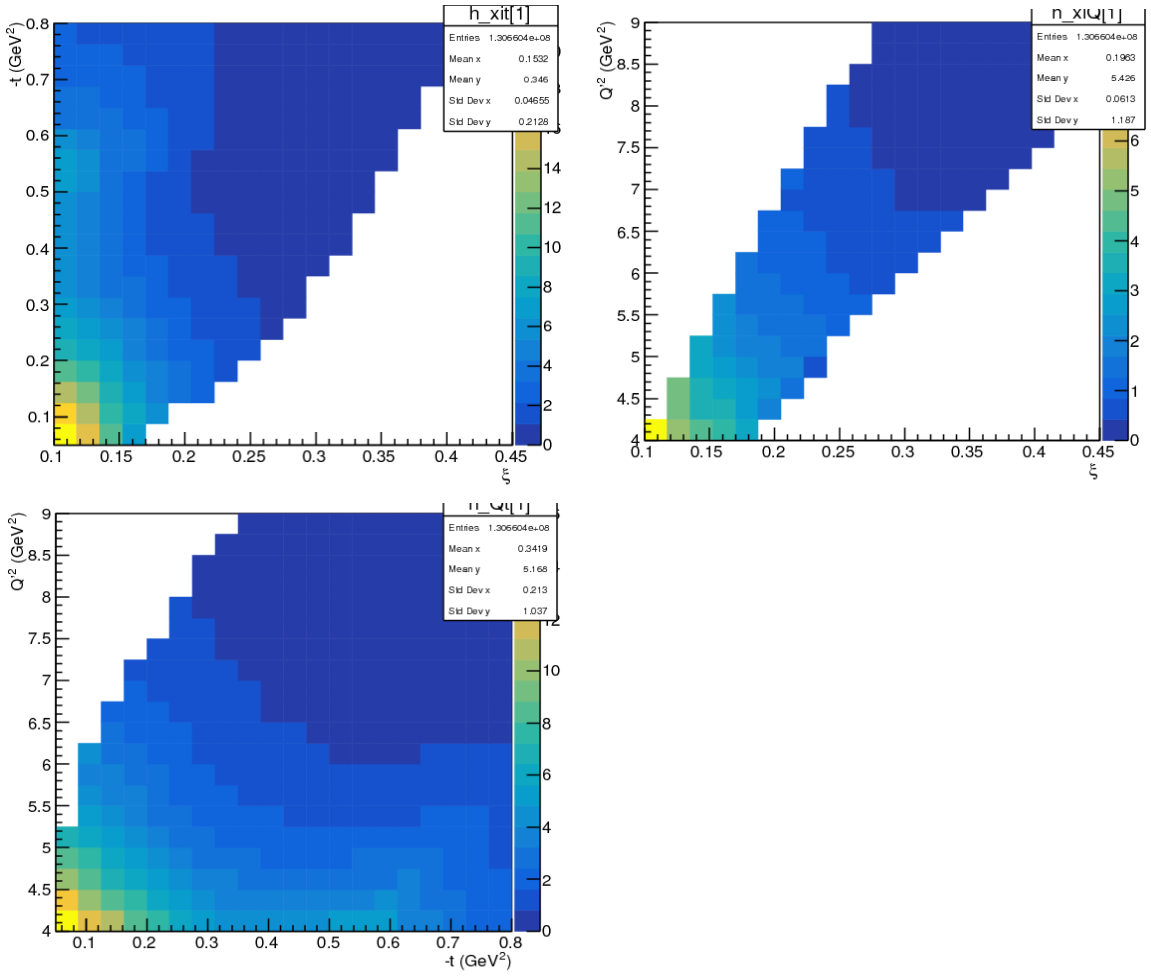


Figure 30: Top left: -t as a function of $\xi$, top right: $Q'^2$ as a function of $\xi$, bottom left: $Q'^2$ as a function of -t. The beam energy has been limited to 7.5 < $E_\gamma$<10.5 GeV. The weights are proportionnal to the unpolarized cross section.

is largely dominant compared to the other one. One of the leptons takes most of the energy of the virtual photon and is emitted at very low angle ($\sim 0°$), while the other one is emitted at large angle ($\sim 180°$) with a very low momentum. The cross section drastically increases next to these limits and sharp peaks are observed in angular distributions. Azimuthal distributions ($\phi$) are also strongly affected by this effect: one lepton going in the beam direction forces all particles to be emitted in the same plane (see Fig. 6). The impact of this correlation between $\theta$ and $\phi$ is illustrated in Fig. 31, presenting distributions in $\phi$, where $\theta$ has been integrated in asymmetric ranges over $\theta$ (one diagram dominates). At these kinematics, the BH peaks are at $\theta \sim 20°$ and $\theta \sim 160°$, explaining that the curve corresponding to $20° < \phi < 30°$ presents the largest cross section. In the perspective of experimental measurements, integrating calculations over a symmetric range around $\theta_{CM} = 90°$, away from BH peaks, presents the advantage of having the same contribution from the two diagrams in the integrated cross section while enhancing the statistic in each bin for displaying distributions in other variables in the data.

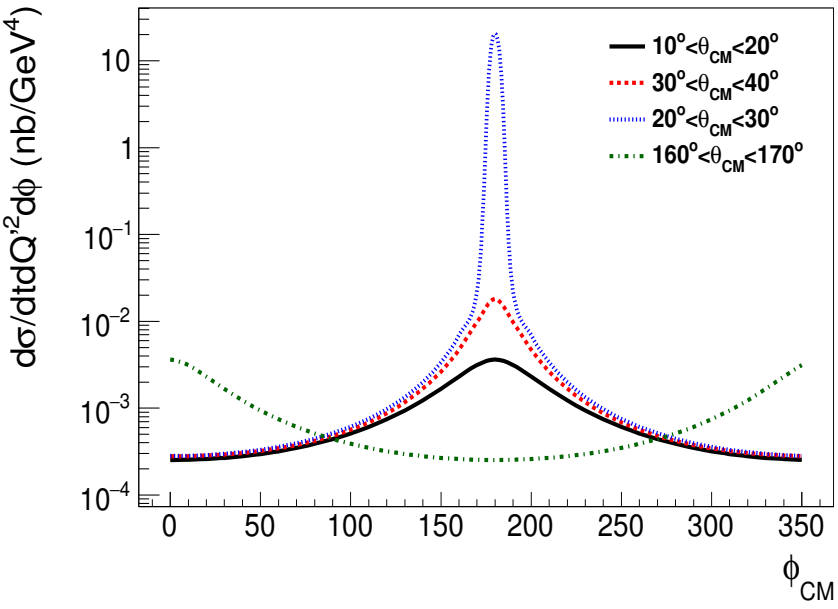


Figure 31: BH cross section as a function of $\phi$ at $Q'^2$ = 5 GeV$^2$, -t=0.3 GeV$^2$, E$_\gamma$=9.5 GeV, and integrated over $\theta_{CM}$ on various ranges (colored curves).

We expressed the cross sections as a function of the virtual photon CM frame electron angles $\phi$ and $\theta$ (eq. 2). The angle $\phi$ is conserved in the boost from $\gamma N$ C.M. frame to $\gamma^*$ rest frame, while $\theta$ is not conserved. It is correlated to $\theta_{lab}$ for a given $\Theta_{\gamma\gamma^*}$ angle (the angle between incoming and outgoing photon). At $\Theta_{\gamma\gamma^*}$ larger than zero, the position of the peaks in the $\theta_{CM}$ distribution therefore

depends on the kinematics ($E_\gamma$, t, $Q'^2$). The correlation between $\Theta_{\gamma\gamma^*}$ and t at fixed $E_\gamma$ and the $\Theta_{\gamma\gamma^*}$ dependence of the unpolarized cross section is displayed in Fig. 32. At small $\Theta_{\gamma\gamma^*}$ ($t_{min}$ limit), the peaks are observed for $\theta \to 0^\circ$ and $\theta \to 180^\circ$.

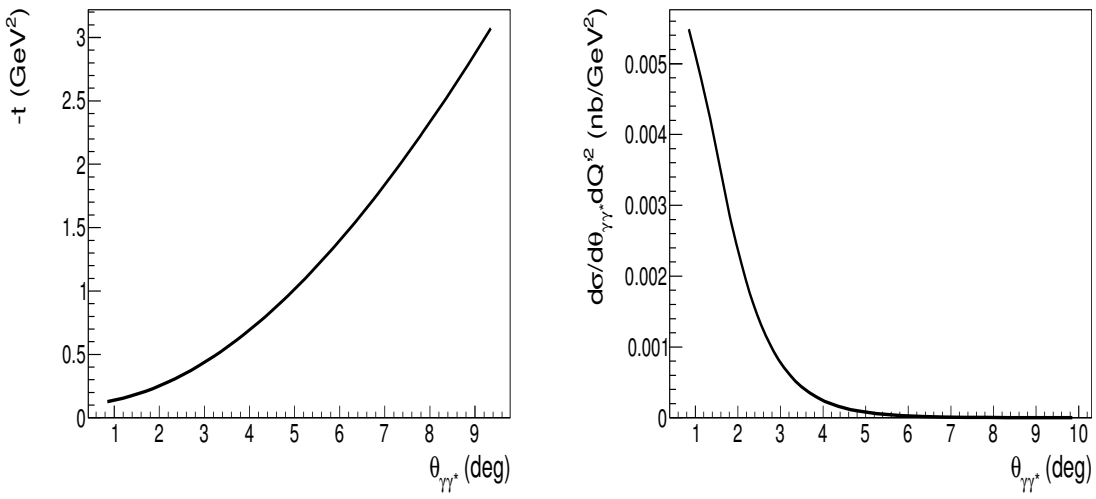


Figure 32: Distribution in -t versus $\theta_{\gamma\gamma^*}$ (left panel, at $Q'^2$=5 GeV$^2$) and BH cross section as a function of $\theta_{\gamma\gamma^*}$ (right panel, at -t=0.3 GeV$^2$ and $Q'^2$=5 GeV$^2$). Both curves are calculated at $E_\gamma$=9.5 GeV. for $0 < \phi_{CM} < 360^\circ$ and $45^\circ < \theta_{CM} < 135^\circ$.

#### 4.2.2 Solutions for the analysis

With limited data statistics and resolution effects, measuring TCS+BH in the BH peak regions would induce very large systematic uncertainties due to the very fast variations of the cross sections. To reproduce experimental conditions (limited statistics, broad kinematic range) and obtain numerically the position of the BH peaks, we computed BH cross sections as a function of $\theta$ for several fixed values of $E_\gamma$, t and $Q'^2$. We integrated the cross sections over $\phi$ with a limited number of steps (numerical integration in Gaussian quadrature starting from the lower edge of the bin). We perfomed calculations and compared the results for two values of $\theta$ symmetric around $\theta = 90^\circ$, with 5° steps: by instance we compare the results for 85° and 95°, for 80° and 100°, etc.. The results are the same for the 2 symmetric values in $\theta$ until approching the peaks. We defined values of $\theta_{min}$ and $\theta_{max}$, for which between these limits, the compared results have less than $5\%$ differences. We reproduced the same exercise for different values of $E_\gamma$, t and $Q'^2$. Values of $\theta_{max}$ for $E_\gamma = 9.5$ GeV, as a function of $-t$ and $Q'^2$ are displayed on Fig. 33. We reproduced the same exercise by integrating cross sections over different ranges in $\phi_{CM}$ (0$\pm$10°, $0 \pm 20^\circ$, $180^\circ \pm 30^\circ$, etc.). We con-

clude that the peaks can be avoided by 2-dimensional cuts in $\phi_{CM}$ and $\theta_{CM}$, which we appy in our projections, such as:

- if ($\theta_{CM}$<$\theta_{min}$ and $150° < \phi_{CM} < 210°$), the event has to be rejected,
- if ($\theta_{CM}$>$\theta_{max}$ and $-30° < \phi_{CM} < +30°$, the event has to be rejected,
- otherwise the event can be kept and results can be fitted with reasonable systematic errors.

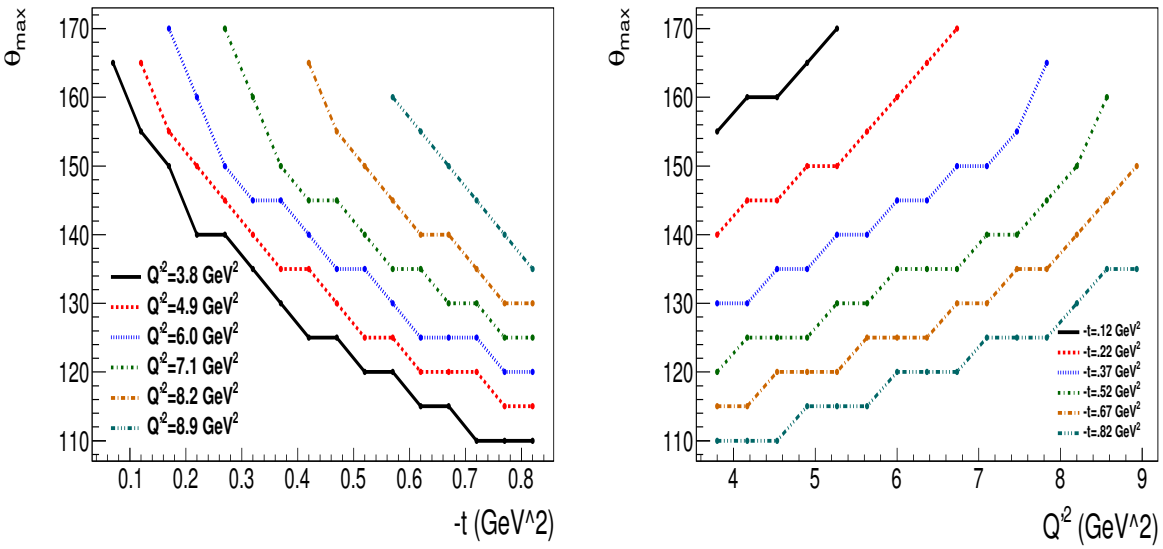


Figure 33: Values of $\theta_{max}$ for a fixed beam energy $E_\gamma = 9.5$ GeV, as a function of $t$ for different values of $Q'^2$ (left panel) and as a function of $Q'^2$ for different values of $-t$ (right panel). See text for details.

Further studies on angular correlations, impact on lepton kinematics and exclusivity can be found in [53].

### 4.3 Final particle distributions at vertex

As a consequence of the BH cross section behavior, it is not possible to determine the best position of the calorimeters and the recoil detector based solely on the expected counting rates. Indeed, the cross section can be very large for some specific angles and momentum of the final particles, but the asymmetry and the TCS/BH rate may be small. We studied the angular and momentum dependence of the unpolarized cross section, the TCS/BH rate and the size of the asymmetries. Fig. 34 compares the 2D distributions of the electron and the proton momentum polar angle in the

lab frame (without deflection) with different event weighting. We weighted the events by factors proportional to the unpolarized cross section (left column), to the TCS/BH rate (central column) and to the size of the transverse spin asymmetries (right column). The positions of the detectors in the setup we are proposing allow for a fair balance between counting rates and the size of the asymmetries, and allow for impact on extracting the CFFs, as shown in Sec. 2.4.

### 4.4 Dilution factors

The JLab electron beam polarization is assumed to be larger than 85%. In addition, we calculated the secondary bremsstrahlung photon transfer factor to be from 85% (7.5 GeV photons) to 100% (11 GeV photons) as shown in Fig. 35. On average, we estimate a photon beam polarization transfer factor of $\sim$75%.

From counting the number of polarized protons in the target material, we estimate the target polarization dilution factor to be $\sim$27% in the case of a detected recoil proton. The detection of the proton is improving the dilution factor by suppressing some of the high momentum protons in nitrogen.

The dilution factors are not included in the following section (projections, 4.6) and will be our main systematic uncertainty for the asymmetry measurements.

### 4.5 Systematic uncertainties and background contribution

In the SANE experiment [45], which used the UVA polarized target, the biggest contribution to systematic uncertainties came from target polarization (5%). The uncertainty is due to NMR measurement of the polarization. SANE experiment estimated a 2% uncertainty on the target dilution factor. In a similar way as was done for the SANE experiment, we will measure the packing fraction for each load of the target during the experiment.

Another source of systematic error can be $\pi^+\pi^-$ background. The pion suppression in the electromagnetic calorimeters is on the order of $10^3$ to $10^4$, typically. A study of $e^+e^-/\pi^+\pi^-$ ratios and pion discrimination for measurements of the $e^+e^-$ continuum is currently performed by the GlueX collaboration. This work is intended to study resonances such as J/$\Psi$ in the $\gamma P \to e^+e^-P'$ reaction, and includes studies of the continuum region for a lepton pair mass above 1.5 GeV. It estimates $\sim$30% contribution of $\pi^+\pi^-$ events at maximum using analysis cuts at $2\sigma$ of GlueX calorimeter resolution [54]. The rates strongly depend on the analysis cuts. These results have been obtained for a significantly lower luminosity, and for a different spectrometer acceptance. We will perform a detailed study with the real data from cross section measurements, and by means of simulations.

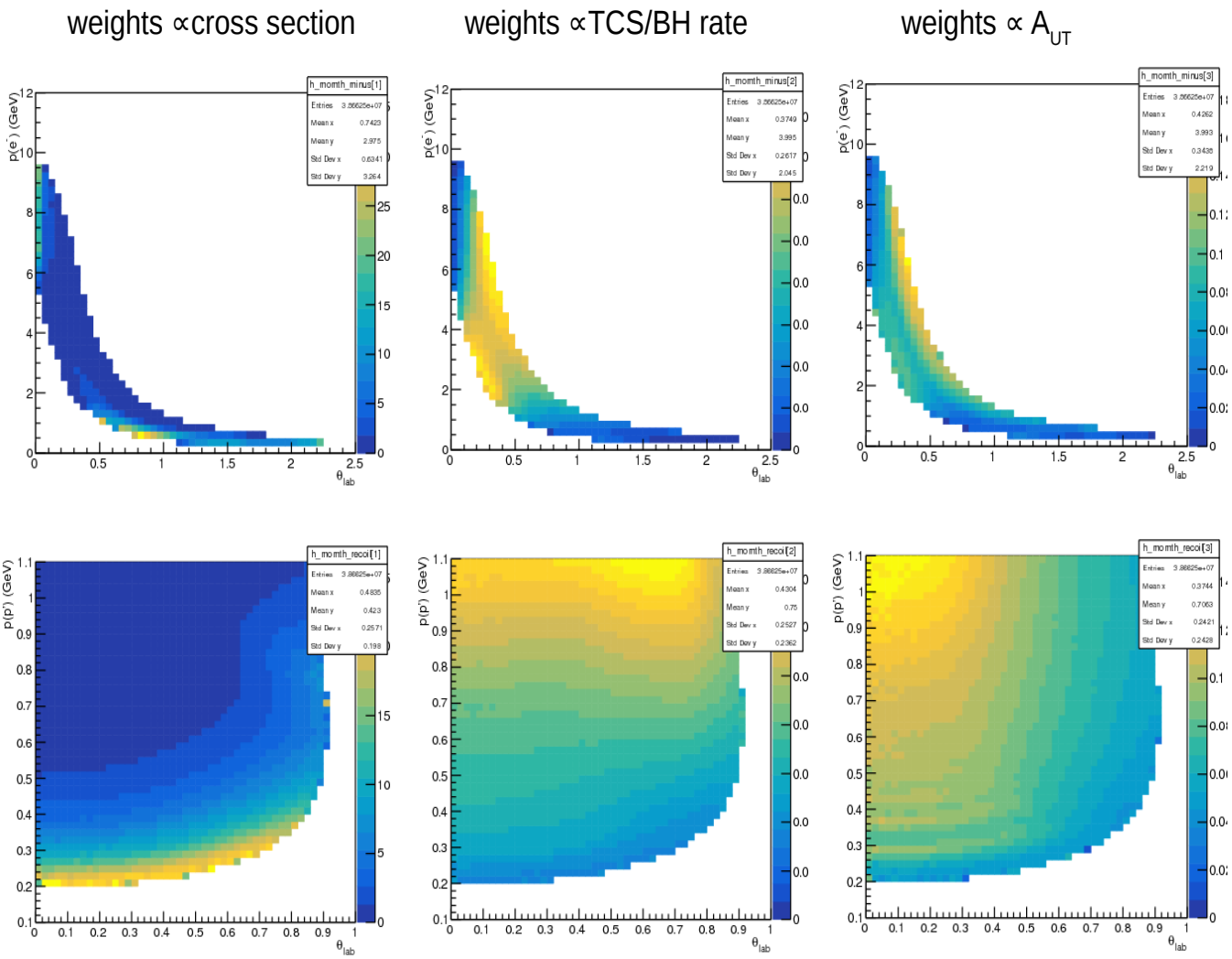


Figure 34: Distribution of momentum versus $\theta_{lab}$ for the scattered electron (top row) and the recoil proton (bottom row), weighted by factors proportionnal to the unpolarized cross section (left column), the TCS/BH rate (central column) and the size of the transverse target spin asymmetry (right column).

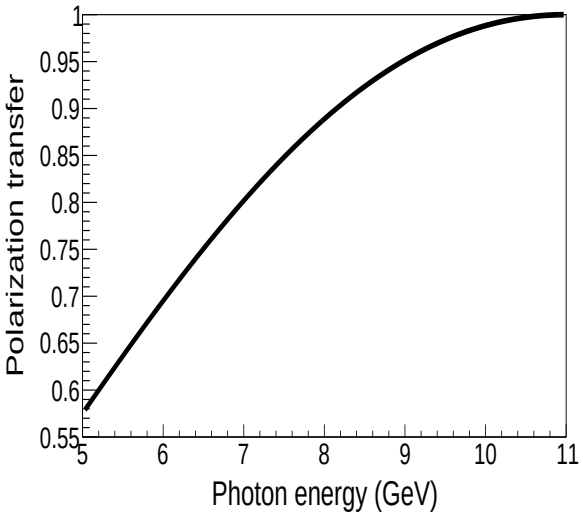


Figure 35: Circular polarization transfer for bremsstrahlung photons initiated from a 100% polarized 11 GeV electron.

We assume the triple coincidence accidental rates being suppressed by exclusivity cuts.

Proton resonances such as $\Delta$ will be suppressed by cuts of exclusive kinematics in the proton reconstruction with the recoil detector. A similar study using a recoil proton detector for COMPASS, at a similar kinematic, demonstrated negligible contribution (<1%) from such events. Such resonance suppression was achieved by applying exclusivity cuts to the recoil detector information, despite the resolutions on the proton momentum and energy were broad [55, 56].

A systematic associated with the beam polarization will enter into the beam spin asymmetry measurements, and can be assumed at a percent level.

Other backgrounds include gamma conversion and $\pi^0$ events, which can be estimated from simulations.

### 4.6 Experimental projections

We applied the following phase space and analysis cuts on our simulations:

- 7.5 < $E_\gamma$ < 11 GeV (from correlations, we obtain .1 < $\xi$ < .45),
- 4 < $Q'^2$ < 9 $GeV^2$,
- 0.04 < -t < 1.04,
- 40° < $\theta$ < 140° in addition to the cut $\theta_{min,max}$ as explicited in section 4.2.2,

- $0° < \phi < 360°$,
- $0° < \phi_S < 360°$,
- p(p) > 0.1 GeV,
- E( $e^+$ or $e^-$) > 0.7 GeV,
- (E($e^+$) + E($e^-$)) > 5 GeV,
- tagging of the 2 leptons and the proton,
- acceptance cut at the calorimeters level: $\pm 4$ cm vertical band from the middle.

We defined bins in -t, $\xi$ and $Q'^2$ as presented in Fig. 36 for the unpolarized and beam polarized cross sections. A total of 8 kinematic bins is defined. For each of these bins, we use 16 bins in $\phi$, with additional 16 bin in $\phi_S$ for transversely target polarized dependent cross sections. We integrated over $\theta$.

We optimized the binning in $\xi$ and -t which is important for CFFs extraction by balancing statistics and narrow widths. For the first -t bin (-t<0.2 GeV$^2$), we have 2 bins in $\xi$: 0.1<$\xi$<0.15 and 0.15<$\xi$<0.22. For the second and third -t bins (0.2<-t<0.35 GeV$^2$ and 0.35<-t<0.7 GeV$^2$), we have 3 bins in $\xi$: 0.1<$\xi$<0.15, 0.15<$\xi$<0.22 and 0.22<$\xi$<0.3. Despite the proton detection is limited for -t<0.2 GeV$^2$ due to the magnetic field, we display this region in our projections. We base our observations and interpretations on the 2 largest -t bins.

We have cut the central $\pm 4$ cm vertical band in the middle of the calorimeters in order to avoid the high background rates in this region. The impact on counting rates is an overall reduction of $\sim$15%. The asymmetries are not significantly affected by this cut nor the physics impact of the measurements.

We applied a photon energy cut such as 7.5<E$_\gamma$<11 GeV in following projections. The phase-space after the $\theta_{min,max}$ cut is narrow below these energies, however events from lower energy photons will be measured.

We display in Fig. 37 a projection of the counting rates for the unpolarized cross section, after applying all cuts and acceptance. The shape of the curves in the lowest -t bin is explained by the phase space cut in ($\theta$, $\phi$), affecting the peaks at $\phi = 0$ and $\phi = \pi$. We display in Fig. 38 the beam spin asymmetries with the expected statistic uncertainties. Fig. 39 presents the $A_{Ux}$ and $A_{Uy}$ asymmetries using the same binning For a selected kinematic, we display in Fig. 40 the transverse target spin asymmetries as a function of $\phi$ in $\phi_S$ bins. Additional projections can be found in Appendix B. Each set of 2 orthogonal transverse spin asymmetry (first row versus second row, same column) provides independent information and will be fitted simultaneously to extract the CFFs.

By combining the uncertainties, it leads to reasonable errors on the CFFs. We notice that the size of 2 orthogonal asymmetries is strongly correlated: for instance, the larger $A_{UX}$ is, the smaller $A_{UY}$. Therefore, small asymmetries in one $\phi_S$ bin is not reflecting a lack of sensitivity to CFFs when combining all $\phi_S$ bins. This effect is also visible in the figure of merits (next section, 4.7). It is enhanced at low $\xi$.

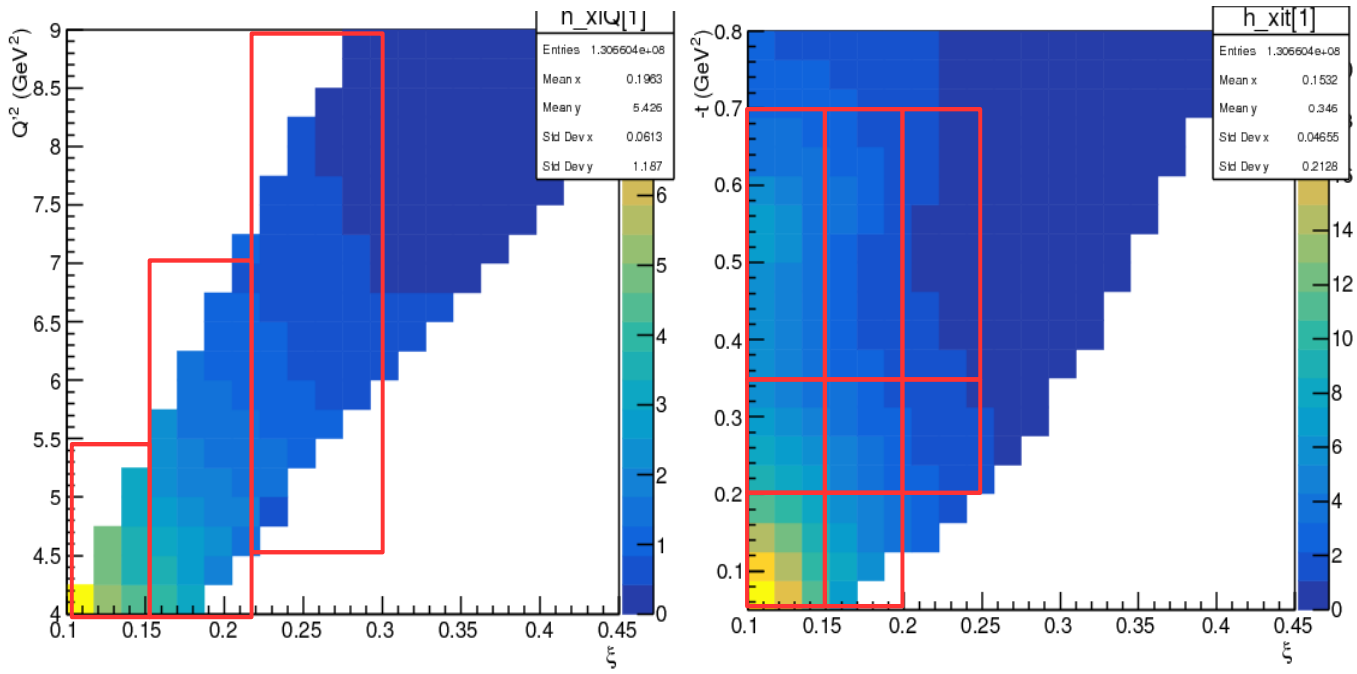


3 bins in ξ and Q'²

1) 0.1 < ξ < 0.15, 4 < Q'² < 5.5 GeV²

2) 0.15 < ξ < 0.22, 4 < Q'² < 7 GeV²

3) 0.22 < ξ < 0.3, 4.5 < Q'² < 9 GeV²

3 bins in -t

1) 0.04 < -t < 0.2 GeV²

2) 0.2 < -t < 0.35 GeV²

3) 0.35 < -t < 0.7 GeV²

Total: 8 bins in ξ, t, Q'²

Figure 36: Phase space binning for the TCS+BH analysis in $\xi$ and $Q'^2$ (left) and in $\xi$ and -t (right). A total of 8 kinematic bins is used for the analysis.

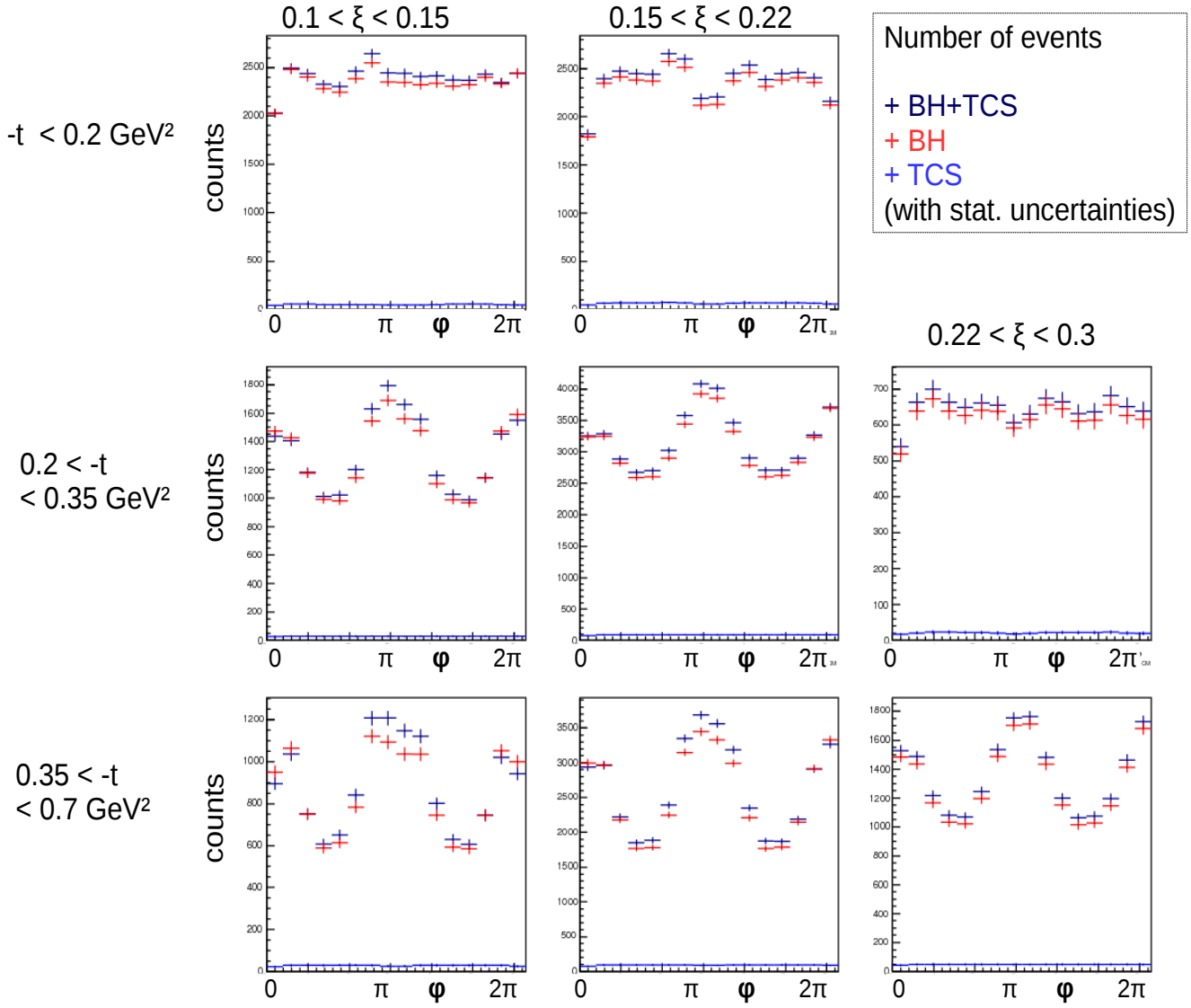


Figure 37: Projection of number of events in each bin for 16 bins in $\phi$. Calculated from unpolarized cross sections corrected by the acceptance, after applying all cuts. Events are weighted by BH "only" rates (red), BH+TCS rates (dark blue) and TCS "only" rates (light blue, very low rates). The different panels correspond to various kinematic bins, indicated in the figures. The counts and the statistic uncertainties are represented and correspond to an integrated photon luminosity of $5.85 * 10e5$ pb$^{-1}$ for $5.5 < E_\gamma < 11$ GeV. The projections include acceptance, phase-space cuts, momentum thresholds and a $E_\gamma > 7.5$ GeV cut. Our interpretations are based on projections for $-t > 0.2$ GeV$^2$ only ($2^d$ and $3^d$ rows) due to magnetic field effects and the limited acceptance at smaller -t. The stronger effect of the phase-space cuts for $-t < 0.2$ GeV$^2$ is the reason for the $\phi$ distribution shapes being different than for the other bins.

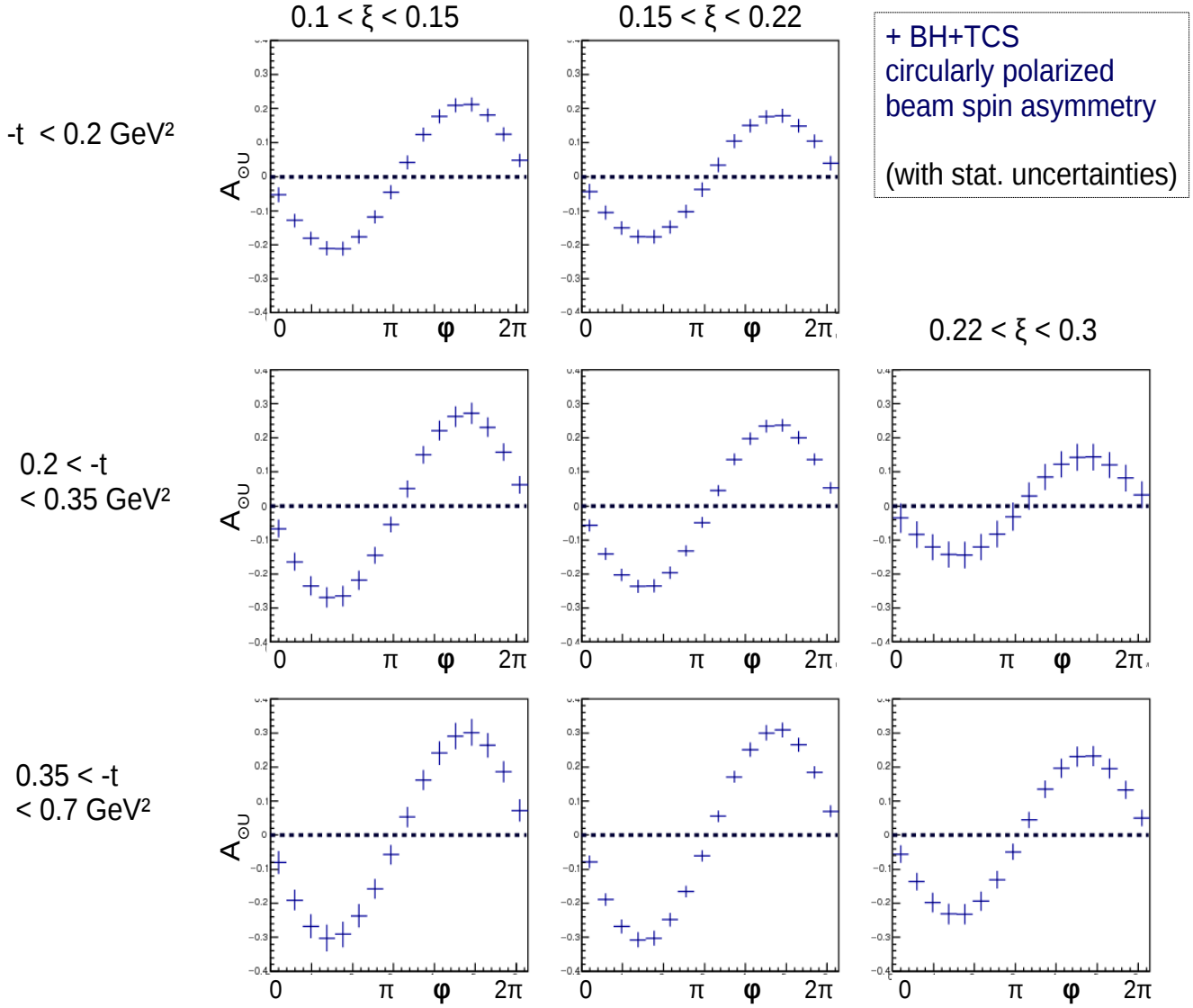


Figure 38: Projection of the single circularly polarized beam spin asymmetries in each bin as a function of 16 bins in $\phi$. The different panels correspond to various kinematic bins, indicated in the figures. Statistic uncertainties are represented and correspond to an integrated photon luminosity of $5.85 * 10e5$ pb$^{-1}$ for $5.5 < E_\gamma < 11$ GeV. The projections include acceptance, phase-space cuts, momentum thresholds and a $E_\gamma > 7.5$ GeV cut. The ~75% beam polarization transfer factor (in average) is not included. Our interpretations are based on projections for $-t > 0.2$ GeV$^2$ only ($2^d$ and $3^d$ rows) due to magnetic field effects and the limited acceptance at smaller -t.

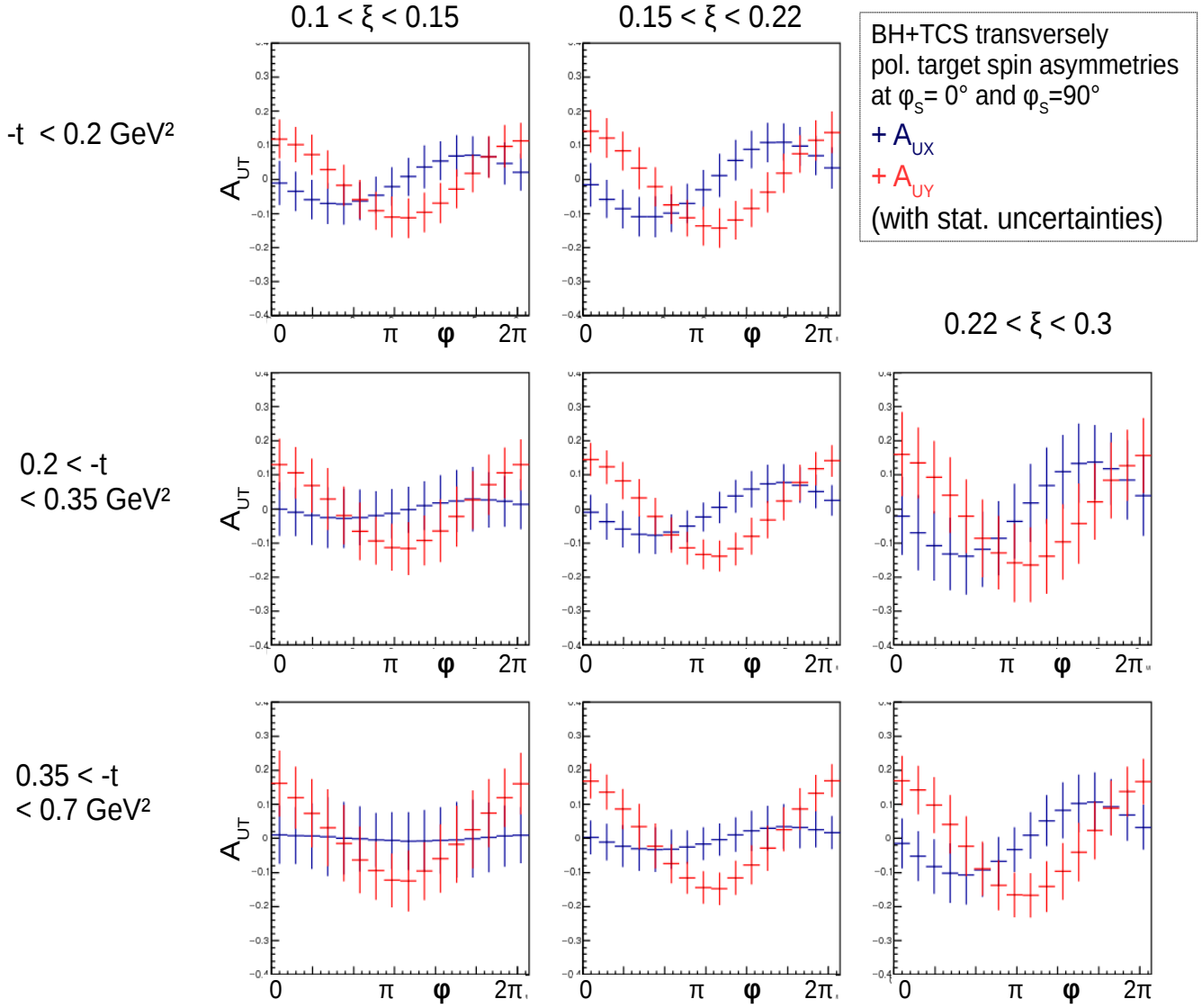


Figure 39: Projection of the single transversely polarized target spin asymmetries for $\phi_S = 0°$ (blue) and $\phi_S = 90°$ (red), as a function of 16 bins in $\phi$. Statistic uncertainties are represented and correspond to an integrated photon luminosity of $5.85 * 10e5$ pb$^{-1}$ for $5.5 < E_\gamma < 11$ GeV. The projections include acceptance, phase-space cuts, momentum thresholds and a $E_\gamma > 7.5$ GeV cut (see section 4.6). Systematic uncertainties and the 27% target polarization dilution factor are not included. Our interpretations are based on projections for $-t > 0.2$ GeV$^2$ only ($2^d$ and $3^d$ rows) due to magnetic field effects and the limited acceptance at smaller -t.

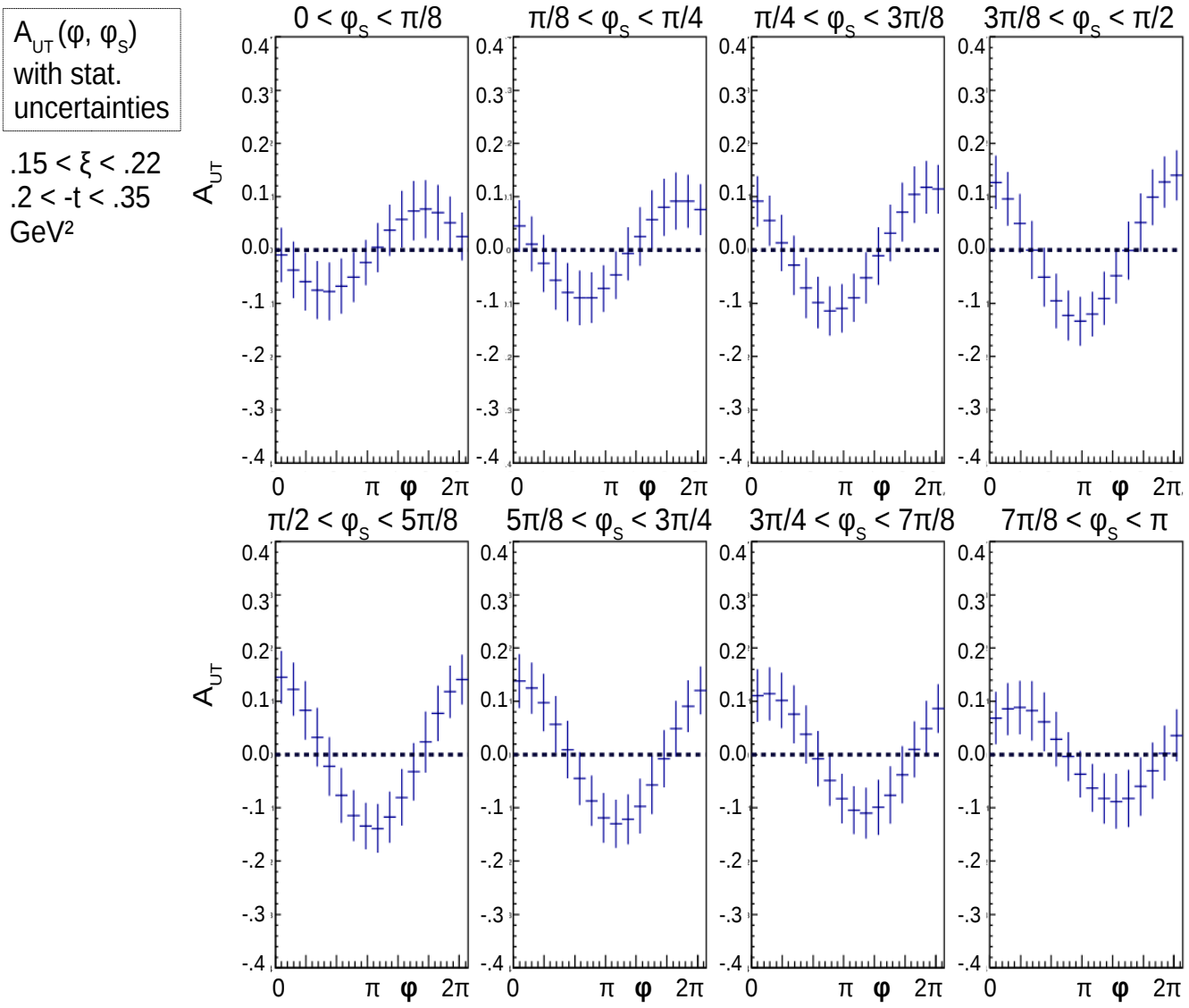


Figure 40: Projection of the single transversely polarized target spin asymmetries in bins of $\phi_S$ (different panels), as a function of 16 bins in $\phi$ and for $0.15 < \xi < 0.22$ and $0.2 < -t < 0.35$ GeV$^2$. Statistic uncertainties are represented and correspond to an integrated photon luminosity of $5.85 * 10e5$ pb$^{-1}$ for $5.5 < E_\gamma < 11$ GeV. The projections include acceptance, phase-space cuts, momentum thresholds and a $E_\gamma > 7.5$ GeV cut. Systematic uncertainties and the 27% target polarization dilution factor are not included. Our interpretations are based on projections for $-t > 0.2$ GeV$^2$ only ($2^d$ and $3^d$ rows) due to magnetic field effects and the limited acceptance at smaller -t.

### 4.7 Figures of merit

We defined the figures of merit for the asymmetries as

$$F.O.M. = N * A^2, \tag{14}$$

where N is the number of events including the acceptance and analysis cuts, and $A^2$ the size of the asymmetry. We neglect the background contribution and polarization transfer factor in this definition. We display Fig. 41 the F.O.M. for the beam spin asymmetries. The binning for the F.O.M. is defined in the same way as for Fig. 38. The target spin asymmetries F.O.M. are displayed Fig. 42 for one reference kinematical bin. The binning for this figure is defined in the same way as for Fig. 40. The figures for other kinematical bins are presented in appendix B.

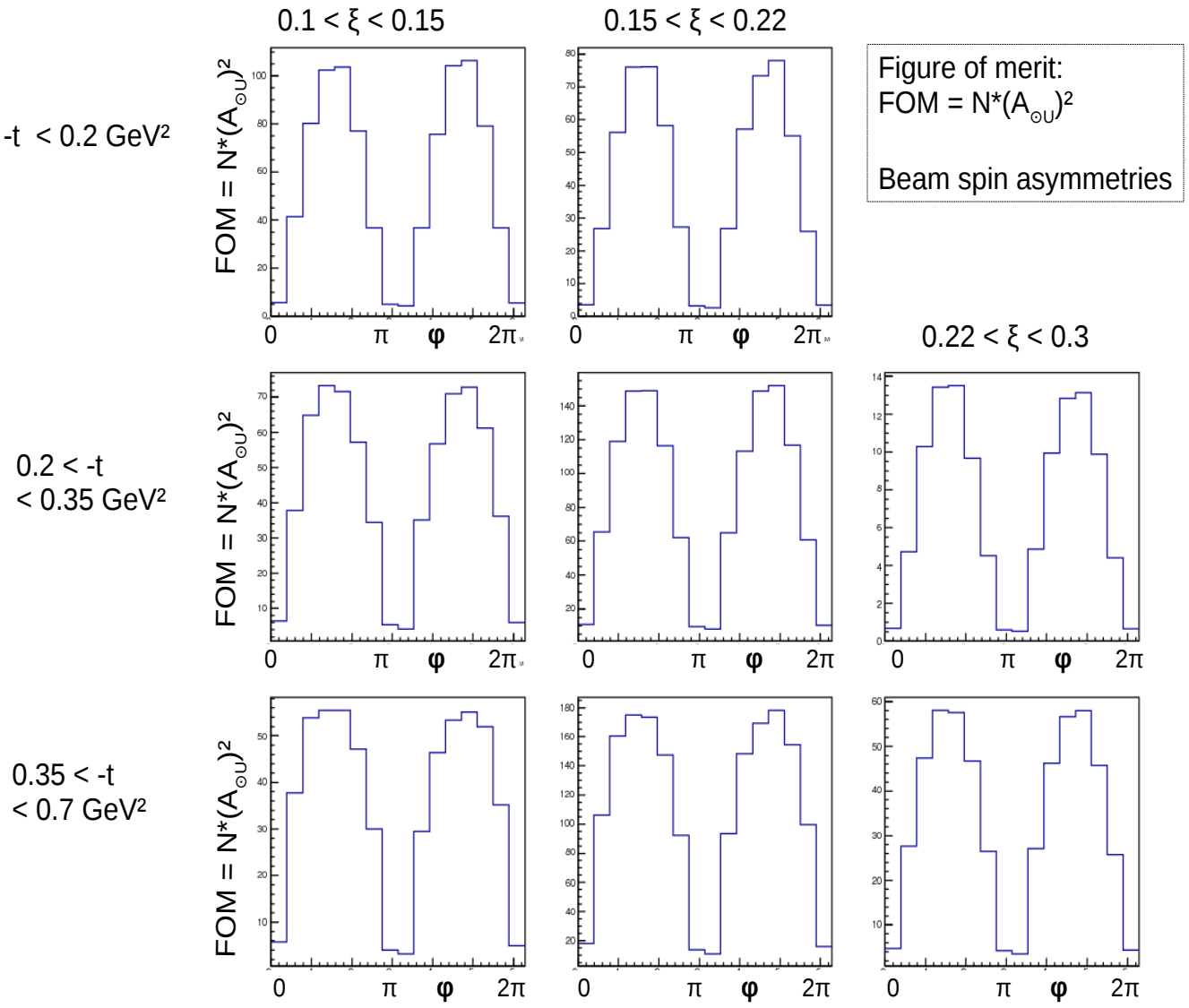


Figure 41: Figures of merit for the single circularly polarized beam spin asymmetries in each bin as a function of 16 bins in $\phi$. The different panels correspond to various kinematic bins, indicated in the figures. These results correspond to an integrated luminosity of $5.85 * 10e5$ pb$^{-1}$.

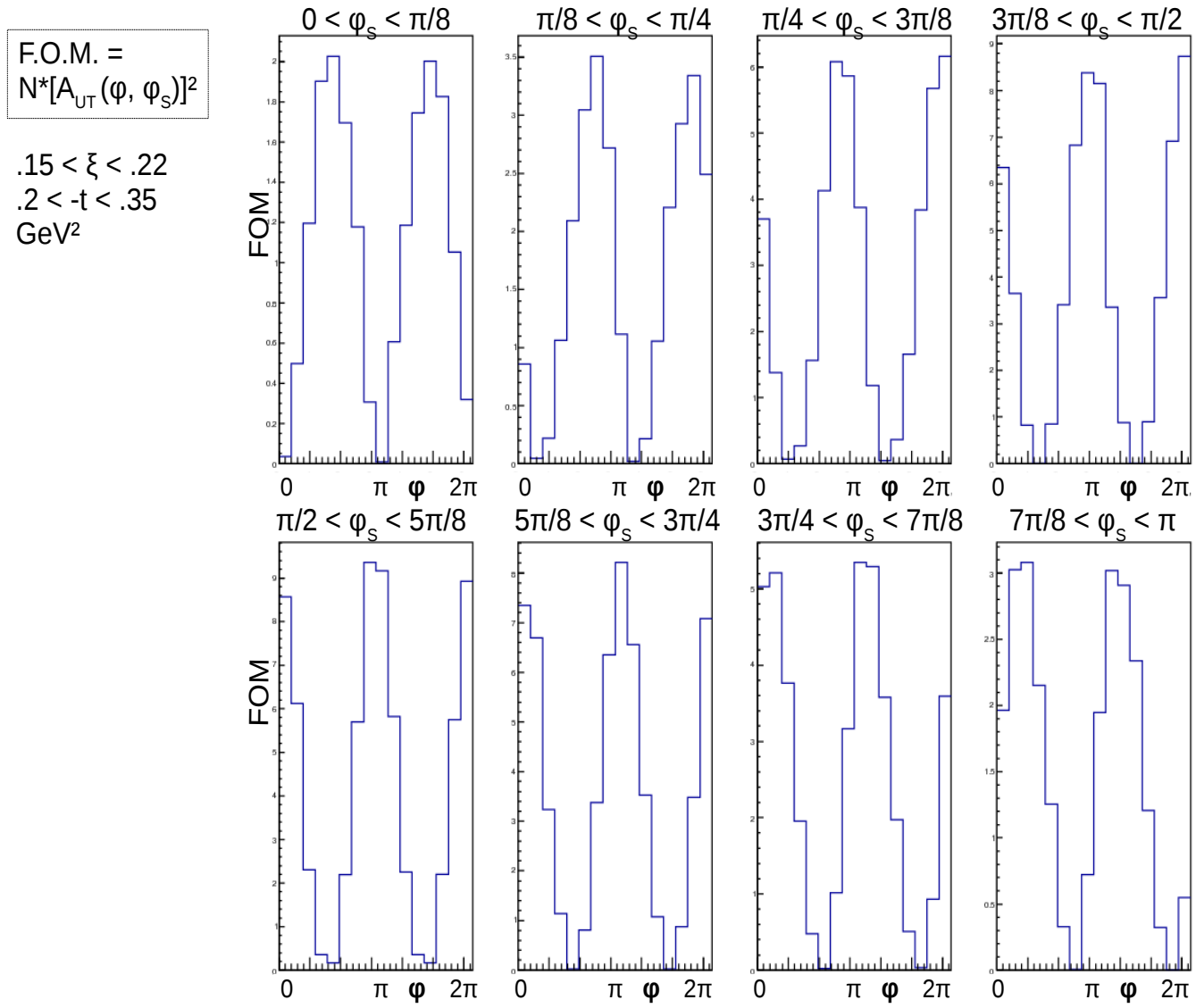


Figure 42: Figures of merit for the single transversely polarized target spin asymmetries in bins of $\phi_S$ (different panels), as a function of 16 bins in $\phi$ and for $0.15 < \xi < 0.22$ and $0.2 < -t < 0.35$ GeV$^2$. These results correspond to an integrated luminosity of $5.85 * 10e5$ pb$^{-1}$.

# 5 Beam time request

We request a total of 52 days, of which 16 calendar days for activities without beam, and 35 PAC days for commissioning and physics data taking. Our request is based on the following needs:

- Setup and installation in Hall C: 5 calendar days,
- Initial signal and electronics checkout (without the beam): 5 calendar days,
- Gain matching of the detectors' channels (with gain monitoring system): 1 calendar day,
- Commissioning with the beam: 5 PAC days,
- Physics measurement: 30 PAC days,
  with an 11 GeV, 2.5 $\mu$A electron beam and the UVa/JLab $NH_3$ polarized target. We request a longitudinally polarized electron beam of polarization > 85%.
- Target and experiment apparatus configuration change:
  - target annealing: 1 calendar day,
  - recovering PbWO crystals: 1 calendar day.
- Decommissioning: 3 calendar days.

# 6 Conclusion

We presented our project aiming at the measurement of the TCS+BH reaction. We will measure the unpolarized cross section, cross section of circularly polarized photon beam, and cross section of transversely polarized proton. This measurement will be held at the Jefferson Laboratory Hall C experimental facility, using a real photon source (Compact Photon Source, CPS), electromagnetic calorimeters as for the Neutral Particle Spectrometer (NPS), recoil proton detectors, and using a transversely polarized target ($NH_3$ UVa/JLab target). The main physics goals of this experiment are:

- Extraction of the CFF $\Im E$ of the proton at the same level as achievable from DVCS experiments. This result will allow constrain the quark angular momenta and contribute to the understanding of the nucleon's partonic spin structure.
- Study of GPD universality and higher twist effects thanks to a unique comparison of results from a spacelike process (DVCS, in other experiments) and a timelike process (TCS, this experiment). The expected level of precision on extracted CFFs compared to other approved TCS experiments [2, 1] is one order of magnitude better on GPD H.
- Complementarity with DVCS measurements and the possibility of combined CFF extraction from TCS and DVCS observables simultaneously. TCS observables bring new independent information, allowing for an extraction of all the proton quark CFFs at the same time, and for constraining GPD models.

We will take advantage of the development of the approved NPS project [15]. The main hardware development that are required are:

- A second electromagnetic calorimeter similar to the NPS one,
- A scintillator hodoscope based recoil proton detector.

We anticipate a need of 30 days of beam for the physics data taking (see section 5), with a photon luminosity of $10^{35}$ photons/cm$^2$/s, which corresponds to $5.85 * 10^5$ pb$^{-1}$ integrated luminosity for 5.5 to 11 GeV real photons.

# A Details about CFF fitting method

All the distributions we generated and used for extracting the CFFs are shown on Fig. 43 (DVCS+BH) and 44 (TCS+BH). Rather than directly fitting the CFF, we extract coefficients of the generated CFFs values from these observables. The coefficients are set to 1 when the generated value is recovered. We limit the variation of all the coefficients during the minimization procedure to stay in a range of $[-5, +5]$, in order to force underconstrained fits to converge. The impact of limitating the variation of the coefficients on uncertainties and on correlation between the extracted CFFs is discussed in [57]. As shown on Fig. 45, the result of the fit (mean value) has a dependence on the starting point and fluctuates around the generated value. However, the $\pm 1\sigma$ limits of the result are stable. To check if CFFs can be extracted from actual data, we also smear the generated cross section points within $1\sigma$ of the uncertainties. Similarly, we started the fits from random values of the coefficients. We obtained broader distributions of the results and their limits, with a resolution including the uncertainties on the observables and the correlation between the different CFFs (Fig. 46).

We fitted the results of the fits (CFF value and $1\sigma$ errors) by Gaussian functions. When a given CFF can be extracted from a specific set of observables, we found stable results and allocated the fitted $1\sigma$ limits as uncertainties on extracted CFFs. To avoid overcounting the uncertainties on CFFs and in our goal of comparating DVCS and TCS, we used the unsmeared distributions of pseudo-data for this exercise.

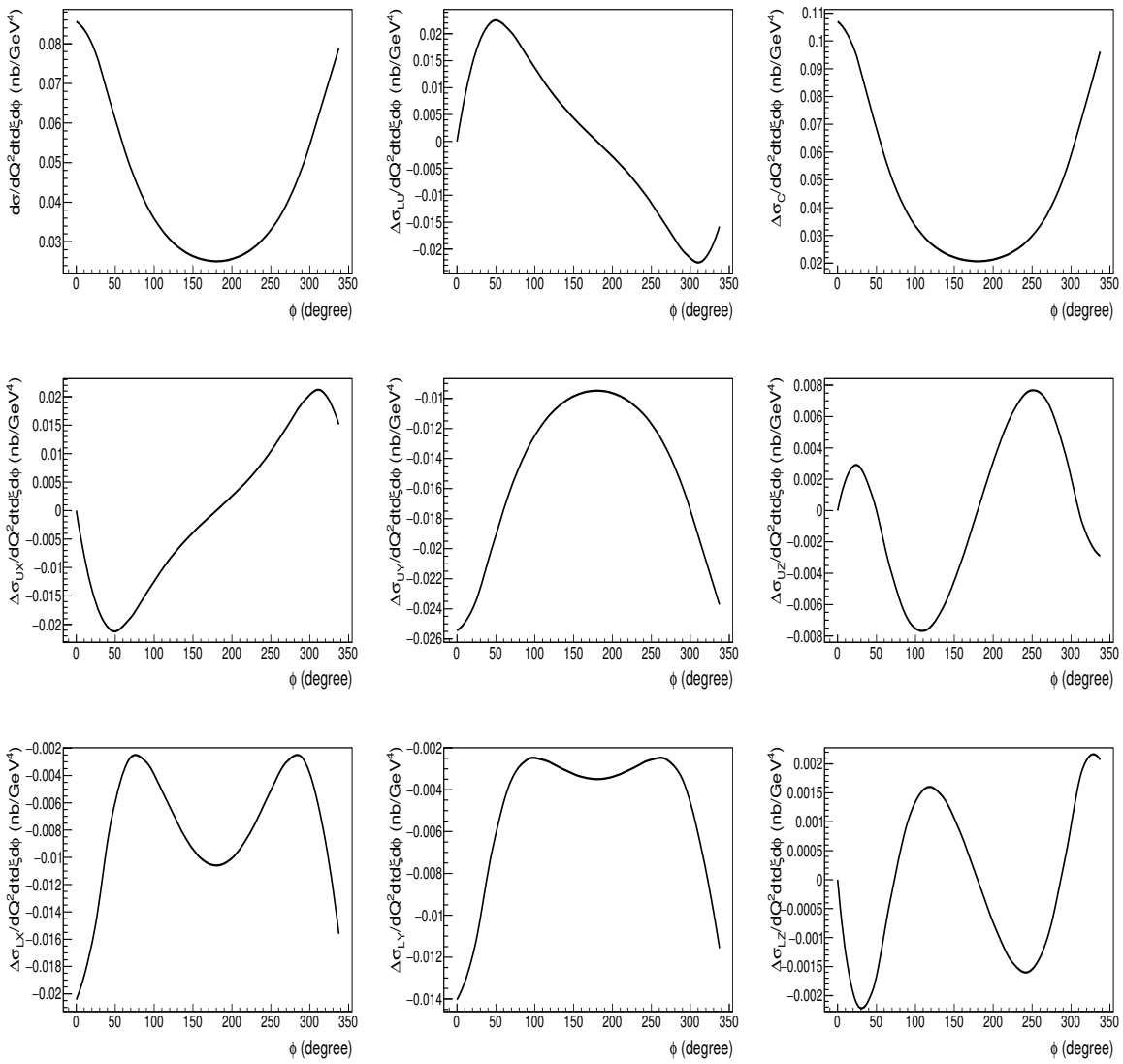


Figure 43: Generated distributions for DVCS+BH process. First row: unpolarized cross section, beam spin cross section difference, beam charge cross section difference. Second row: single target spin cross section differences (target spin along x, y, z). Third row: double spin cross section differences (target spin along x, y, z).

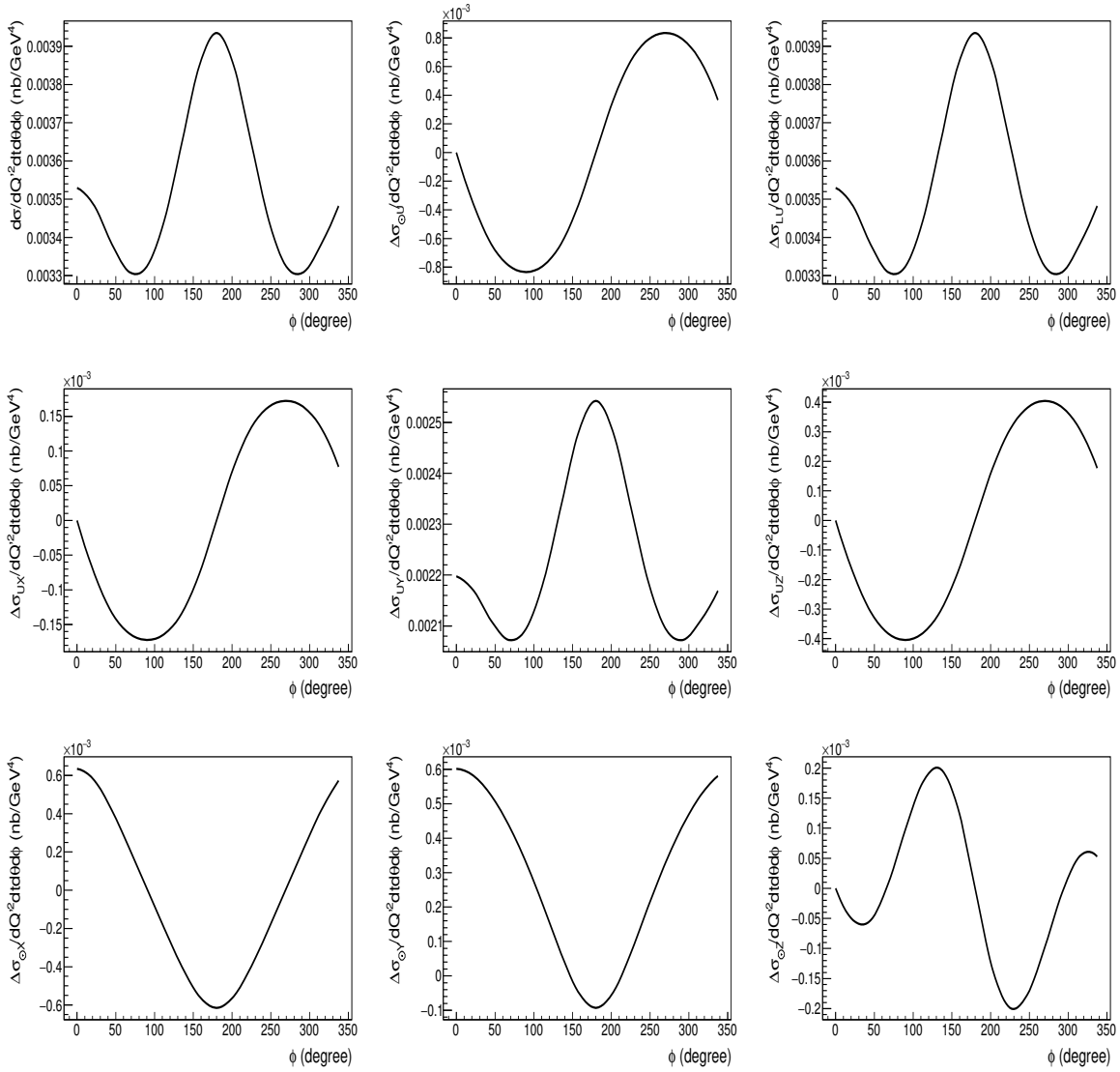


Figure 44: Generated distributions for TCS+BH process. First row: unpolarized cross section, circularly polarized beam spin cross section difference, longitudinaly polarized beam cross section difference. Second row: target polarized cross section differences (target spin along x, y, z). Third row: double beam and target polarized cross section difference (target spin along x, y, z).

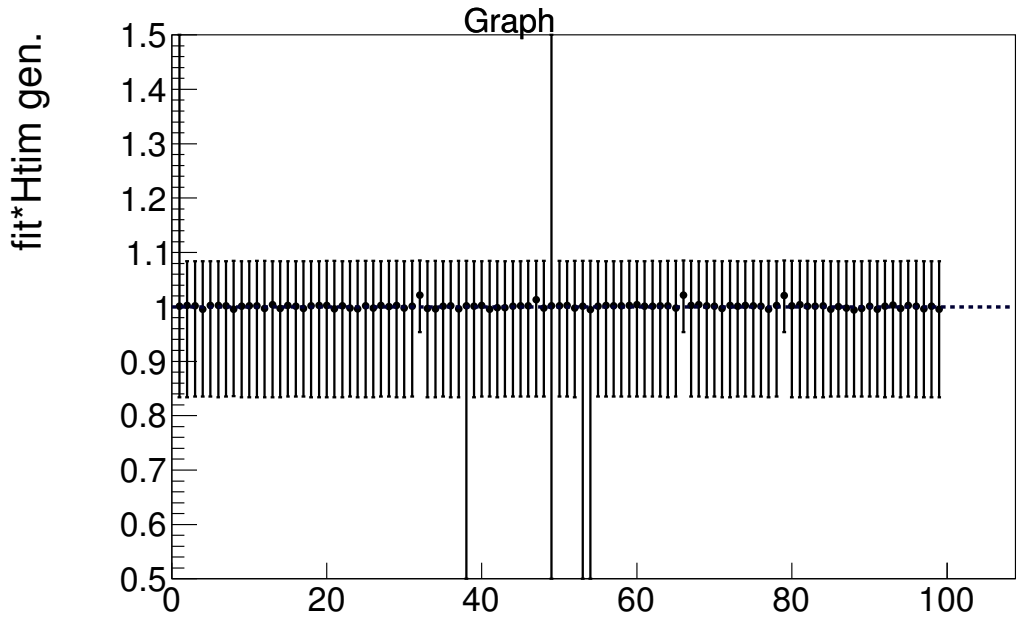


Figure 45: Result for $\Im\tilde{\mathcal{H}}$ of fitting 100 times the same distribution starting from a random value for all CFF coefficients in $[-5, +5]$. We fitted simultaneously DVCS+BH unpolarized cross section, beam spin and longitudinal target single and double polarized cross section differences. We assumed uncertainties of 5%/bin and 7%/bin for the unpolarized and polarized cross sections, respectively, for 16 bins in $\phi$.

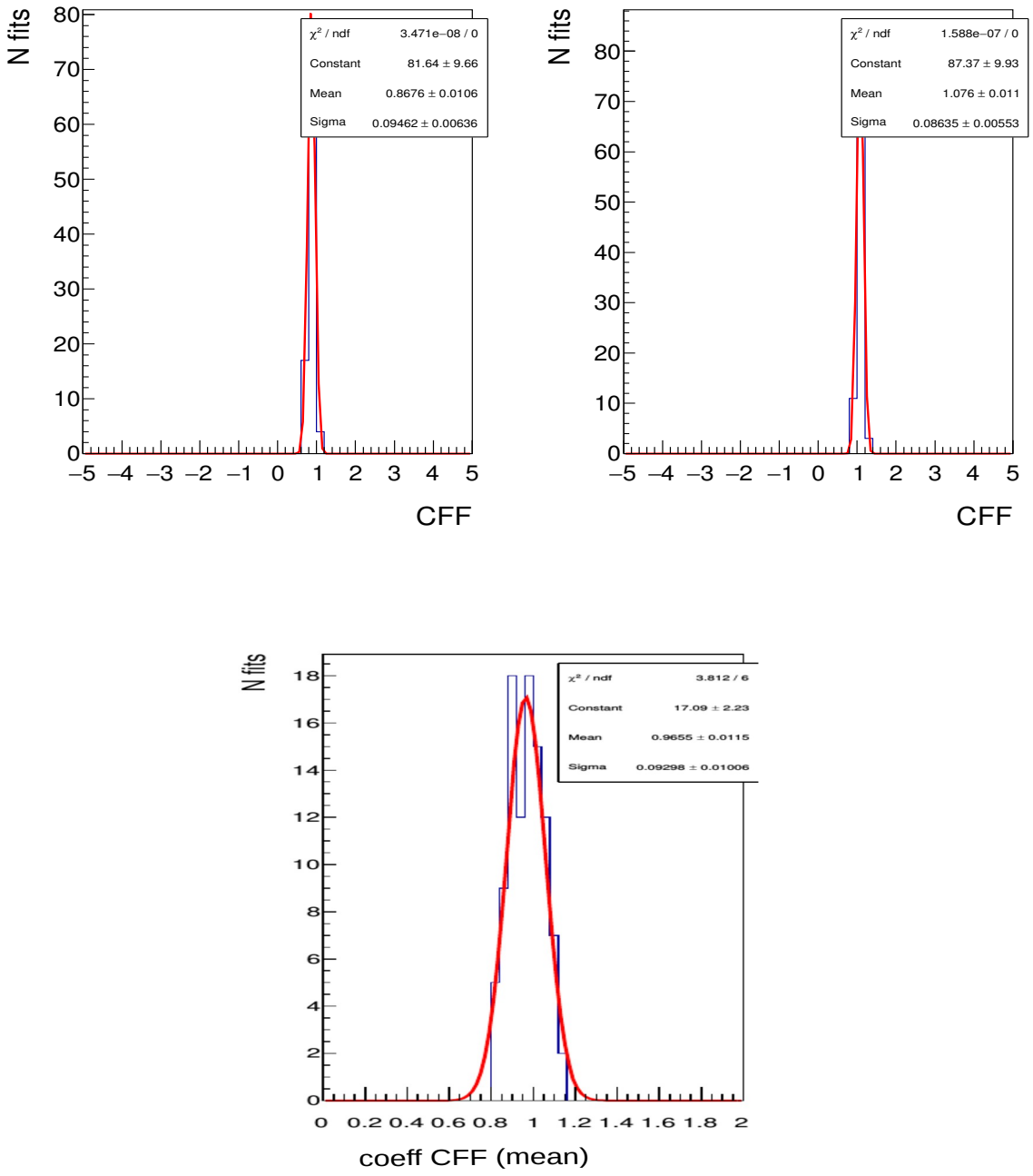


Figure 46: Top: Minimal (left) and maximal (right) limits of $\Im\tilde{\mathcal{H}}$ extracted from fitting 100 times smeared distributions of the same observables, and starting from a random value for all CFF coefficients in $[-5, +5]$. Bottom: fit result (central value) for the same distributions. We fitted simultaneously DVCS+BH unpolarized cross section, beam spin and longidutinal target single and double polarized cross section differences. We assumed uncertainties of 5%/bin and 7%/bin for the unpolarized and polarized cross sections, respectively, for 16 bins in $\phi$.

# B Additional experimental projections

## B.1 Projections: transverse target spin asymmetries in kinematic bins

Fig. 47 to 54 present the transverse target spin asymmetries as a function of $\phi$ and $\phi_S$ for different kinematic bins. For all these figures, we took account the acceptance of the setup (section 3.7. We applied the analysis, acceptance and phase-space cuts as described in section 4.6. For each figure sub-panel, the statistic uncertainties are represented and correspond to an integrated luminosity of $5.85 * 10e5$ pb$^{-1}$ for photons such as $5.5 < E_\gamma < 11$ GeV. Our observations and interpretations are based on the results for $-t > 0.2$ GeV$^2$ only, as for lower -t we may be biased by the magnetic field effects and smaller acceptance.

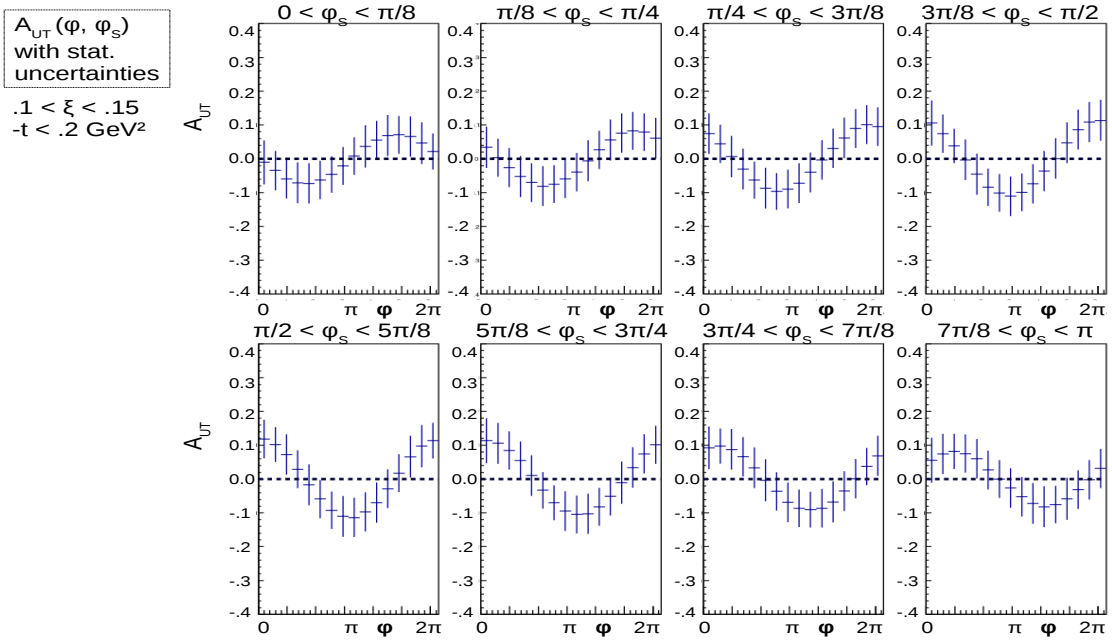


Figure 47: Projection of the single transversely polarized target spin asymmetries in bins of $\phi_S$ (panels), as a function of 16 bins in $\phi$ and for $0.1 < \xi < 0.15$ and $0.04 < -t < 0.2$ GeV$^2$. Statistic uncertainties are represented. Systematic uncertainties and the 27% target polarization dilution factor are not included.

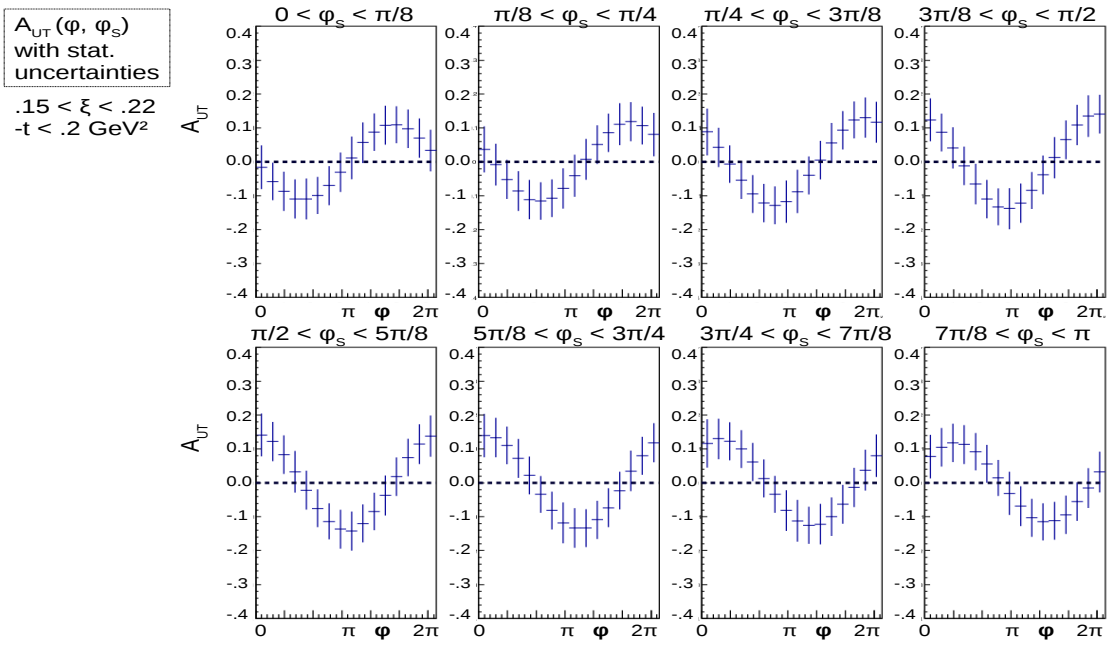


Figure 48: Projection of the single transversely polarized target spin asymmetries in bins of $\phi_S$ (panels), as a function of 16 bins in $\phi$ and for $0.15 < \xi < 0.22$ and $0.04 < -t < 0.2$ GeV$^2$. Statistic uncertainties are represented. Systematic uncertainties and the 27% target polarization dilution factor are not included.

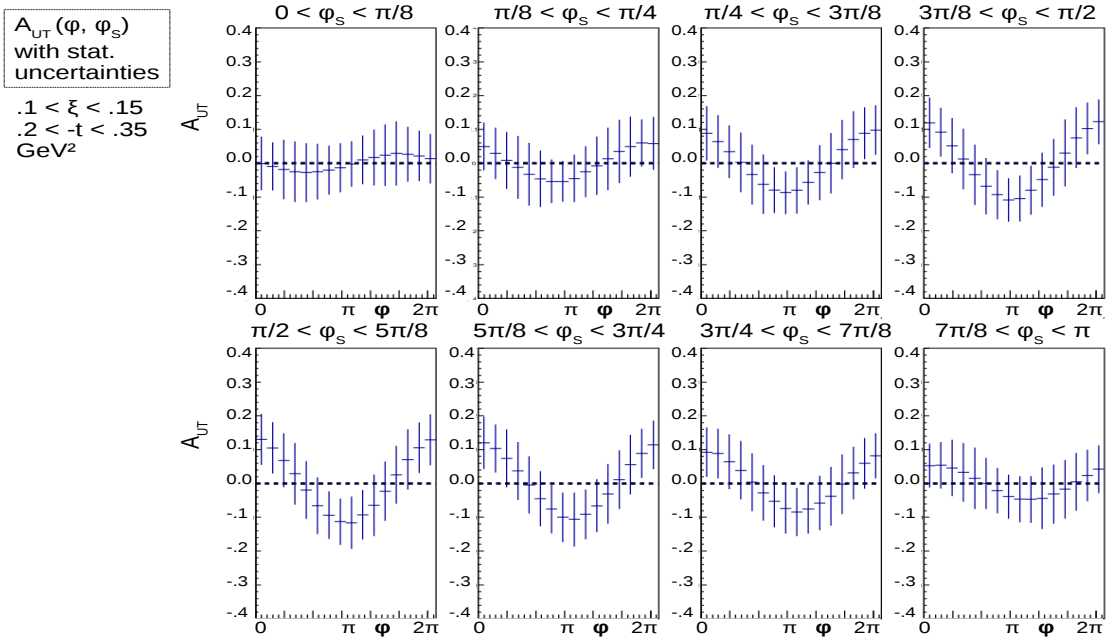


Figure 49: Projection of the single transversely polarized target spin asymmetries in bins of $\phi_S$ (panels), as a function of 16 bins in $\phi$ and for $0.1 < \xi < 0.15$ and $0.2 < -t < 0.35$ GeV$^2$. Statistic uncertainties are represented. Systematic uncertainties and the 27% target polarization dilution factor are not included.

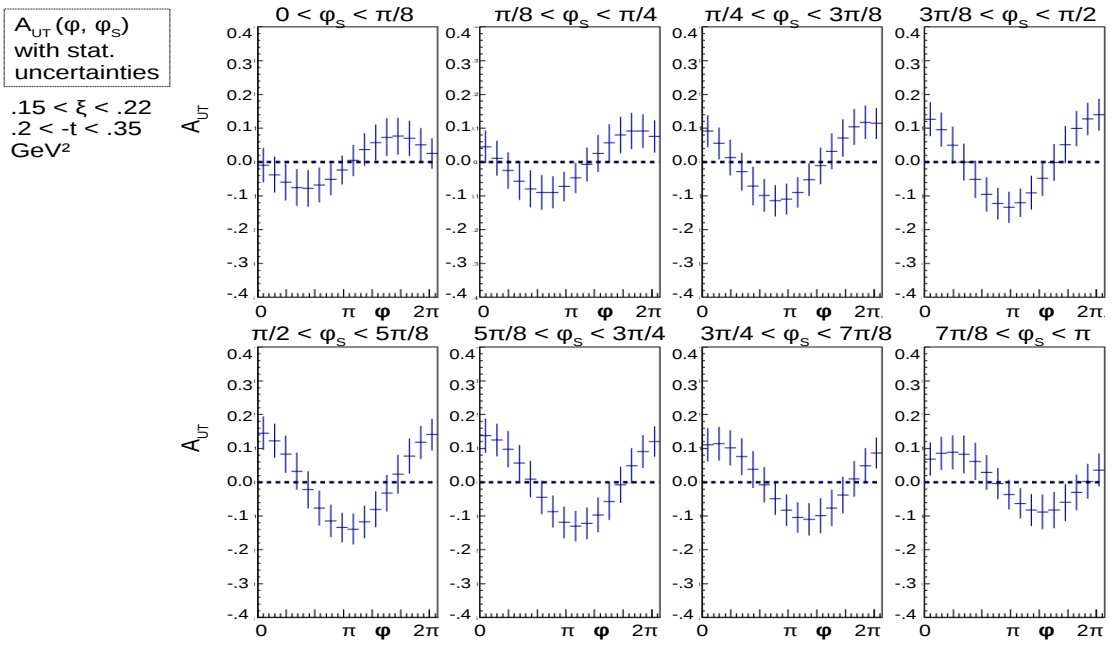


Figure 50: Projection of the single transversely polarized target spin asymmetries in bins of $\phi_S$ (panels), as a function of 16 bins in $\phi$ and for $0.15 < \xi < 0.22$ and $0.2 < -t < 0.35$ GeV$^2$. Statistic uncertainties are represented. Systematic uncertainties and the 27% target polarization dilution factor are not included.

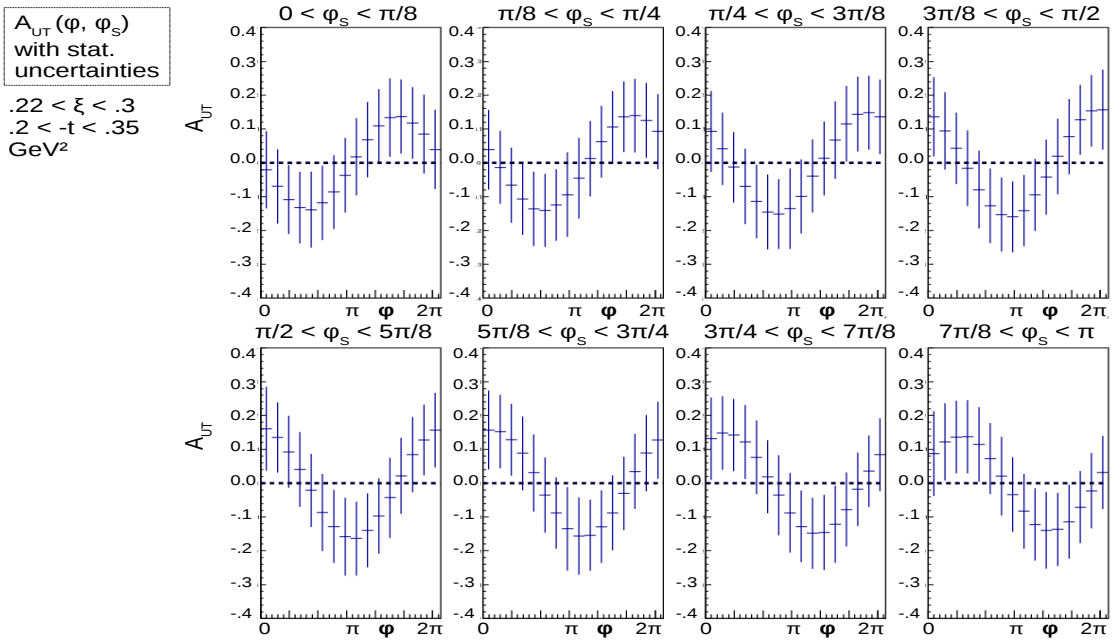


Figure 51: Projection of the single transversely polarized target spin asymmetries in bins of $\phi_S$ (panels), as a function of 16 bins in $\phi$ and for $0.22 < \xi < 0.3$ and $0.2 < -t < 0.35$ GeV$^2$. Statistic uncertainties are represented. Systematic uncertainties and the 27% target polarization dilution factor are not included.

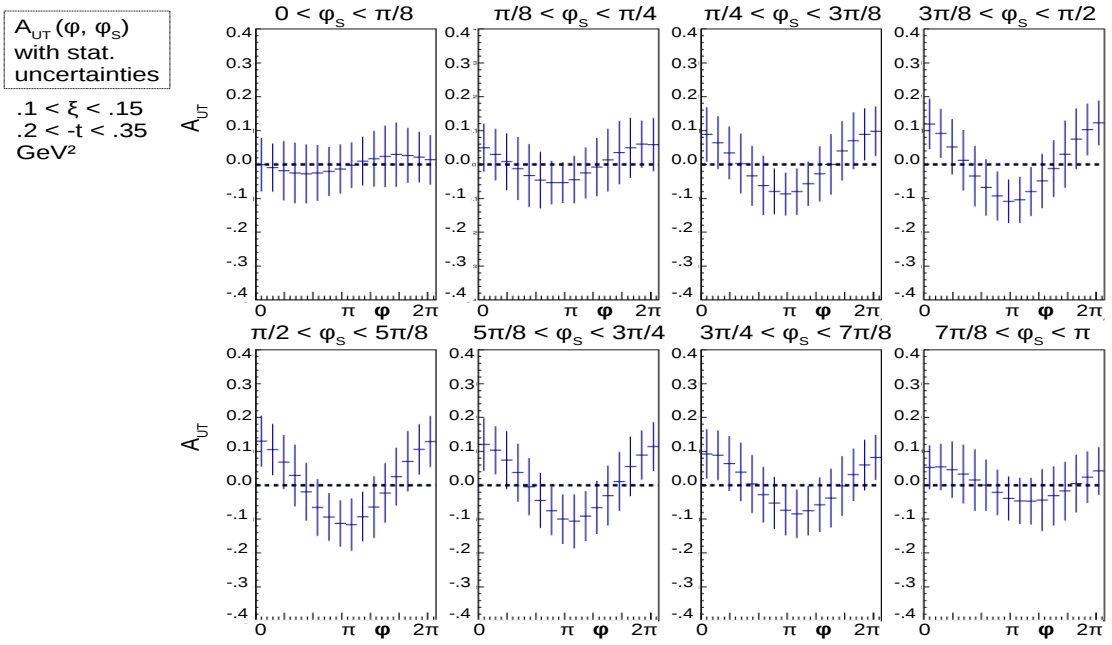


Figure 52: Projection of the single transversely polarized target spin asymmetries in bins of $\phi_S$ (panels), as a function of 16 bins in $\phi$ and for $0.1 < \xi < 0.15$ and $0.35 < -t < 0.7$ GeV$^2$. Statistic uncertainties are represented. Systematic uncertainties and the 27% target polarization dilution factor are not included.

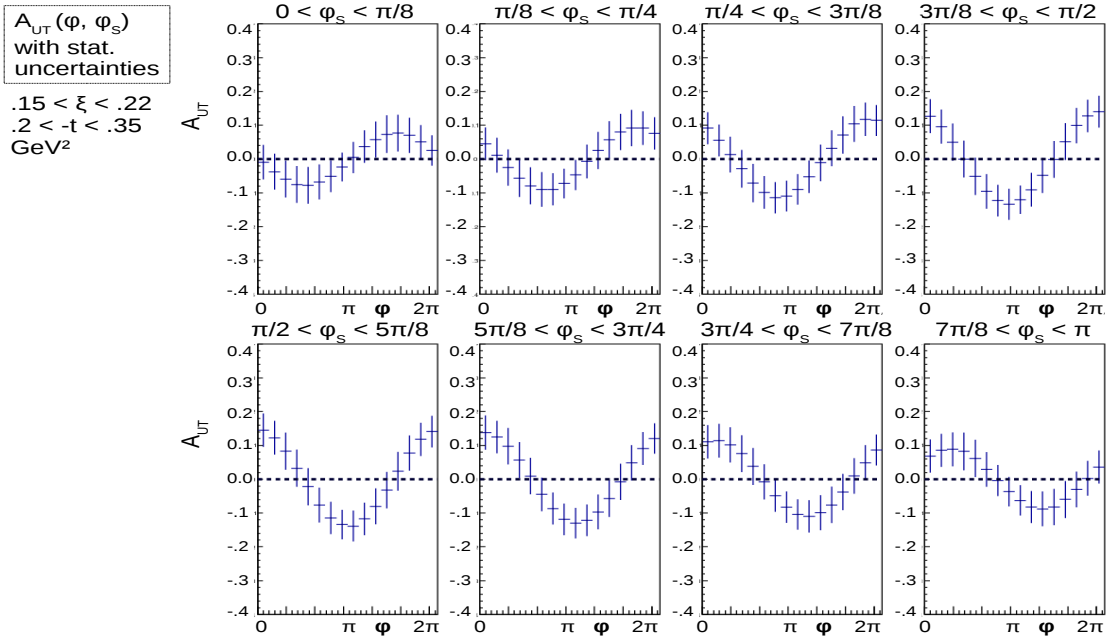


Figure 53: Projection of the single transversely polarized target spin asymmetries in bins of $\phi_S$ (panels), as a function of 16 bins in $\phi$ and for $0.15 < \xi < 0.22$ and $0.35 < -t < 0.7$ GeV$^2$. Statistic uncertainties are represented. Systematic uncertainties and the 27% target polarization dilution factor are not included.

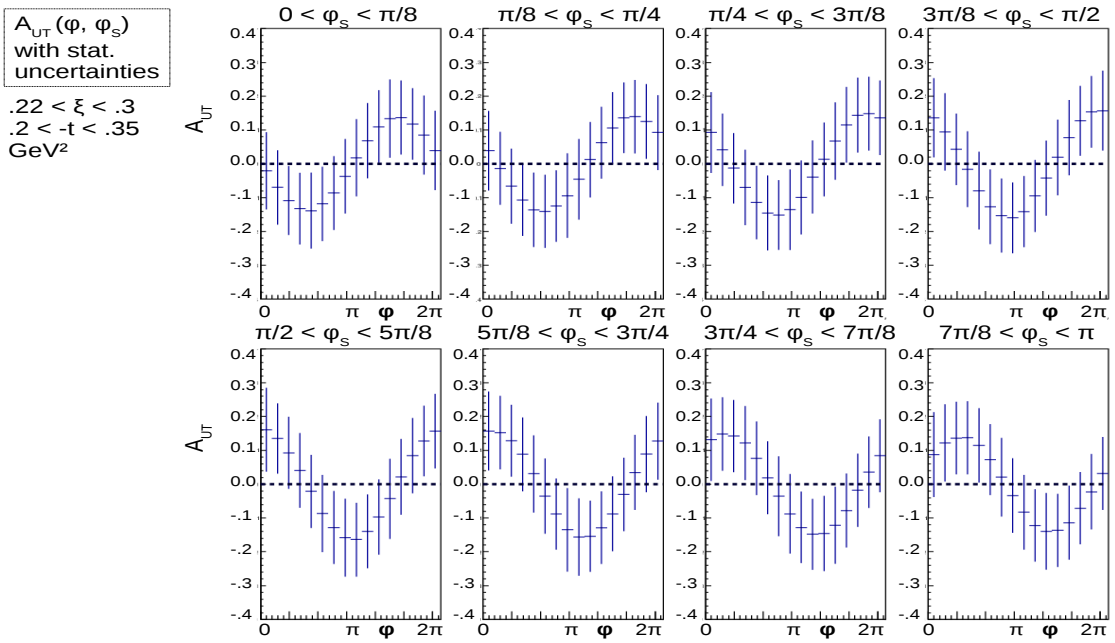


Figure 54: Projection of the single transversely polarized target spin asymmetries in bins of $\phi_S$ (panels), as a function of 16 bins in $\phi$ and for $0.22 < \xi < 0.3$ and $0.35 < -t < 0.7$ GeV$^2$. Statistic uncertainties are represented. Systematic uncertainties and the 27% target polarization dilution factor are not included.

## B.2 Figures of merit for the target spin asymmetry in kinematic bins

We dispay Figs. 55 to 62 the figures of merit of the transverse target spin asymmetry, as defined in section 4.7, for the 8 kinematic bins.

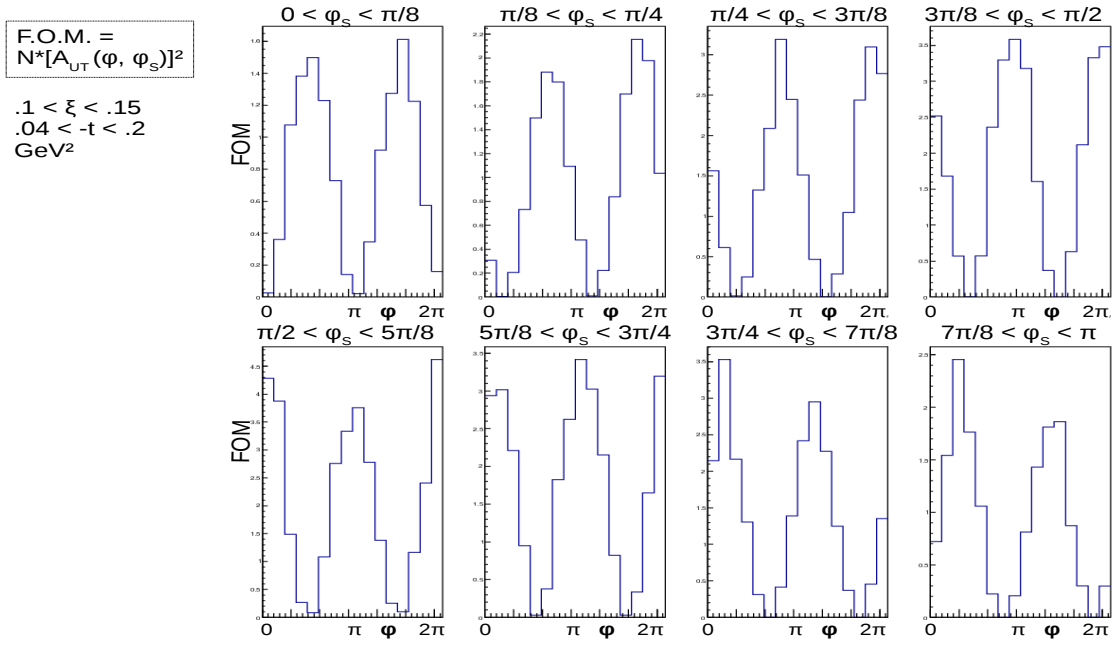


Figure 55: Figures of merit for the single transversely polarized target spin asymmetries in bins of $\phi_S$ (different panels), as a function of 16 bins in $\phi$ and for $0.1 < \xi < 0.15$ and $-t < 0.2$ GeV$^2$.

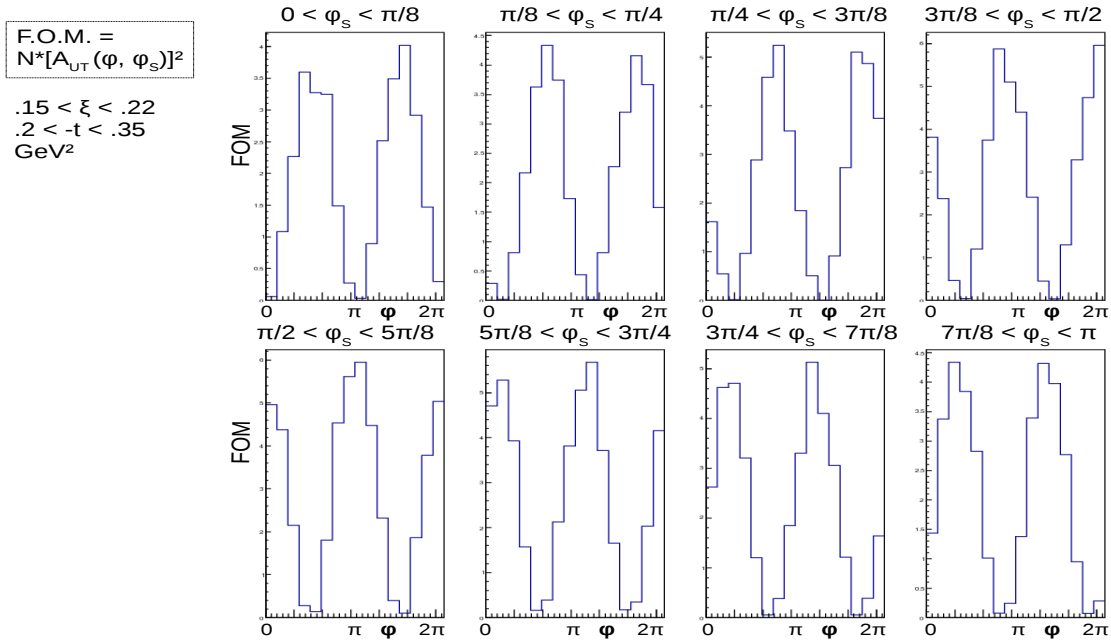


Figure 56: Figures of merit for the single transversely polarized target spin asymmetries in bins of $\phi_S$ (different panels), as a function of 16 bins in $\phi$ and for $0.15 < \xi < 0.22$ and $-t < 0.2$ GeV$^2$.

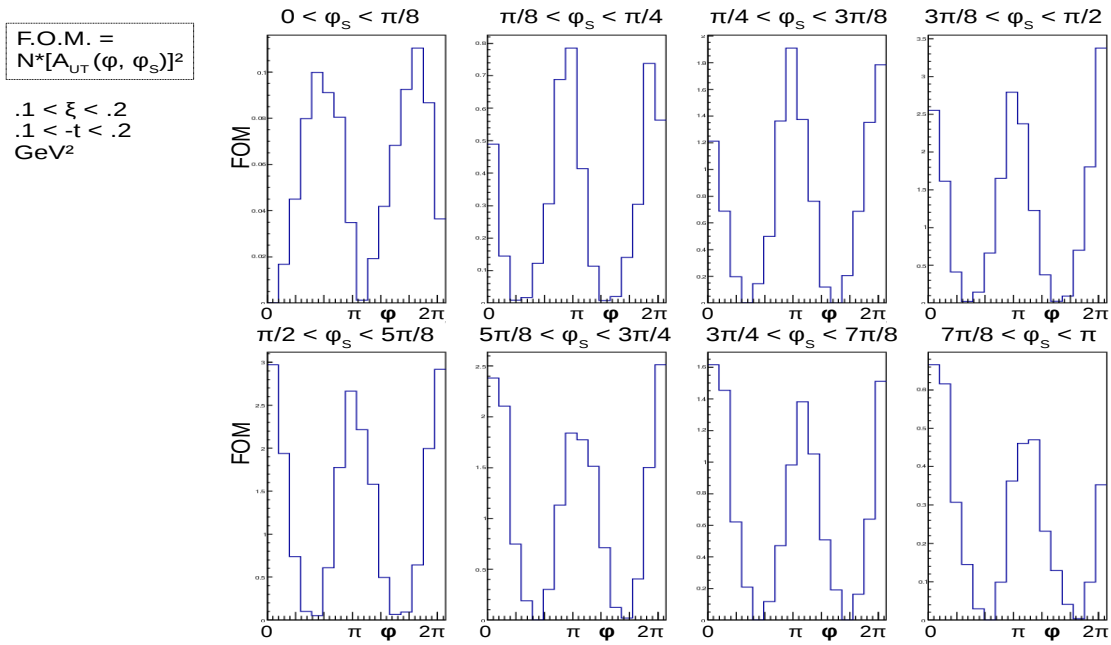


Figure 57: Figures of merit for the single transversely polarized target spin asymmetries in bins of $\phi_S$ (different panels), as a function of 16 bins in $\phi$ and for $0.1 < \xi < 0.15$ and $0.2 < -t < 0.35$ GeV$^2$.

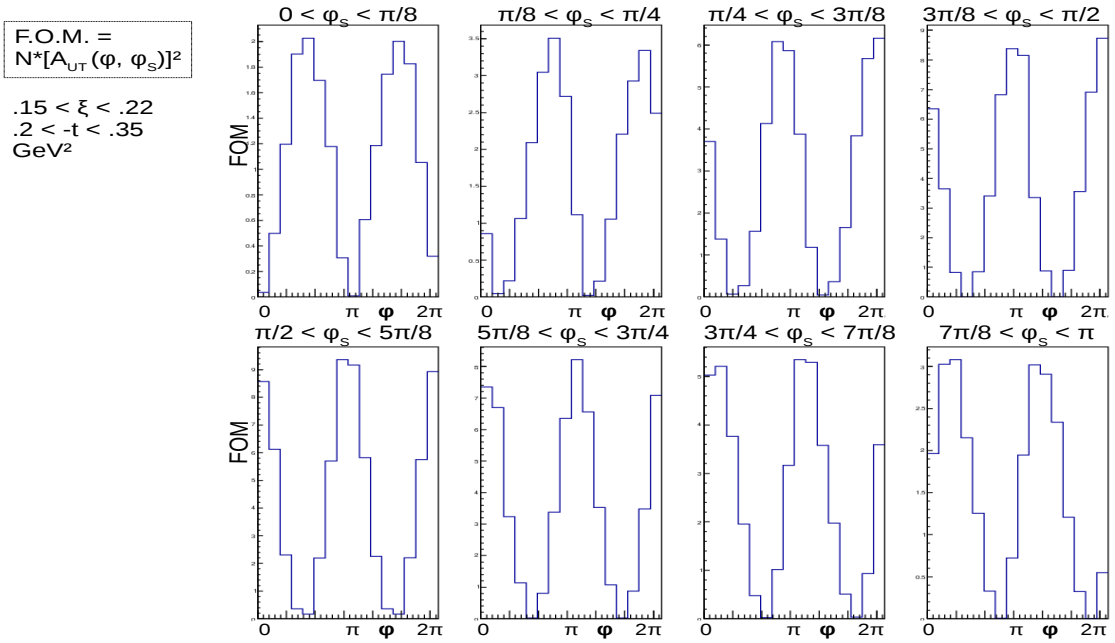


Figure 58: Figures of merit for the single transversely polarized target spin asymmetries in bins of $\phi_S$ (different panels), as a function of 16 bins in $\phi$ and for $0.15 < \xi < 0.22$ and $0.2 < -t < 0.35$ GeV$^2$.

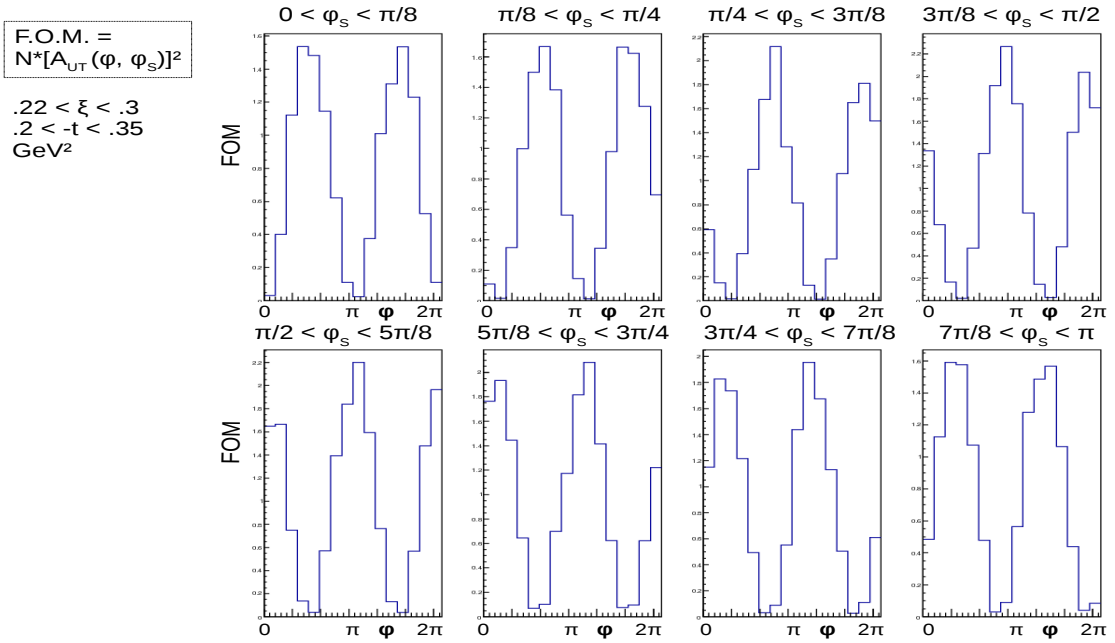


Figure 59: Figures of merit for the single transversely polarized target spin asymmetries in bins of $\phi_S$ (different panels), as a function of 16 bins in $\phi$ and for $0.22 < \xi < 0.3$ and $0.2 < -t < 0.35$ GeV$^2$.

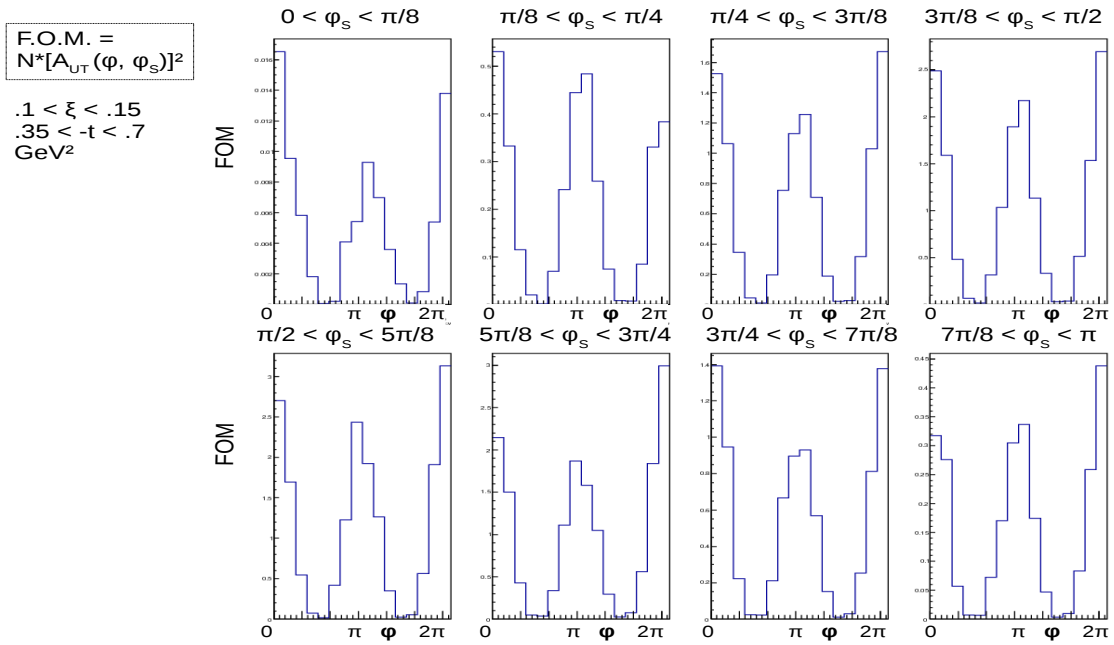


Figure 60: Figures of merit for the single transversely polarized target spin asymmetries in bins of $\phi_S$ (different panels), as a function of 16 bins in $\phi$ and for $0.1 < \xi < 0.15$ and $0.35 < -t < 0.7$ GeV$^2$.

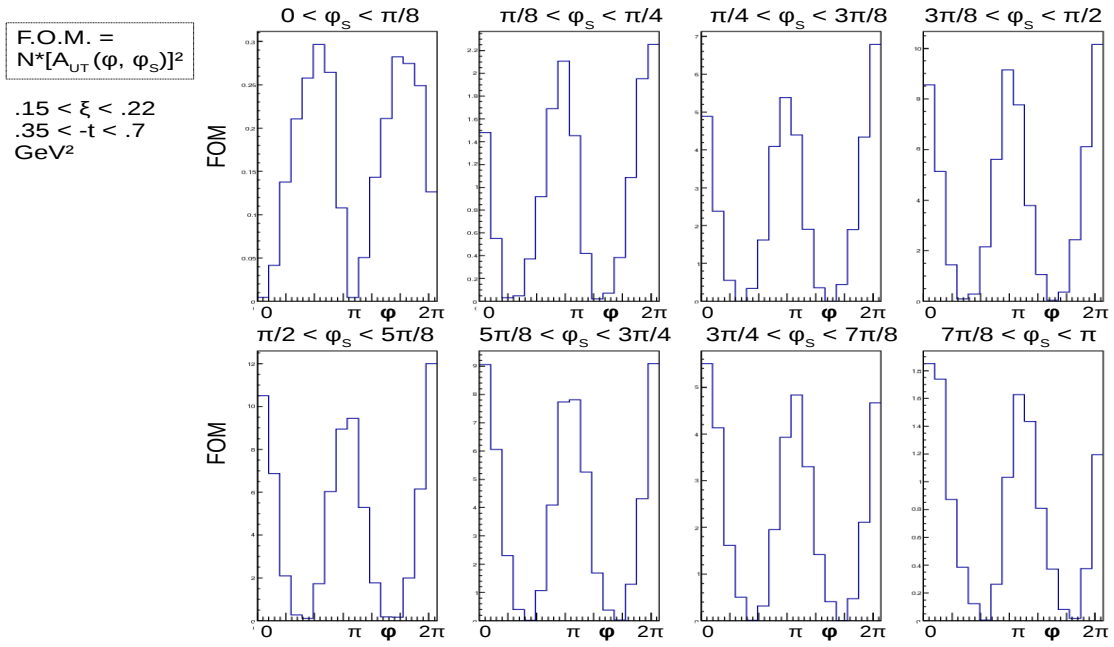


Figure 61: Figures of merit for the single transversely polarized target spin asymmetries in bins of $\phi_S$ (different panels), as a function of 16 bins in $\phi$ and for $0.15 < \xi < 0.22$ and $0.35 < -t < 0.7$ GeV$^2$.

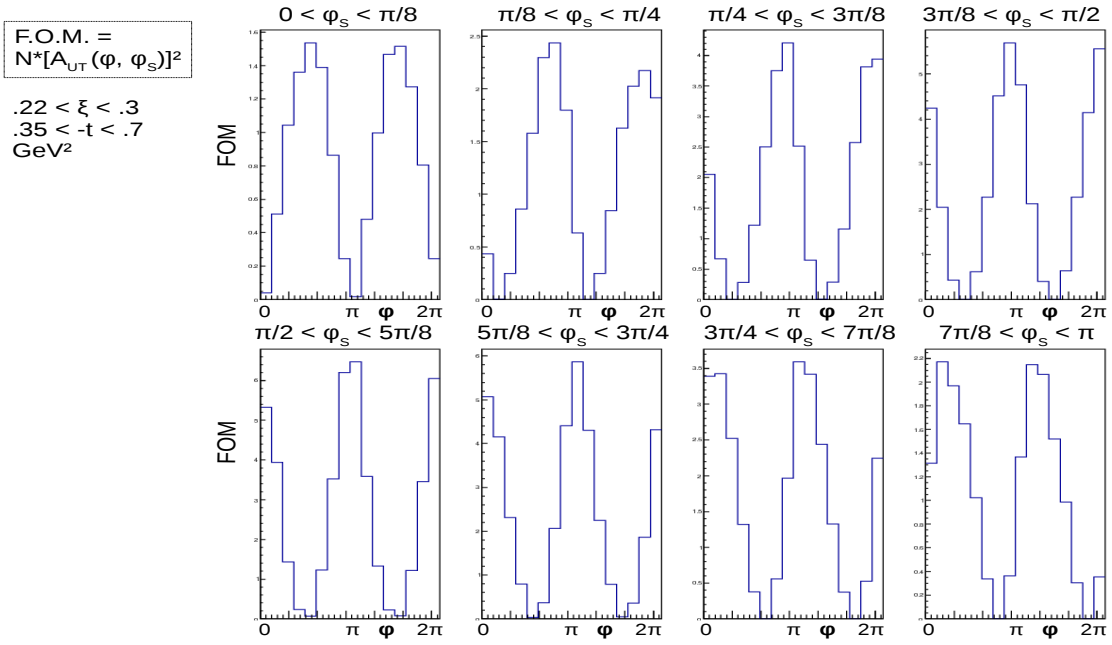


Figure 62: Figures of merit for the single transversely polarized target spin asymmetries in bins of $\phi_S$ (different panels), as a function of 16 bins in $\phi$ and for $0.22 < \xi < 0.3$ and $0.35 < -t < 0.7$ GeV$^2$.

## References


[1] Z. Zhao, M. Boër, P. Nadel-Turonski, J. Zhang, JLab experiment E12-12-006A: Timelike Compton Scattering on the proton in $e^+e^-$ with SoLID at 11 GeV, run group proposal to the PAC 43 (2015).

[2] P. Nadel-Turonski, M. Guidal, T. Horn, R. Paremuzyan, S. Stepanyan, JLab experiment E12-12-001: Timelike Compton Scattering and $J/\psi$ photoproduction on the proton in $e^+e^-$ pair production with CLAS12 at 11 GeV.

[3] D. Müller, D. Robaschik, B. Geyer, F.-M. Dittes and J. Hořejši, Fortsch. Phys. **42** (1994) 101

[4] X. D. Ji, Phys. Rev. D **55** (1997) 7114

[5] A. V. Radyushkin, Phys. Rev. D **56** (1997) 5524

[6] Goeke K, Polyakov M V and Vanderhaeghen M 2001 *Prog. Part. Nucl. Phys.* **47** 401

[7] M. Diehl, Phys. Rept. **388** (2003) 41

[8] M. Guidal, H. Moutarde and M. Vanderhaeghen, Rept. Prog. Phys. **76** (2013) 066202

[9] M. Boër, M. Guidal and M. Vanderhaeghen, Eur. Phys. J. A **51** (2015) no.8, 103.

[10] E. R. Berger, M. Diehl and B. Pire, Timelike Compton scattering: exclusive photoproduction of lepton pairs, The European Physical Journal C23 (2002) 675-689

[11] X. D. Ji, Phys. Rev. Lett. **78**, 610 (1997)

[12] Proceedings from High Intensity Photon Sources Workshop (CUA, 2/6–2/7 2017), https://arxiv.org/pdf/1704.00816.pdf

[13] D. Crabb and D. Day, *"The Virginia/Basel/SLAC polarized target: operation and performance during experiment E143 at SLAC"*. Nucl. Inst. Meth. **A**356, 9-19 (1995).

[14] H. Zhu, *"A Measurement of the Neutron Electric Form Factor in $\vec{D}(\vec{e}, e'n)p$ Quasi-elastic Scattering at $Q^2_= 0.5\ (GeV/c)^2$"*. Ph.D. Dissertation, University of Virginia, Charlottesville (2000).

[15] T. Horn et. al, Neutral Particle Spectrometer Facility in Hall C, proposal to PAC 40 (2013).

[16] Z-E. Meziani, K. Hafidi, X. Qian, N. Spaveris, JLab experiment E12-12-006, Near Threshold Electroproduction of J/$\Psi$ at 11 GeV, proposal to the PAC 39 (2012).

[17] L. Elouadrhiri, H. Avakian, V. Burkert, M. Guidal, M. Lowry, L. Pappalardo, and S. Procureur, JLab experiment E-12-12-010, conditionally approved.

[18] UVa target group web page: *http://twist.phys.virginia.edu/documents.html*.

[19] JLab target group web page: *https://poltar.jlab.org/drupal*.

[20] Vanderhaeghen M, Guichon P A M and Guidal M 1998 *Phys. Rev. Lett.* **80** 5064

[21] M. Vanderhaeghen, P. A. M. Guichon and M. Guidal, Phys. Rev. D **60** (1999) 094017 doi:10.1103/PhysRevD.60.094017

[22] Guidal M, Polyakov M V, Radyushkin A V and Vanderhaeghen M 2005 *Phys. Rev. D* **72** 054013

[23] A. V. Radyushkin, Phys. Rev. D **59** (1999) 014030

[24] A. V. Radyushkin, Phys. Lett. B **449** (1999) 81

[25] P. A. M. Guichon and M. Vanderhaeghen, Phys. Rev. Lett. **91** (2003) 142303

[26] E. J. Brash, A. Kozlov, S. Li and G. M. Huber, Phys. Rev. C **65** (2002) 051001

[27] A. V. Radyushkin, In *Shifman, M. (ed.): At the frontier of particle physics, vol. 2* 1037-1099

[28] S. Liuti, private communication.

[29] A.V. Belitsky, D. Mueller and A. Kirchner, Nucl. Phys. B629 (2002) 323.

[30] M. Defurne *et al.* [Jefferson Lab Hall A Collaboration], Phys. Rev. C **92** (2015) no.5

[31] H. Moutarde, B. Pire, F. Sabatie, L. Szymanowski and J. Wagner, Phys. Rev. D **87** (2013) no.5, 054029

[32] A. V. Belitsky and A. V. Radyushkin, Phys. Rept. **418** (2005) 1

[33] M. Aghasyan *et al.* [COMPASS Collaboration], Phys. Rev. Lett. **119** (2017) no.11, 112002

[34] D. W. Sivers, Phys. Rev. D **41** (1990) 83.

[35] M. Burkardt and D. S. Hwang, Phys. Rev. D **69** (2004) 074032 doi:10.1103/PhysRevD.69.074032

[36] Guidal M 2008 *Eur. Phys. J. A* **37**, 319 [Erratum-ibid. A **40**, 119 (2009)]

[37] C. Hyde-Wright, B. Michel, C. Munoz Camacho and J. Roche, JLab experiment E12- 06-114.

[38] F. Sabatié, A. Biselli, V. Burkert, L. Elouadrhiri, M. Garçon, M. Holtrop, D. Ireland, K. Joo, W. Kim, JLab experiment E12-06-119.

[39] C. Munoz Camacho, R. Paremuzyan, T. Horn, JLab experiment E12-13-010.

[40] S. Niccolai, V. Kubarovsky, S. Pisano, and D. Sokhan, JLab experiment E12-11-003.

[41] S. Niccolai et al, Deeply virtual Compton scattering on the neutron with a longitudinally polarized deuteron target, run group proposal E12-06-109A (2016).

[42] Polarization Observables in Wide-Angle Compton Scattering at large $s$, $t$, and $u$. G. Niculescu,B. Wojtsekhowski, D. Day, D. Keller, J. Zhang,D.J. Hamilton co-spokespersons. Proposal C12-17-008 conditionally approved by JLab PAC45 in 2017.

[43] The Charge Form Factor of the Neutron, JLab experiment E93-026, D. Day spokesperson.

[44] Precision Measurement of the Nucleon Spin Structure Functions in the Region of the Nucleon Resonances, JLab experiment E01-006, O. Rondon Aramayo spokesperson.

[45] Spin Asummetries on the Nucleon Experiment:SANE, JLab experiment E07-003, S. Choi, Z.E. Meziani, O. Rondon-Aramayo spokespersons.

[46] J. Pierce, J. Maxwell and C. Keith, Nucl. Instrum. Meth. A **738** (2014) 54.

[47] GeN Technical Note.

[48] D. Keller, "The UVa approved and proposed experiments," arXiv:1704.00816.

[49] M. Kubantsev et al., Performance of the Primex Electromagnetic Calorimeter, arXiv:physics/0609201, 22 Sep. 2006; A. Gasparyan, Performance of PWO crystal Detector for a High Resolution Hybrit Electromagnetic Calorimeter at Jefferson Lab., Proceed. X Int. Conf. Calorimetry in Particle Physics, Perugia, Italy, 29 March-2 April 2004, pp. 109-115.

[50] Measurement of Semi-Inclusive $\pi^0$ Production as Validation of Factorization, JLab Experiment E12-13-007, R. Ent, T. Horn, H. Mkrtchyan and V. Tadevosyan spokespersons. Proposal aproved in 2015 by JLab PAC40.

[51] M. Boër, DEEPGen: polarized BH+TCS event generator, `https://hallaweb.jlab.org/wiki/index.php/DDVCS_and_TCS_event_generator` (2015).

[52] Event generator for TCS from R. Paremuzyan.

[53] M. Boër, GlueX note 3571, *Angular correlations in deep exclusive photo-production of lepton pairs and tools for data analysis* (2018), `https://halldweb.jlab.org/doc-public/DocDB/ShowDocument?docid=3571`.

[54] L. Pentchev, private communication.

[55] M. Boër, PhD thesis (2014)

[56] M. Boër, E. Burtin, Measurement of the cross section for exclusive photoproduction of a single photon and of a neutral pion on hydrogen target, in the context of Generalized partons distributions studies at COMPASS II, COMPASS note 201312 (2013).

[57] M. Boër and M. Guidal, J. Phys. G **42** (2015) no.3, 034023